MODELING FUNCTIONAL INTERACTIONS BETWEEN

CORTICAL GYRI AND SULCI

by

XI JIANG

(Under the Direction of Tianming Liu)

ABSTRACT

Cortical gyrification, which is composed of convex and concave neural folding structures of gyri and sulci, is one of the most prominent features of human brain. A variety of recent studies in the brain mapping field have demonstrated the specific structural differences between gyral and sulcal regions. However, the potential functional differences and interactions between gyral and sulcal regions are largely unknown due to the complexity and variability of the structure and function of the cerebral cortex. In this dissertation, based on the proposed common structural and functional brain architecture which has anatomical, structural, and functional correspondences across different individuals, I develop four novel computational approaches to model the functional interactions between cortical gyri and sulci. Experimental results based on the four approaches demonstrate the meaningful functional interactions between cortical gyri and sulci, thus reveal novel functional architecture of cortical gyri and sulci, and provide novel understanding of functional mechanisms of human cerebral cortex.

INDEX WORDS: functional interaction, cortical gyri and sulci, functional magnetic resonance imaging, brain structure and function

MODELING FUNCTIONAL INTERACTIONS BETWEEN CORTICAL GYRI AND SULCI

by

XI JIANG

B.E., Northwestern Polytechnical University, China, 2009

A Dissertation Submitted to the Graduate Faculty of The University of Georgia in Partial Fulfillment of the Requirements for the Degree

DOCTOR OF PHILOSOPHY

ATHENS, GEORGIA

2016

MODELING FUNCTIONAL INTERACTIONS BETWEEN CORTICAL GYRI AND SULCI

by

XI JIANG

Major Professor: Tianming Liu

Committee: Suchendra M. Bhandarkar

L. Stephen Miller

Xiaoping Hu

Electronic Version Approved:

Suzanne Barbour

Dean of the Graduate School

The University of Georgia

August 2016

DEDICATION

This work is dedicated to my loving parents for their longstanding support. This work is also dedicated to all the researchers in the fields of brain imaging, cognitive neuroscience, psychology, psychiatry and brain mapping who need to systematically study the functional brain connectivity/interaction.

ACKNOWLEDGEMENTS

First and foremost, I would like to express my sincere gratitude to my major professor, Dr. Tianming Liu. He is not only my advisor in academia, but also my good friend in life. I will never forget the countless efforts Dr. Liu has devoted to training me from a fresh PhD student to an independent researcher in the brain mapping field during the past six years. I will engrave his attitude in both research and life: be optimistic, patient, and serious. Second, I would like to thank my PhD committee members, Dr. Suchendra M. Bhandarkar, Dr. L. Stephen Miller, and Dr. Xiaoping Hu. They have given me numerous insightful suggestions from computer science, psychology, and brain imaging perspectives. Their thorough guidance has prepared me the experience for communicating with people from various backgrounds and conducting interdisciplinary studies in the brain mapping field. Third, I would like to thank my colleagues in the CAID lab and my friends in UGA (too many to mention). I cannot make this achievement without their help in both research and life. Finally, I want to say thank you to my parents and relatives. They are always my strongest supporters whenever I encounter difficulties studying abroad.

Twenty years ago when I was ten years old, I was sitting in front of the TV and watching Atlanta Summer Olympic Games. Today, twenty years later, I am sitting in the lab office which is next to the Atlanta Olympic Games coliseum and writing the dissertation as my 30th birthday gift. Confucius once said: ‘At thirty, I stood firm.’ Hope I can always stand firm at work and in life.

TABLE OF CONTENTS

Page

LIST OF TABLES

Page

LIST OF FIGURES

Page

CHAPTER 1

INTRODUCTION

1.1 Dissertation Statement

One of the most prominent features of human cerebral cortex is the highly convoluted cortical folding, which is composed of convex and concave neural folding structures of gyri and sulci (Barron 1950; Rakic 1988; Welker 1990). Recent studies in the brain mapping field have demonstrated that there are specific structural differences between gyri and sulci from both macro- and micro- scale perspectives (Nie et al., 2012; Takahashi et al., 2012; Chen et al., 2013; Zhang et al., 2014; Zeng et al., 2015). From macro-scale perspective, our recent study (Nie et al., 2012) reported that the termination of streamline fibers concentrate on gyral regions in human, chimpanzee, and macaque brains based on diffusion tensor imaging (DTI) and high angular resolution diffusion imaging (HARDI) data. Another study (Takahashi et al., 2012) on human fetus brain also observed similar phenomenon. Chen et al., 2013 reported a similar finding that structural fiber connection pattern closely follows the gyral folding pattern in the tangent direction to the cortical sphere. Zhang et al., 2014 characterized and focused on the U-shapes of streamline fibers based on DTI, HARDI, and diffusion spectrum imaging (DSI) data respectively, and demonstrated that a majority of the U-shaped streamline fibers connect neighboring cortical gyri and course along sulci in human, chimpanzee, and macaque brains. From micro-scale perspective, a recent study (Zeng et al., 2015) based on the recently released Allen Mouse Brain Atlas demonstrated that the cerebellum gyri and

sulci of rodent brains are significantly different in both axonal connectivity and gene expression patterns. Although interesting results have been demonstrated for the structural differences between gyri and sulci, the potential functional differences and interactions between gyral and sulcal regions are largely unknown in the current literatures due to the complexity and variability of the structure and function of the cerebral cortex. Dissecting the functional differences as well as interactions between cortical gyri and sulci can provide foundations for studying functional mechanisms of human brain, help unveil the intrinsic relationships among cortical folding patterns, structural connections, and functional interactions between gyri and sulci, and fundamentally advance scientific understanding of the human brain.

In order to address this problem, in this dissertation, based on our previously proposed common structural and functional brain architecture which has anatomical, structural, and functional correspondences across different individuals/populations, I develop four novel computational approaches to model the functional interactions between cortical gyri and sulci based on modern in-vivo multi-modal neuroimaging data including Magnetic Resonance Imaging (MRI), DTI, and functional MRI (fMRI). We aim to unveil the functional differences and interactions between cortical gyri and sulci from the four different perspectives.

1.2 Contributions

Common structural human brain architecture: We develop a novel anatomy-guided cortical landmark discovery framework (Chapter 2) to identify large-scale cortical landmarks, called ‘Anatomy-guided Dense Individualized and Common Connectivity-

based Cortical Landmarks (A-DICCCOL)', which are common across different subjects/populations but still retain the individual variability based on DTI data (Jiang et al., 2013; Jiang et al., 2015). These A-DICCCOL landmarks have been demonstrated to have intrinsic correspondences across individuals/populations with anatomical, DTI-derived fiber connection pattern, and functional consistency (Jiang et al., 2013; Jiang et al., 2015). Notably, the developed set of cortical landmarks as well as the DICCCOL landmarks (Zhu et al., 2013) have a variety of applications in our recent studies which are not detailed in this dissertation: functional annotation of DICCCOLs (Yuan et al., 2013), identification of large-scale functional connectivity alterations between normal controls and specific disease groups such as Mild Cognitive Impairment (MCI), Attention Deficit Hyperactivity Disorder (ADHD), and Post-Traumatic Stress Disorder (PTSD) (Jiang et al., 2013; Jiang et al., 2014; Wang et al., 2013; Li et al., 2014), modeling functional interactions among functional networks (Jiang et al., 2014; Li et al., 2014), and representing low-level multimedia features using high-level DICCCOL-based semantic features (Jiang et al., 2012; Fang et al., 2015). This set of A-DICCCOL landmarks also provides the structural foundation for modeling functional interactions between cortical gyri and sulci in this dissertation.

Common functional human brain architecture: We develop a novel machine learning and sparse representation framework (Chapter 3), called 'Holistic Atlases of Functional Networks and Interactions (HAFNI)', to identify large-scale functional brain networks and their spatial overlaps which are common across subjects/populations but still retain the individual variability based on fMRI data (Lv et al., 2015a; Lv et al., 2015b). The identified large-scale functional networks are reproducible and robust across

different individuals/populations, and are simultaneously distributed in distant neuroanatomic areas while substantially spatially overlapping with each other (Lv et al., 2015a; Lv et al., 2015b). Notably, the developed HAFNI framework also has a variety of applications in our recent studies which are not detailed in this dissertation: identification of potential large-scale functional network alterations in specific diseases such as MCI, Alzheimer's Disease (AD), and Prenatal Alcohol Exposure (PAE) (Jiang et al., 2014; Lv et al., 2015c), and representing low-level multimedia features using high-level HAFNI-based semantic brain features (Zhao et al., 2014). This HAFNI framework also provides the functional foundation for modeling functional interactions between cortical gyri and sulci in this dissertation.

Modeling functional interactions between cortical gyri and sulci: We develop four novel approaches to model the functional interactions between cortical gyri and sulci from different perspectives. First, we assess the resting state functional connectivity difference between cortical gyral and sulci regions, and propose a novel functional connectivity model of cortical gyri and sulci (Chapter 4). Second, we systematically characterize and identify the task-based heterogeneous functional regions (THFRs) on cortical surface, and assess their distribution difference between cortical gyral and sulcal regions (Chapter 5). Third, we assess the temporal dynamics difference of spatial overlap pattern of functional brain networks between cortical gyral and sulcal regions (Chapter 6). Finally, we examine the resting state fMRI signal sparse representation accuracy difference between cortical gyral and sulcal regions, and propose a novel gyri/sulci-guided working model of functional networks (Chapter 7). These four approaches

demonstrate the meaningful functional interactions between cortical gyri and sulci from different perspectives.

1.3 Dissertation Outline

As illustrated in Fig. 1.1, this dissertation mainly contains six parts corresponding to Chapters 2-7, respectively. Chapters 2 and 3 will demonstrate the establishment of A-DICCCOL and HAFNI system, respectively. They are the foundations for modeling functional interactions between cortical gyri and sulci. Chapters 4-7 will introduce the proposed four approaches to model functional interactions between cortical gyri and sulci, respectively. Chapter 8 is the discussion and conclusion.

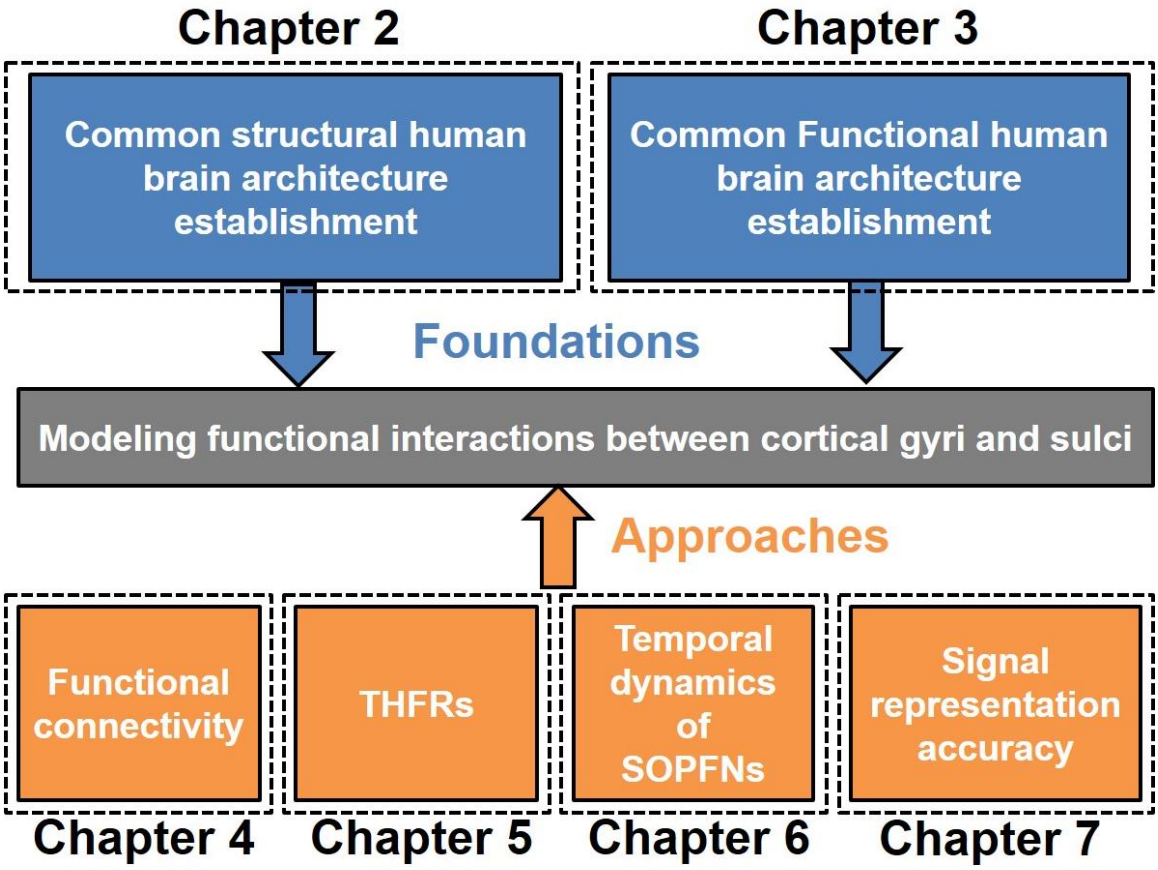

Figure 1.1. Overview of this dissertation.

CHAPTER 2

ANATOMY-GUIDED DENSE INDIVIDUALIZED AND COMMON CONNECTIVITY-BASED CORTICAL LANDMARKS (A-DICCCOL)[1]

[1]Xi Jiang, Tuo Zhang, Dajiang Zhu, Kaiming Li, Hanbo Chen, Jinglei Lv, Xintao Hu, Junwei Han, Dinggang Shen, Lei Guo, and Tianming Liu. 2015. *IEEE Transactions on Biomedical Engineering*. 62(4):1108-19.

Abstract

Establishment of structural and functional correspondences of human brain that can be quantitatively encoded and reproduced across different subjects and populations is one of the key issues in brain mapping. As an attempt to address this challenge, our recently developed DICCCOL (Dense Individualized and Common Connectivity-based Cortical Landmarks) system reported 358 connectional landmarks, each of which possesses consistent DTI-derived white matter fiber connection pattern that is reproducible in over 240 healthy brains. However, the DICCCOL system can be substantially improved by integrating anatomical and morphological information during landmark initialization and optimization procedures. In this chapter, we present a novel anatomy-guided landmark discovery framework that defines and optimizes landmarks via integrating rich anatomical, morphological, and fiber connectional information for landmark initialization, group-wise optimization and prediction, which are formulated and solved as an energy minimization problem. The framework finally determines 555 consistent connectional landmarks. Validation studies demonstrate that the 555 landmarks are reproducible, predictable and exhibited reasonably accurate anatomical, connectional and functional correspondences across individuals and populations, and thus are named anatomy-guided DICCCOL or A-DICCCOL. This A-DICCCOL system represents common cortical architectures with anatomical, connectional and functional correspondences across different subjects, and would potentially provide opportunities for various applications in brain science.

Introduction

Establishment of structural and functional correspondences of human brain across different subjects and populations is one of the important issues in the brain mapping field. For several decades, three major categories of approaches have been largely adopted in the brain mapping field to establish the correspondences of brain regions across individuals, and remarkable successes have been achieved by those approaches. The first category is brain image registration algorithms (e.g., Thompson and Toga, 1996; Fischl et al., 2002; Shen and Davatzikos, 2002; Van Essen and Dierker, 2007; Avants et al., 2008; Jia et al., 2010; Yap et al., 2011; Zhang and Cootes, 2011; Asman and Landman, 2011). In general, brain image registration methods are mainly concerned with morphological correspondences across individuals. The second category is cortical parcellations (e.g., Rettmann et al., 2002; Behrens et al., 2004; Jbabdi et al., 2009; Li et al., 2009). These cortical parcellation approaches typically designed certain criteria to define cortical region boundaries with the aim of establishing correspondences during parcellation of multiple brains. The third category is manual/semi-automatic regions of interests (ROI) analysis (e.g., Liu, 2011; Poldrack, 2012; Li et al., 2012). The ROI-based correspondence establishment methods are usually suitable for specific application scenarios.

Alternatively, several recent studies attempted to define and discover consistent and common brain cortical landmarks with intrinsic structural and functional correspondences across different subjects and populations (Li et al., 2012; Zhang et al., 2012; Zhu et al., 2011; Li et al., 2012; Li et al. 2012; Zhu et al., 2013). In particular, several multimodal DTI/fMRI studies (Zhu et al., 2013; Saygin et al., 2011; Honey et al.,

2009; Li et al., 2010) have demonstrated the close relationships between DTI-derived fiber connection patterns and brain functions. This provides direct supporting evidence to the connectional fingerprint concept (Passingham et al., 2002), which premises that each brain's cytoarchitectonic area has a unique set of extrinsic inputs and outputs that largely determines the functions that each brain area performs. Based on these principles, we developed and validated a data-driven connectional landmark discovery approach dubbed as: Dense Individualized and Common Connectivity-based Cortical Landmarks (DICCCOL) in (Zhu et al., 2013), which identified 358 consistent connectional landmarks. The basic idea was to optimize the localizations of each initial DICCCOL landmark in individual brains by maximizing the group-wise consistency of their DTI-derived white matter fiber connectivity patterns (Zhu et al., 2013). Our validation studies have demonstrated that the DICCCOLs provide reasonably good intrinsically-established correspondences across subjects and populations, and these 358 DICCCOLs have been released online at: http://dicccol.cs.uga.edu.

However, the DICCCOL system reported in (Zhu et al., 2013) merely considers the DTI-derived fiber connectivity pattern consistency across different subjects as the metric during landmark identification, and can be substantially improved by integrating additional meaningful anatomical, morphological and fiber connectional information during the landmark identification. Moreover, the landmark initialization for the DICCCOL was merely based on randomly sampled grid points in a template brain. Each grid of initialized landmarks in the template brain was then registered to other brains via linear registration and the landmark optimization was performed afterwards (Zhu et al., 2013). However, anatomical inter-individual variability sometimes misleads the process

of normalization. For example, in some brains the central fissure stops higher than the usual and misleads the registration of the pre and post central gyri. As a consequence, the same corresponding landmark might be misplaced in certain brains. This scenario is illustrated in Fig. 2.1 as an example. Here, we initialized a corresponding landmark located on the left pre-central gyrus (shown as yellow bubble) in three example brains from the template brain via linear registration. It is apparent that the landmark initializations for the first two brains were reasonably accurate (roughly located on the left pre-central gyrus), but the initialization for the third brain was wrong (located on the left post-central gyrus). Therefore, the following landmark optimization procedure would have difficulty in finding consistent fiber connection patterns for these inconsistently initialized landmarks due to image registration error caused by anatomical inter-individual variability and would potentially miss this possibly consistent landmark.

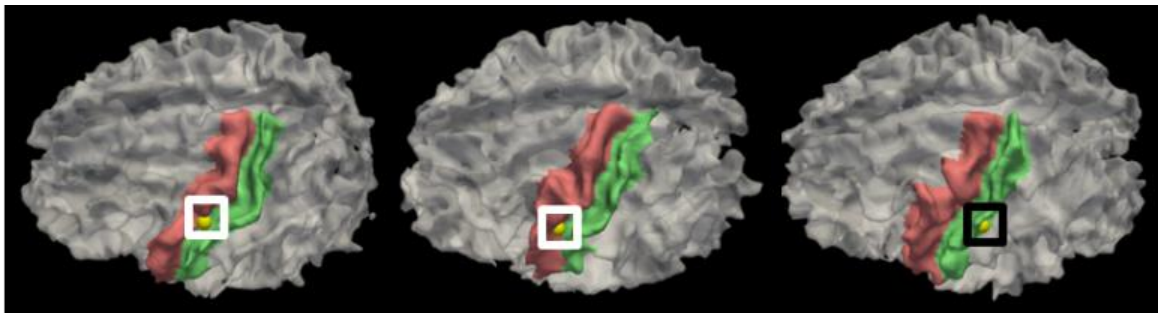

Figure 2.1. An illustration of landmark initialization inaccuracy due to anatomical inter-individual variability. The landmark is highlighted by yellow bubble. The landmarks highlighted by the white boxes in first two brains are located in the left pre-central gyrus (highlighted by red), while the landmark highlighted by the black box in third brain is located in the left post-central gyrus (highlighted by green).

In this chapter, we substantially improved the identification framework of our original DICCCOL system in (Zhu et al., 2013) and introduced the anatomy-guided DICCCOL or A-DICCCOL. Our major improvements are: first, instead of randomly sampled grid points in a template brain as the initialized landmarks in original DICCCOL system, we initialized the connectional landmarks on corresponding gyri/sulci under anatomical guidance for each brain to improve the accuracy of landmark initialization and thus facilitate the landmark optimization and discovery procedure. Second, instead of merely considering the DTI-derived fiber connection pattern similarity as the metric in previous DICCCOL system, we added meaningful anatomical, structural connection pattern homogeneity and spatial information during the group-wise landmark optimization procedure. Specifically, in this chapter, three new constraints including anatomical, structural connection pattern homogeneity, and spatial constraints, as well as the previous adopted structural connection pattern similarity constraint, were jointly modeled and integrated together to optimize the landmark locations within individual brains. Extensive experiments have demonstrated the effectiveness and meaningfulness of those newly added constraints in seeking group-wise consistent and corresponding connectional landmarks in individual brains. Third, we applied the proposed connectional landmark discovery procedures on HARDI data and recently publicly released Human Connectome Project (HCP) high-quality DTI data (Q1 release) (Uğurbil et al., 2013), and via different fiber tracking software tools to examine the consistency of the DTI-derived connectional landmarks, which is another validation improvement than previous DICCCOL system. Our proposed framework finally identified 555 new and consistent connectional landmarks, called the anatomy-guided DICCCOL or A-DICCCOL here.

Extensive validations based on DTI, HARDI and fMRI datasets have demonstrated that the 555 landmarks are reproducible, predictable and exhibit reasonably accurate anatomical, connectional and functional correspondences across individuals and populations.

Data Acquisition and Preprocessing

We used five different multimodal DTI/HARDI/fMRI datasets for initialization, optimization, determination, prediction and validation of A-DICCCOL landmarks, as summarized in Table 2.1. In particular, we randomly selected ten subjects with DTI data from Dataset #1 as the model brains (Fig. 2.2) for landmark initialization and the following group-wise optimization and identification. The remaining subjects from Datasets #1-#5 were used as the testing brains (Fig. 2.2). The details of the five datasets and pre-processing steps are referred to (Jiang et al., 2015).

Table 2.1. Summary of five different datasets.

Datasets	**No. of Subjects**	**Types**	**Functional Activation Maps**	**Model/Testing Brains**
# 1	23	DTI, one task-based fMRI scan	Working memory	10 out of 23: Model; the others: Testing
# 2	13	DTI, five task-based fMRI scans	Emotion, empathy, fear, semantic decision making, working memory	Testing
# 3	20	DTI	None	Testing
# 4 (HCP)	68	DTI	None	Testing
# 5	5	HARDI	None	Testing

A-DICCCOL Identification

Fig. 2.2 summarizes the flowchart of the computational framework for the A-DICCCOL identification. In total, there are four major steps as shown by the numbers: landmark initialization, landmark optimization, landmark determination, and landmark prediction. Details will be covered in the subsequent sections.

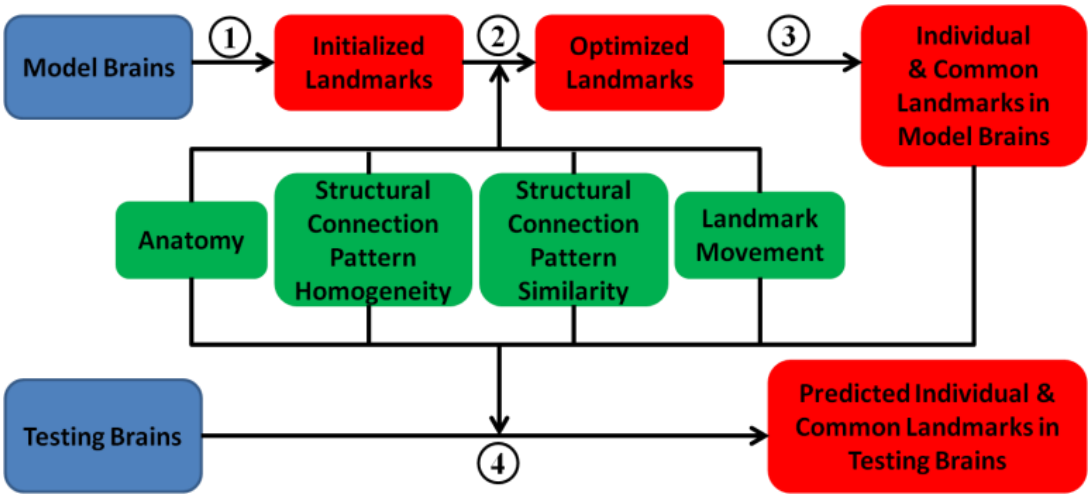

Figure 2.2. The flowchart of the computational framework for the A-DICCCOL landmark identification. Step 1: landmark initialization; Step 2: landmark optimization (four constraints are highlighted by the green boxes, respectively); Step 3: landmark determination; Step 4: landmark prediction.

Landmark Initialization-As mentioned in the introduction and detailed in (Zhu et al., 2013), the landmark initialization for our previous DICCCOL system was only based on randomly sampled grid points (2056) in a template brain. Then, each grid of initialized landmarks in the template brain was registered to other subjects using the linear registration algorithm FSL FLIRT (Jenkinson and Smith, 2001) and landmark optimization was performed afterwards. However, the accuracy of landmark initialization

across different subjects might be affected due to the anatomical inter-individual variability, and thus the landmark optimization procedure might be hampered. In this A-DICCCOL discovery framework, we refined the landmark initialization procedure by initializing corresponding landmark on the same gyrus/sulcus under anatomical guidance across different subjects to improve the accuracy of landmark initialization and thus to facilitate the landmark optimization and discovery procedure.

Specifically, first, ten subjects were randomly selected from Dataset #1 as the group of model brains (Fig. 2.2) for landmark initialization and the following group-wise optimization and determination. It is noted that we randomly selected one of the ten model brains as the template and other model brains were linearly registered to it so that their global shape differences were removed and their cortical surfaces were in the same space for comparison and landmark initialization. Second, for each model brain, the roughly anatomically-corresponding landmarks on the cortical surfaces were interactively labeled by two experts and further checked by the third expert according to the brain template used in the BrainVoyager Brain Tutor (http://www.brainvoyager.com). Specifically, for each clearly identifiable major gyrus/sulcus, a certain number (ranging from 3-20) of landmarks were selected at cortical surface mesh vertices that are roughly distributed evenly along the gyral ridge/sulcal valley (Deng et al., 2014), and are sufficiently dense to ensure the full coverage of the whole gyral ridge/sulcal valley. In total, we interactively labeled 594 corresponding landmarks that fully cover the whole major gyral ridge/sulcal valley for each of the ten model brains. It should be noted that the number of initialized landmarks that fully cover the whole major gyral ridge/sulcal valley (here 594) does not affect the following group-wise landmark optimization result,

since redundant landmarks are automatically merged during the optimization procedure later. It should also be noted that our aim was not to accurately locate the anatomical correspondence of each landmark due to the highly variability of cortical folding patterns even within the same gyrus/sulcus across different subjects. We just enforced the roughly macro-anatomical (gyri/sulci scale) correspondence for the landmarks to improve the accuracy of landmark initialization compared to previous DICCCOL system and further to preserve the same anatomical identity of roughly corresponding landmarks during landmark optimization. Fig. 2.3 shows the initialized 594 corresponding landmarks. These landmarks with rough anatomical correspondences served as the initial locations for group-wise optimization in the next step.

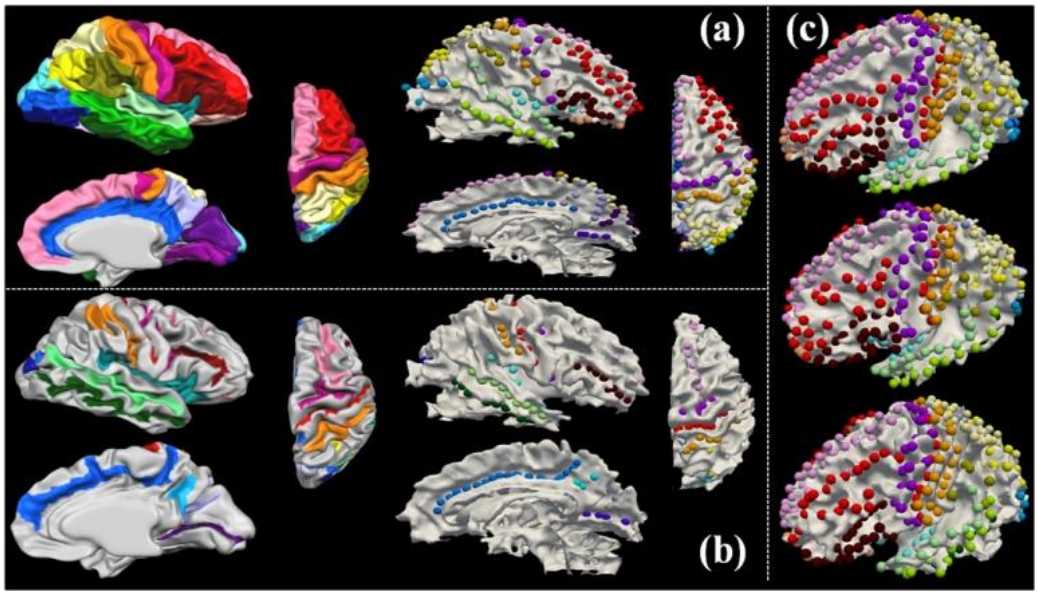

Figure 2.3. Visualization of initialized A-DICCCOL landmarks on the model brains. (a): the brain template with labelled major gyri, and the corresponding initialized landmarks of one example model brain. (b): the brain template with labeled sulci, and the corresponding initialized landmarks of the same model brain in (a). The initialized

landmarks on corresponding gyri/sulci in (a)-(b) are highlighted in the same color with the brain template. (c): all 594 initialized landmarks in three example model brains.

Structural Connection Pattern Homogeneity-Our prior studies (Liu, 2011; Zhu et al., 2011; Li et al., 2010) have demonstrated that the structural connection profile of an ROI could be highly nonlinear, that is, a slight change to the location, size or shape of the ROI could significantly alter its DTI-derived fiber connection patterns. Therefore, this high nonlinearity could cause uncertainties and instabilities in the discovery of consistent and reproducible connectional landmarks. In this chapter, we systematically examined the DTI-derived fiber structural connection pattern linearity/homogeneity of the cortical surface in detail. Specifically, first, for each cortical mesh vertex, we extracted the DTI-derived white matter fiber bundles emanating from it to represent its structural connection pattern. Second, we used our recently developed trace-map model (Zhu et al., 2011a; Zhu et al., 2011b) to quantitatively represent the fiber bundles. To be self-contained, the trace-map model projects a fiber bundle into a point distribution pattern on the standard surface of a unit sphere. 144 sample points are then set up on the standard sphere surface and the point density of each sample point is calculated. Thus, a trace-map is represented as a 144-dimension histogram vector, and each dimension is the point density information of a specific sample point. In this way, the problem of quantitatively comparing the similarities of fiber bundles is effectively converted to comparing the similarities of 144-dimension trace-map vectors. The major advantage of the trace-map model is its capability of accurately and compactly modelling global fiber shape patterns, while allowing for normal local shape variations (Zhu et al., 2011a; Zhu et al., 2011b). Third,

for each cortical mesh vertex, we defined its structural connection pattern homogeneity as the similarity between its trace-map and the trace-maps of its morphological neighbouring vertices (3-ring cortical surface mesh, i.e. about 30 vertices). Specifically, the similarity is calculated by the Kendall's coefficient of concordance (Siegel and N. J. Castellan, 1988). Assume that k_i^j is the location of vertex j in subject i, and $tr(k_i^j)$ is the 144-dimension trace-map of k_i^j. Assume that there are Q vertices in the neighbourhood of k_i^j and they are regarded as the object q to be ranked. Each of 144 dimensions of trace-map is considered as a judge p and the number of judges is denoted by P (P=144). Define object q is given the rank $r_{q,p}$ by judge p, and t_k is the number of tied ranks in k-th of m groups of ties. The Kendall's coefficient of concordance of k_i^j is defined as

$$W\left(k_i^j\right) = \frac{12\sum_{q=1}^{Q}(\sum_{p=1}^{P} r_{q,p})^2 - 3P^2Q(Q+1)^2}{P^2\left(Q^3-Q\right) - P\sum_{k=1}^{m}\left(t_k^3 - t_k\right)} \tag{2.1}$$

The higher the Kendall's coefficient of concordance value is, the more homogeneous of the structural connection pattern of the vertex is.

We calculated the structural connection pattern homogeneity values by (2.1) for all vertices of ten model brains. As shown in Figs. 2.4c-2.4d, we can see that there are vertices (highlighted by red bubbles) with local maximum of structural connection pattern homogeneity within the roughly corresponding cortical regions across different subjects. Moreover, we defined the distance of trace-maps (Zhu et al., 2013) as

$$D(tr, tr') = \frac{\sum_{i=1}^{N}(tr_i - tr_i')^2}{N} \tag{2.2}$$

where tr and tr' are two 144-dimension trace-maps, tr_i and tr'_i are i-th element of tr and tr', and N is the number of trace-map dimensions (N=144). We found that the

structural connection patterns among the vertices with local maximum of structural connection pattern homogeneity (red bubbles) across the ten model brains have less trace-map distance, i.e., are more similar than those among the vertices in the morphological neighbourhood (e.g., in the 1-ring, 3-ring, and 5-ring surface mesh neighbourhood, highlighted by yellow, green and purple bubbles, respectively in Figs. 2.4c-2.4d) of the vertices with local maximum of structural connection pattern homogeneity. These results suggest that there are local structural connection pattern homogeneity peaks within the specific roughly corresponding cortical regions across different subjects, and importantly, these peaks exhibit more similar structural connection patterns compared to their morphological neighbourhood. As illustrated before, the high nonhomogeneity of structural connection profile of a ROI could cause uncertainties and instabilities in the discovery of consistent connectional landmarks. Therefore, in this chapter, we assumed that the identified corresponding connectional landmarks should tend to locate at the structural connection pattern homogeneity peaks in its local morphological neighbourhood for all subjects. Our premise is that those corresponding connectional landmarks which locate at the structural connection pattern homogeneity peaks tend to have less nonhomogeneity and more reproducibility, in that the cortical regions on which they locate have more homogeneous and stable fiber connection patterns, as well as inter-subject correspondences. We will integrate the structural connection pattern homogeneity information, which was not considered in our previous DICCCOL system, into our A-DICCCOL landmark optimization procedure which will be detailed in the following section.

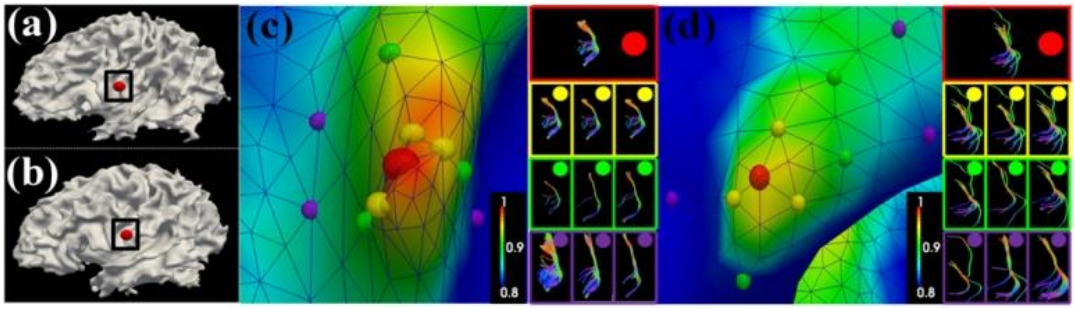

Figure 2.4. Illustration of structural connection pattern homogeneity. (a)-(b): An initialized landmark (highlighted by red bubbles) within roughly corresponding regions (highlighted by black boxes) in two model brains. (c)-(d): the zoomed views of the roughly corresponding regions within the black boxes in (a) and (b). Cortical regions are color-coded by structural connection pattern homogeneity values. The color bar is in the bottom right. The vertices with local maximum of homogeneity and other example vertices in the 1-ring, 3-ring and 5-ring neighborhood are shown in red, yellow, green and purple bubbles, respectively. The fiber shape patterns of the vertices in the left panel are shown in the right panel.

Landmark Optimization-With the availability of initialized cortical landmarks, the next step of landmark identification is to perform landmark optimization by searching all possible combinations of candidate landmark locations within their local morphological neighbourhoods in different model brains, and seeking the optimal solution with the specific constraints. In our previous DICCCOL system, we only considered the DTI-derived fiber connection pattern similarity, which was defined as the distance of 144-dimension trace-maps, as the constraint during landmark optimization to seek the optimal solution of group-wise fiber connection pattern consistency. In this chapter, we substantially improved the landmark optimization procedure by adding three

new meaningful constraints. First, the corresponding landmarks across different model brains should locate on the same clearly identifiable gyrus/sulcus before and after optimization in order to preserve the same macro-anatomical identity. Second, the corresponding landmarks should tend to locate at the vertices with local maximum of structural connection pattern homogeneity within the morphological neighbourhood. Third, the landmark should move within the morphological neighbourhood of its initial location with a predefined size during optimization to preserve the globally spatial correspondence on the cortical surface (Li et al., 2012). These three new constraints/information, as well as the DTI-derived fiber connection pattern similarity constraint adopted in previous DICCCOL system (Zhu et al., 2013), were jointly modeled and integrated together to perform landmark optimization. The goal is to search all possible combinations of candidate landmark locations within their local morphological neighbourhoods in different model brains, and to seek the optimal solution of minimizing the group-wise variance of these four jointly modelled profiles.

Specifically, assume that there are M model brains, $\tilde{k}_i^j$ is the initialized location (mesh vertex) of landmark j in brain i, and k_i^j is the candidate location in its morphological neighbourhood $C_{\tilde{k}_i^j}(\tilde{k}_i^j \in C_{\tilde{k}_i^j})$. The maximum principal curvature of k_i^j is represented by $p_{k_i^j}\begin{cases}\geq 0, & j \in gyrus \\ < 0, & j \in sulcus\end{cases}$ (Li et al., 2009) and it is used as the anatomical constraint. First, $E_S(j)$ is defined as the structural connection pattern similarity constraint to ensure that the corresponding landmark j across M model brains have similar structural connection pattern, which was also adopted in our previous DICCCOL system.

$$E_S(j) = \mathrm{var}\left(tr\left(k_1^j\right), tr\left(k_2^j\right), ..., tr\left(k_i^j\right)\right), p_{k_i^j} \begin{cases} \geq 0, \ j \in gyrus \\ < 0, \ j \in sulcus \end{cases} \quad (2.3)$$

where $tr(k_i^j)$ is the 144-dimension vector representing the trace-map of k_i^j. $var(.)$ is the variance among all trace-map vectors.

Second, $E_H(j)$ is defined as the structural connection pattern homogeneity constraint to ensure that the corresponding landmark j across M model brains should tend to move towards the location with local maximum of structural connection pattern homogeneity within its morphological neighbourhood $C_{\tilde{k}_i^j}$. After calculating the Kendall's coefficient of concordance $W(k_i^j)$ for k_i^j based on (2.1),

$$E_H(j) = \sum_{i=1}^{M}\left(1 - W\left(k_i^j\right)\right), p_{k_i^j} \begin{cases} \geq 0, \ j \in gyrus \\ < 0, \ j \in sulcus \end{cases} \quad (2.4)$$

Third, $E_D(j)$ is defined as the landmark spatial constraint to ensure that the landmark j moves within $C_{\tilde{k}_i^j}$during the optimization procedure to preserve the globally spatial correspondence on the cortical surface, which is similar to the spatial constraints used in our recent work (Li et al., 2012).

$$E_D(j) = \sum_{i=1}^{M} dist\left(k_i^j, \tilde{k}_i^j\right), p_{k_i^j} \begin{cases} \geq 0, \ j \in gyrus \\ < 0, \ j \in sulcus \end{cases} \quad (2.5)$$

where $dist(.)$ is the Euclidean distance between k_i^j and $\tilde{k}_i^j$. Mathematically, the group-wise variance of these four jointly modelled profiles is modelled as the energy E that we aim to minimize as follows based on (2.3)-(2.5):

$$E(j) = \lambda_1 E_S(j) + \lambda_2 E_H(j) + \lambda_3 E_D(j), p_{k_i^j} \begin{cases} \geq 0, \ j \in gyrus \\ < 0, \ j \in sulcus \end{cases} \quad (2.6)$$

Here, we have weights $\lambda_1 + \lambda_2 + \lambda_3 = 1$ (λ_1, λ_2 and λ_3 are between 0 and 1). Note that we adopted the grid search and ten-fold cross-validation on ten model brains to

find the optimal set of weights λ_1, λ_2 and λ_3 which have the least trace-map variance defined in (2.3) across ten model brains for each landmark. Then we searched all possible combinations of candidate landmark locations k_i^j within their local morphological neighbourhoods $C_{\tilde{k}_i^j}$ to seek the optimal solution of minimizing $E(j)$.

The energy $E(j)$ minimization was solved as follows. For each iteration, by searching the whole-space of landmarks candidate locations k_i^j in different model brains for one corresponding landmark j, we could find an optimal combination of landmark locations that minimized $E(j)$. The convergence criterion is that the Euclidean distance of landmark locations between two consecutive iterations is less than or equal to ε (ε =2mm, since the Euclidean distance between two adjacent surface mesh vertices is about 2 mm). Notably, for each iteration, if the distance between two neighbouring landmarks that are to be optimized is less than or equal to a predefined threshold t_d (t_d=2 mm, since the distance between two adjacent surface mesh vertices is about 2 mm) across all model brains, we labelled these two landmarks as 'merged', randomly discarded one of them in all model brains, and only optimized the left one in the next iteration. In our implementation, we considered about 30 candidate locations (3-ring neighborhood) for each initialized landmark. The whole algorithm is summarized below.

Algorithm I: Landmark Optimization

1: Initialization: $\tilde{k}_{0_i}^{\ j}$ is the manually initialized location of landmark j in subject i, iteration number t = 1.

2: repeat 3,4

3: $argmin_{k_i^j} E(j), k_i^j \in C_{\tilde{k}_{0_i}^{\ j}}$

4: t = t+1, $\tilde{k}_{t_i}^{\ j} = k_i^j$

5: until $\left\| \tilde{k}_{t_i}^{\ j} - \tilde{k}_{t-1_i}^{\ j} \right\| \leq \varepsilon$ (ε = 2 mm)

Landmark Determination and Prediction-To examine and ensure the reproducibility of the identified cortical landmarks, we randomly divided the ten model brains equally into two groups and performed landmark optimization separately. As a result, two independent groups of optimized corresponding connectional landmarks were obtained. Then, for each optimized corresponding landmark in all of the ten model brains in two groups, we evaluated its consistency using both quantitative (trace-map distance and fiber connection pattern homogeneity values) and qualitative (visual inspection) methods similar as in (Zhu et al., 2013; Li et al., 2012). In brief, for each corresponding landmark, we calculated the trace-map distance defined in (2.2) between any of the two brains within each of the two groups, and the mean trace-map distance of two groups were assessed to verify the similarity of the landmark across groups of brains. We also assessed the average fiber connection pattern homogeneity values of the landmark in all model brains to verify if it increased after optimization. Meanwhile, we used in-house large-scale visualization tool (Li et al., 2012) to visually confirm that the landmark preserved the same anatomical identity after optimization across all model brains. We also checked the fiber connection patterns in all model brains of two groups. If the landmark in any of the ten model brains has substantially different fiber shape patterns than others according to (Zhu et al., 2013; Li et al., 2012) based on quantitative (trace-map distance and fiber connection pattern homogeneity values) or qualitative (visual inspection) measurements, this landmark is discarded. Finally, we retained 555

connectional landmarks which exhibit reasonably accurate anatomical and connectional consistency across all ten model brains, and named these 555 landmarks as A-DICCCOL. The visualizations of all 555 A-DICCCOL landmarks have been released online at: http://dicccol.cs.uga.edu.

With the identified 555 A-DICCCOL landmarks, we were motivated to predict all 555 landmarks in a single subject's brain to verify the reproducibility and predictability of the A-DICCCOL landmarks. The prediction of A-DICCCOL landmarks in a testing brain was similar as the landmark optimization procedure. First, the testing brain was linearly registered to the same space of the model brains via FSL FLIRT and thus the A-DICCCOL landmarks in one of the model brains were roughly initialized in the testing brain. Second, the landmark optimization procedure was applied to the testing brain based on the optimized A-DICCCOL landmark locations in ten model brains. Since we already had the optimized locations of 555 A-DICCCOL landmarks in the ten model brains, we kept those optimized landmark locations in all model brains unchanged and only optimized those in the testing brain by minimizing the energy E defined in (2.6) across eleven brains (ten model brains and the testing brain). Thus, the landmark prediction procedure is fast and efficient. Specifically, assume m_1, m_2,…,m_{10} are the ten model brains and m_n is a testing brain, respectively. The landmark prediction algorithm is summarized below. It is clear that even though the performance of the prediction algorithm is dependent on the number of candidate locations in $C_{\tilde{k}_{0_n}^{\ j}}$ of m_n, it can be finished within linear time since the locations of A-DICCCOL landmarks of ten model subjects are unchanged. In practice, predicting all 555 A-DICCCOL landmarks in a testing brain takes around thirty minutes on a conventional computer at current stage.

Algorithm II: Landmark Prediction

1: m_n is linearly registered to m_1 and 555 landmarks in m_1 are roughly initialized in m_n. $\tilde{k}_{0_n}^{\ j}$ is the initial location of landmark j in m_n.

2: Construct the new group, including m_1, m_2,…, m_{10} and m_n. Keep $\tilde{k}_{0_1}^{\ j}$, $\tilde{k}_{0_2}^{\ j}$,…,$\tilde{k}_{0_{10}}^{\ j}$ be unchanged.

3: $argmin_{k_n^j} E(j), k_n^j \in C_{\tilde{k}_{0_n}^{\ j}}$

4: k_n^j with least $E(j)$ is the predicted location of landmark j in m_n.

Results

Reproducibility and Predictability of A-DICCCOL-We optimized and determined 555 consistent and corresponding A-DICCCOL landmarks in ten model brains, and further predicted 555 landmarks in all testing brains in Datasets #1-#4 (Table 2.1) with DTI data to examine the reproducibility and predictability of 555 A-DICCCOL landmarks. Fig. 2.5a shows the optimized 555 A-DICCCOL landmarks in three model brains. As an example, three of 555 landmarks are randomly selected for all model brains to examine their anatomical, structural connection pattern similarity and homogeneity consistency across different subjects in detail. First, by visual inspection, the fiber connection patterns of the same landmark across three model brains in Fig. 2.5b are similar. Quantitatively, the average trace-map distance calculated by (2.2) is 2.08, 2.18 and 2.15 within and across two groups of all ten model brains, respectively, which are considered as quite low (Zhu et al., 2013). Moreover, the consistency of fiber structural connection pattern of corresponding landmarks across different subjects is significantly

improved and shows group-wise consistency after landmark optimization than that of initialization, as illustrated in Fig. 2.6.

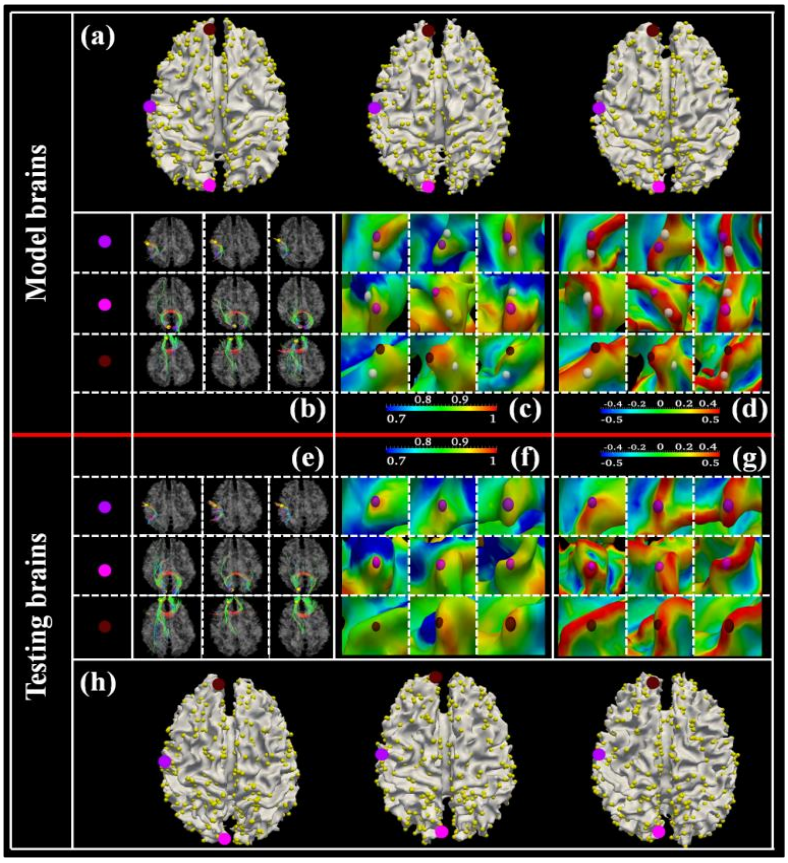

Figure 2.5. Visualization of 555 A-DICCCOL landmarks. (a) and (h): The optimized 555 landmarks in three model brains (a) and three testing brains (h), respectively. Three example landmarks are highlighted by enlarged color bubbles, respectively. (b) and (e): DTI-derived fiber connection patterns of the three example landmarks across the three model brains and three testing brains, respectively. In each sub-figure, each row represents a corresponding landmark in the model brain/testing brain. (c): The optimized locations (color bubbles) and initial locations (white bubbles) of the three landmarks on the three model brains' cortical surfaces which are color-coded by structural connection pattern homogeneity value. Each row represents a corresponding landmark in three model

brains. The color bar is at the bottom. (d): The optimized locations (color bubbles) and initial locations (white bubbles) of the three landmarks on the three model brains' cortical surfaces which are color-coded by the maximal principal curvature value. Each row represents a corresponding landmark in three model brains. The color bar is at the bottom. (f): The predicted locations (color bubbles) of the three landmarks on the three testing brains' cortical surfaces which are color-coded by structural connection pattern homogeneity value. Each row represents a corresponding landmark in three testing brains. The color bar is at the top. (g): The predicted locations (color bubbles) of the three landmarks on the three testing brains' cortical surfaces which are color-coded by the maximal principal curvature value. Each row represents a corresponding landmark in three testing brains. The color bar is at the top.

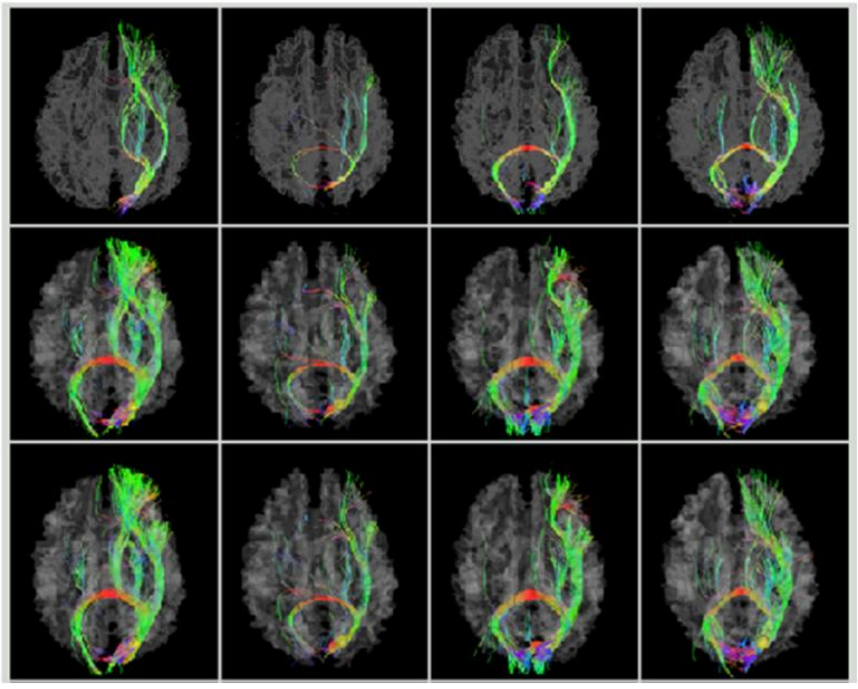

Figure 2.6. One example A-DICCCOL landmark before and after optimization. Row 1-3 show the fiber structural connection patterns of the same landmark before optimization in

four model brains, after optimization in four model brains, and in four testing brains, respectively. The landmarks are shown by the yellow bubbles.

To illustrate the effectiveness of fiber connection patterns, we also performed cortical registration via FreeSurfer based on the initialized locations of 555 A-DICCCOL landmarks on the ten model brains. In this way, we obtained a new set of 555 landmarks for each brain. Then, for each pair of corresponding landmarks based on cortical registration and the A-DICCCOL system, we calculated the Euclidean distance between the two landmarks. On average, the distance of all 555 landmarks across ten model brains is 1.54 mm, indicating that the 555 A-DICCCOL landmark locations indeed moved after adding meaningful fiber connection patterns constraints than merely anatomical constraints to improve the fiber connection correspondence. Second, in Fig. 2.5c, we can see that after landmark optimization, the three landmarks all converged to the locations with higher structural connection pattern homogeneity values than that of their initial locations, respectively. Third, in Fig. 2.5d, we can see that after optimization, the locations of three landmarks all maintained the same anatomical profiles as their initial locations, respectively. Finally, all of the 555 A-DICCCOL landmarks were evaluated and confirmed to possess the anatomical, structural connection pattern consistency across all model brains. The visualizations of structural connection patterns of all 555 A-DICCCOL landmarks have been released online at: http://dicccol.cs.uga.edu.

Moreover, Fig. 2.5h shows the predicted 555 A-DICCCOL landmarks in randomly selected three testing brains. The same three landmarks as in model brains (Fig. 2.5a) are also selected for the testing brains to examine their anatomical, structural

connection pattern similarity and homogeneity consistency across model brains and testing brains in detail. First, by visual inspection, the fiber connection patterns of the same landmark across three testing brains (Fig. 2.5e) as well as three model brains (Fig. 2.5b) are similar. Quantitatively, the average trace-map distance calculated by (2.2) is 2.14 within the three testing brains, which is similar as those in model brains and are considered as quite low (Zhu et al., 2013). Second, in Fig. 2.5f, we can see that the predicted three landmarks are all at the locations with high structural connection pattern homogeneity values in its morphological neighbourhood, respectively. Third, in Fig. 2.5g, we can see that the locations of three predicted landmarks all maintained the same anatomical profiles as those in model brains (Fig. 2.5d), respectively. Moreover, Fig. 2.7 shows that the predicted A-DICCCOL landmarks possess structural connection pattern consistency across model brains and different testing brains from the publicly released HCP high-quality DTI data (Q1 release). Finally, all of the 555 predicted A-DICCCOL landmarks were evaluated and confirmed to possess the structural connection pattern consistency across all model brains and about 120 testing brains, indicating that the A-DICCCOL system is reproducible, predictable, and reasonably represents common cortical architectures with anatomical and structural connection pattern consistency across different subjects and populations.

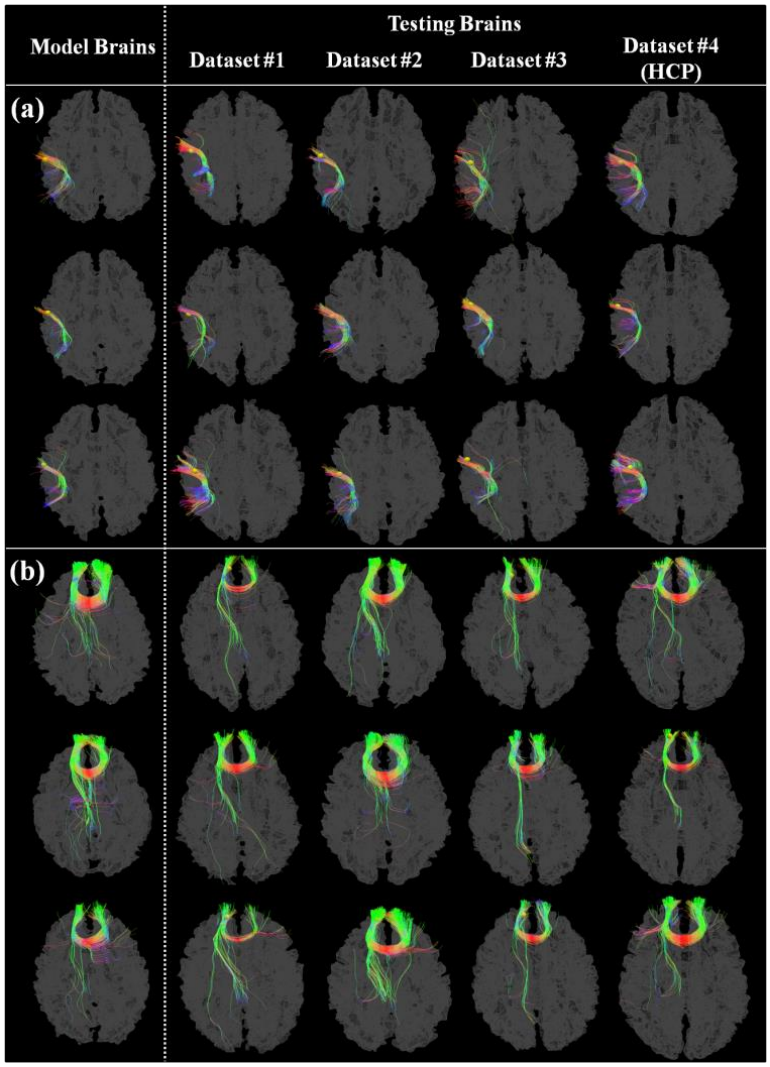

Figure 2.7. Identified A-DICCCOL landmarks in different datasets. (a)-(b): Two example A-DICCCOLs in both model brains and testing brains of four different datasets, respectively. In each sub-figure, the first column shows the fiber structural connection patterns of the same corresponding landmark in three example model brains, respectively. The second to fifth rows are the fiber structural connection patterns of the same predicted landmark in three example testing brains of Datasets #1-#4, respectively. The landmarks are shown by the yellow bubbles.

Consistency of Landmarks in HARDI Data and Using Different Fiber Tracking Software Tools-We examined the consistency of 555 DTI-derived A-DICCCOL landmarks in HARDI data because of its superior quality and capability of dealing with crossing fibers (Tuch et al., 2002). Moreover, since our A-DICCCOL landmarks identification depends on fiber structural connection patterns which might be affected by different fiber tracking strategies and software tools, we adopted five different fiber tracking software toolkits or parameter settings which more adequately account for crossing fibers (Fillard et al., 2011) on HARDI data to examine the consistency of the 555 A-DICCCOL landmarks. Note that these validations were not considered in our previous DICCCOL system (Zhu et al., 2013). Specifically, first, we initialized 555 optimized A-DICCCOL connectional landmarks on all five brains with HARDI data by linear registration (FSL FLIRT). Second, five different fiber tracking software toolkits or parameter settings (including MRtrix (Tournier et al., 2012) with three parameter settings (fiber bundle number is 10,000, 50,000 and 100,000, respectively), MEDINRIA based on q-ball imaging, and DTIStudio) were adopted to perform streamline fiber tracking on the HARDI data, respectively. Third, the landmark optimization procedure was applied to the five brains based on different fiber tracking software tools, respectively. Fig. 2.8 shows the co-visualization of 555 optimized landmarks based on DTI/HARDI data and using different fiber tracking software tools, respectively. We mapped all 555 landmarks in ten model brains and five HARDI brains using different fiber tracking software tools to the same space via linear transformation, and calculated the mean distance of any pair of locations for each corresponding landmark. The overall mean distance for all landmarks is 4.37 mm, which is relatively

small. In short, the A-DICCCOL landmarks are reasonably stable and consistent across subjects using DTI/HARDI data and different fiber tracking software tools.

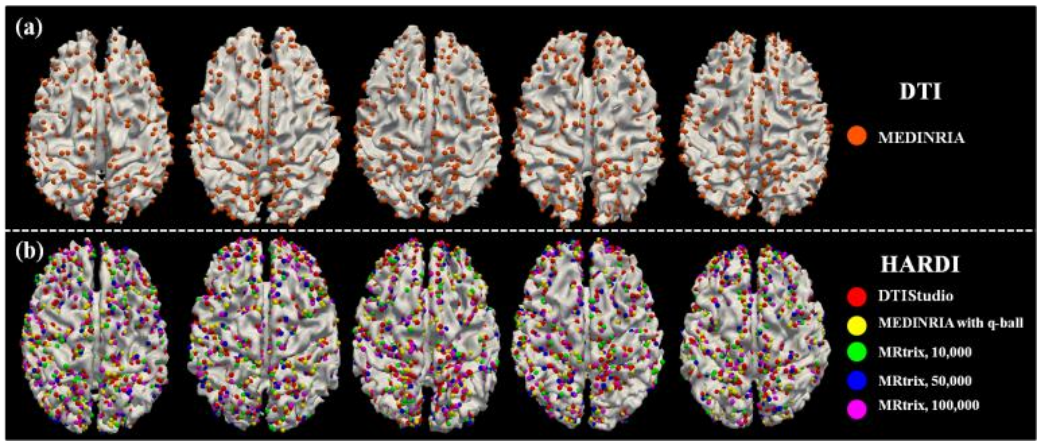

Figure 2.8. A-DICCCOLs using different fiber tracking software tools. (a) Optimized landmarks (orange bubbles) on the five model brains based on DTI data and MEDINRIA software. (b) Optimized landmarks on the five HARDI brains using different fiber tracking software tools are highlighted by red, yellow, green, blue and purple bubbles, respectively.

Functional Annotations of A-DICCCOL-Similar as in (Zhu et al., 2013), the major objective of performing functional annotations of A-DICCCOL landmarks is to demonstrate that A-DICCCOL landmarks with reasonably consistent anatomical, fiber structural connection pattern similarity and homogeneity consistency also possess corresponding functional localizations. We adopt the same method in (Zhu et al., 2013) in annotate the A-DICCCOL landmarks. It is interesting that 46 A-DICCCOL landmarks were annotated and consistently co-localized in one or more 46 identified functional activation peaks based on the five task fMRI datasets across different subjects and/or populations as shown in Fig. 2.9. We measured the Euclidean distance between each

annotated A-DICCCOL landmark and corresponding functional activation peak, and reported the results in Fig. 2.9. The mean distances for the five functional activation maps are 6.27 mm, 5.68 mm, 6.38 mm, 5.91 mm, and 6.33 mm, respectively. On average, the distance is 6.11 mm. Furthermore, we measured the functional annotation accuracy of the same identified functional activation peaks by our previous DICCCOL to have a comparison with A-DICCCOL. Specifically, for previous DICCCOL, the mean distances for the five task fMRI datasets are 6.50 mm, 6.12 mm, 5.93 mm, 6.25 mm, and 6.41 mm, respectively. On average, the distance is 6.24 mm, indicating that A-DICCCOL has higher functional annotation accuracy than previous DICCCOL. Moreover, we compared the mean distance of each functional activation peak of all five functional activation maps with the corresponding annotated A-DICCCOL landmark before and after optimization, and generated by a random perturbation. The results are 6.78 mm, 6.11 mm and 7.12 mm, respectively, indicating that in general, our optimized A-DICCCOL landmarks have better functional annotation accuracy than the landmarks before optimization or generated by a random perturbation. In conclusion, A-DICCCOL system also reasonably represents functional correspondences across different subjects and populations.

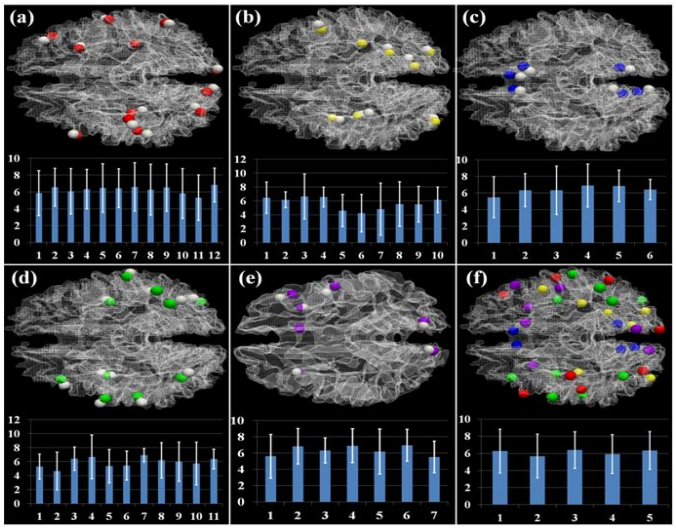

Figure 2.9. Functional annotations of A-DICCCOL landmarks. (a)-(e): Semantic decision making, emotion, empathy, fear and working memory activation map, respectively. In each sub-figure, the functional activation peaks are highlighted by white bubbles, while the corresponding annotated A-DICCCOL landmarks are other color bubbles. The mean distance and standard deviation between each pair of functional activation peak and annotated landmark are shown in the histogram in the bottom panel, in which the horizontal axis indexes activation peaks and the vertical axis represents the distance (mm). (f): all of the functionally annotated landmarks and the mean distance and standard deviation of each functional activation map.

Comparisons with Image Registration Algorithms-We compared the functional annotation accuracies of functional activation peaks by our A-DICCCOL landmarks and with those by five representative different volumetric/surface registration algorithms. For volumetric registration, we adopted four algorithms including one linear FSL FLIRT (Jenkinson and Smith, 2001) and three nonlinear ones: FSL FNIRT (Andersson et al., 2008), ANTS (Avants et al., 2008), and HAMMER (Shen and Davatzikos, 2002). For surface-based registration, we used the FreeSurfer nonlinear algorithm (Fischl et al., 1999). The working memory functional activation map regions were used as the benchmark for comparisons here. Specifically, the A-DICCCOL annotation error is defined as the mean Euclidean distance between each pair of the annotated A-DICCCOL landmark and corresponding functional activation peak. The image registration based annotation error is defined as the mean Euclidean distance between the transformed fMRI activation peaks from individual brains to the MNI

standard space via different registration methods and the centers of these multiple brains' transformed fMRI activation peaks. The average annotation errors in all subjects by the six methods are 6.33 mm, 7.76 mm, 8.01 mm, 7.74 mm, 7.73 mm and 7.16 mm, respectively. The results show that our A-DICCCOL landmarks have higher functional annotation accuracy than these five image registration algorithms. Note that the above compared image registration algorithms were designed for anatomical alignments, but not specifically for cortical landmark localization. If those image registration algorithms are optimized by taking the advantage of multimodal data in the future, their accuracies for landmark localization could be better than what was reported in this chapter.

Discussion and Conclusion

In this chapter, we presented a novel approach that identified 555 connectional cortical landmarks that turn out to be reproducible, predictable and exhibit reasonably accurate anatomical, fiber connection pattern similarity and homogeneity consistency across individuals and populations. Moreover, a portion of the connectional landmarks were functionally annotated, demonstrating the reasonably functional correspondences of our connectional landmarks. We named these 555 connectional landmarks, which were generated by different and substantially improved strategies and procedures from our previous DICCCOL system, as anatomy-guided DICCCOL or A-DICCCOL. This A-DICCCOL system can be potentially used to report, integrate, transfer, and compare different measurements of the structural and functional properties of the brain, e.g., morphological measurements derived from structural MRI data and functional measurements derived from resting state fMRI data.

The presented A-DICCCOL system can be possibly further improved in the following directions in the future. First, we can potentially integrate parts of the strategies adopted in DICCCOL and A-DICCCOL systems together to identify more consistent connectional landmarks. We believe that the identified 555 landmarks in A-DICCCOL are still a portion of all consistent landmarks across human brains. For example, the random initialization used in our previous DICCCOL system might be implemented prudentially to complement the interactive initialization in our A-DICCCOL system by considering landmark initialization positions in the banks in-between the gyral crowns and sulcal fundi. In this case, additional consistent connectional landmarks can be possibly discovered in cortical regions that A-DICCCOL has not considered. Moreover, there might potentially be more consistent cortical landmarks to be identified and discovered in the future, if we improve our discovery procedures in other aspects. For instance, an improvement we can possibly make is to integrate additional constraints into the optimization procedure, e.g., functional homogeneity (Craddock et al., 2012), in the future. Second, the functional annotations of A-DICCCOL landmarks are still far from being comprehensive and systematic. Though the preliminary results are encouraging, in the future, more specific, large-scale task fMRI datasets should be designed and performed for the purpose of functional annotation of our A-DICCCOL landmarks. In addition, we can consider leveraging existing rich fMRI literature and existing databases such as the BrainMap data (Laird et al., 2009) to perform functional annotations of the discovered A-DICCCOL landmarks. As a result, the functional meanings of the A-DICCCOL landmarks can be then interpreted and applied in neuroscience applications. Once the anatomical, DTI-derived fiber structural connection pattern, and functional

correspondences of the A-DICCCOL landmarks are established across individuals and populations, the A-DICCCOL system will offer a general platform to examine functional interaction (Sun et al., 2012) and dynamics (Hu et al., 2011) of the brain.

This chapter has been focused on the presentation of methodologies and validation studies of the A-DICCCOL system, and the potential of its application in neuroscience and neuroimaging fields are left to our other studies. In short, the A-DICCCOL based representation of reasonably common cortical architecture offers a principled approach and a generic platform to share, exchange, integrate, and compare multimodal neuroimaging datasets across laboratories, and we predict that public release of our A-DICCCOL system (http://dicccol.cs.uga.edu) will stimulate and enable various collaborative efforts in brain sciences, as well as contributing to data-driven discovery brain imaging studies.

Acknowledgement

T. Liu was supported by NSF CAREER Award (IIS-1149260), NIH R01 DA-033393, NIH R01 AG-042599, and NSF CBET-1302089. L. Guo was supported by NSFC 61273362 and NSFC 61333017. T. Zhang and J. Lv were supported by the China Government Scholarship and the Doctorate Foundation of Northwestern Polytechnical University. The authors would like to thank C. Faraco and L. S. Miller for sharing the working memory task design and the associated DTI/T-fMRI data.

CHAPTER 3

HOLISTIC ATLASES OF FUNCTIONAL NETWORKS AND INTERACTIONS (HAFNI) ON CORTICAL SURFACE[2,3]

[2]Xi Jiang, Xiang Li, Jinglei Lv, Tuo Zhang, Shu Zhang, Lei Guo, and Tianming Liu. 2015. Sparse Representation of HCP Grayordinate Data Reveals Novel Functional Architecture of Cerebral Cortex. *Human Brain Mapping*. 36(12): 5301-19.

[3]Jinglei Lv*, Xi Jiang*, Xiang Li*, Dajiang Zhu*, Shu Zhang, Shijie Zhao, Hanbo Chen, Tuo Zhang, Xintao Hu, Junwei Han, Jieping Ye, Lei Guo, and Tianming Liu. * indicates co-first authors. 2015. Holistic Atlases of Functional Networks and Interactions Reveal Reciprocal Organizational Architecture of Cortical Function. *IEEE Transactions on Biomedical Engineering*. 62(4):1120-31, 2015.

Abstract

It has been largely unknown to what extent multiple functional networks spatially overlap/interact with each other and jointly realize the total cortical function. In this chapter, by developing novel sparse representation of whole-brain fMRI signals, we show that a number of reproducible and robust functional networks, including both task-evoked and resting state networks, are simultaneously distributed in distant neuroanatomic areas and substantially spatially overlapping with each other, thus forming an initial collection of holistic atlases of functional networks and interactions (HAFNI). Specifically, we apply the HAFNI framework on the recently publicly released Human Connectome Project (HCP) high-quality grayordinate fMRI data to identify those concurrent functional networks on the cortical surface.

Introduction

Understanding the organizational architecture of cortical function has been of intense interest since the inception of human neuroscience. After decades of active research using in-vivo functional neuroimaging techniques such as fMRI (Heeger and Ress, 2002), there has been mounting evidence (Fedorenko et al., 2013; Fox et al., 2005; Dosenbach et al., 2006; Duncan, 2010; Pessoa, 2012) showing that the brain function emerges from and is realized by the interaction of multiple concurrent neural processes or networks, each of which is spatially distributed across specific structural substrate of neuroanatomical areas (Bullmore and Sporns, 2009; Huettel et al., 2004). However, it is still challenging to robustly and faithfully reconstruct concurrent functional networks

from fMRI (either task fMRI (tfMRI) or resting state fMRI (rsfMRI)) data and quantitatively measure their network-level interactions. The critical lack of this key knowledge might be the underlying fundamental barrier to rigorously answering this long-standing debate in human neuroscience (Kanwisher, 2010): is the functional human brain architecture composed of a collection of highly specialized components, each responsible for a dedicated aspect of human function, or is the brain architecture more of a general-purpose machinery, each component of which involved in a wide range of functional processes?

For tfMRI, despite the remarkable successes and significant neuroscientific insights achieved by traditional GLM based subtraction approach (Friston et al., 1994; Worsley, 1997), it has been recognized and pointed out in the literature that spatially overlapping networks subserving different functions are possible to go unnoticed by the blocked subtraction paradigms and the associated analysis methods such as GLM (Logothetis, 2008; Krekelberg et al., 2006). Meanwhile, from a human neuroscience perspective, it has been widely reported and argued that a variety of cortical regions and networks exhibit strong functional diversity and heterogeneity (Fedorenko et al., 2013; Duncan, 2010; Pessoa, 2012; Kanwisher, 2010; Anderson et al., 2013; Gazzaniga, 2004), that is, a cortical region could participate in multiple functional domains/processes and a functional network might recruit various heterogeneous neuroanatomic areas. Therefore, it is unlikely that current subtraction-based tfMRI data analysis methods are sufficient to reconstruct concurrent spatially-overlapping functional networks and then to address the fundamental question of whether the functional brain architecture is composed of highly-specialized components, or is a general-purpose machinery, or is somewhere in-between.

Besides tfMRI for studying task-evoked cortical function, rsfMRI has arguably been another major neuroimaging technique to examine the intrinsic functional activities of the human brain (Biswal, 2012; Fox and Raichle, 2007; Biswal et al., 1997). Recently, a variety of computational methods, such as independent component analysis (ICA) (Beckmann et al., 2005; Calhoun et al., 2004), normalized cut (Van den Heuvel et al., 2008) or other clustering algorithms (Chen et al., 2013), have been employed to map resting state networks (RSNs) in healthy brains or neurological/psychiatric disorders, and many interesting results have been reported (Fox and Raichle, 2007; Biswal et al., 1997; Biswal et al., 2011; Xu et al., 2013). However, there has been limited knowledge about to what extent the reconstructed RSNs spatially overlap with each other and jointly realize resting state brain function. In addition, there has been increasing interest in examining the relationship or interaction between task-evoked networks and intrinsic RSNs in the literature (Raichle, 2010).

In order to address the abovementioned fundamental questions, in this chapter, we developed a novel computational framework of sparse representations of whole-brain fMRI signals. The basic idea is to aggregate all of hundreds of thousands of tfMRI or rsfMRI signals within the whole brain of one subject into a big data matrix, which is subsequently factorized into an over-complete dictionary basis matrix and a reference weight matrix via an effective online dictionary learning algorithm (Wright et al., 2009; Mairal et al., 2010). Then, the time series of each over-complete basis dictionary represents the functional BOLD (blood-oxygen-level dependent) activities of a brain network and its corresponding reference weight vector stands for the spatial map of this brain network. A particularly important characteristic of this framework is that the

decomposed reference weight matrix naturally reveals the spatial overlap/interaction patterns among reconstructed brain networks. Specifically, we apply this framework on the recently publicly released large-scale Human Connectome Project (HCP) grayordinate fMRI data (Q1 release) (Barch et al., 2013) to identify the concurrent functional networks on cortical surfaces.

Materials and Methods

'Grayordinate' Data Acquisition and Preprocessing-We adopt the high-quality task-based fMRI (tfMRI) data from the Human Connectome Project (HCP) (Q1 release) (Van Essen et al., 2013; Barch et al., 2013). HCP provides publicly available and easy-to-use multi-modality MRI neuroimaging datasets for multi-modal analysis of brain structure, connectivity, and function, as well as comparisons across subjects. Specifically, the HCP tfMRI datasets include seven different task paradigms (emotion, gambling, language, motor, relational, social, and working memory) which are adopted or designed to identify core functional nodes across a wide range of cerebral cortex, thus can be viewed as a comprehensive and systematic mapping of core functional nodes and functional networks across subjects (Barch et al., 2013). The detailed designs of the seven task paradigms are referred to in (Barch et al., 2013).

There are 68 subjects in the Q1 release of HCP tfMRI datasets (Van Essen et al., 2013; Barch et al., 2013). The acquisition parameters of tfMRI data are as follows: 90×104 matrix, 220mm FOV, 72 slices, TR=0.72s, TE=33.1ms, flip angle = 52°, BW =2290 Hz/Px, in-plane FOV = 208 × 180 mm, 2.0 mm isotropic voxels (Barch et al., 2013). We adopt the publicly released preprocessed tfMRI data after the minimal preprocessing pipelines which are especially defined for high spatial and temporal

resolution of HCP datasets (Glasser et al., 2013). The minimal preprocessing pipelines mainly include spatial artifacts and distortions removal, cortical surfaces generation, within-subject cross-modal registration, cross-subject registration to standard volume and surface spaces, and generation of a CIFTI format of preprocessed data in the standard grayordinate space (Glasser et al., 2013). In brief, gray matter is modeled as combined cortical surface vertices and subcortical voxels, and the term "grayordinates" is adopted to describe the spatial dimension of such combined coordinate system. The standard grayordinate space means that the cortical surface mesh and subcortical volume parcels are both in the MNI standard space. There are 91,282 maximally aligned grayordinates in total (including the gray matter sampled at about 60k surface vertices in the standard 2 mm average vertex spacing on the cortical surface and about 30k standard 2 mm voxels in subcortical regions) across all subjects and data modalities (Glasser et al., 2013). The grayordinate-based tfMRI data is represented as a 2D matrix in CIFTI format, in which one dimension represents the standard grayordinates (spatial information) which have correspondence across subjects and the other dimension represents the tfMRI time series (Barch et al., 2013; Glasser et al., 2013).

Sparse Representation of Grayordinate-based Whole-brain TfMRI Signals- We perform dictionary learning and sparse representation of grayordinate-based whole-brain tfMRI data to obtain a comprehensive collection of dictionary components (functional networks) in the whole brain for each subject in each task data. As illustrated in Fig. 3.1, for each subject in each task data, first, we extract tfMRI signals of whole-brain grayordinates (Fig. 3.1a). After normalizing to zero mean and standard deviation of 1, all tfMRI signals are aggregated into a 2D signal matrix $\mathbf{X} = [\mathbf{x}_1, ..., \mathbf{x}_n] \in R^{t \times n}$ (Fig.

3.1b), where *t* is the tfMRI time points and *n* columns are *n* tfMRI signals extracted from *n* grayordinates. Then **X** is factorized into an over-complete dictionary basis matrix $\mathbf{D} = [\mathbf{d}_1, ..., \mathbf{d}_k] \in R^{t \times k}$ (Fig.1c, *k* is the dictionary component size) and a sparse coefficient weight matrix $\boldsymbol{\alpha} = [\boldsymbol{\alpha}_1, ..., \boldsymbol{\alpha}_n] \in R^{k \times n}$ (Fig. 3.1c) via an effective online dictionary learning algorithm (Mairal et al., 2010), in which the tfMRI signal vector $\mathbf{x}_i$ (*i*=1,...*n*) in *i*-th column of **X** is approximately modeled as $\mathbf{x}_i = \mathbf{D} \times \boldsymbol{\alpha}_i$, where $\boldsymbol{\alpha}_i$ (*i*=1,...*n*) is the *i*-th column of **α**. Specifically, each dictionary component can be viewed as a functional network from brain science perspective, i.e., the time series vector $\mathbf{d}_i$ (*i*=1,...*k*) in *i*-th column of **D** represents the functional BOLD activities of *i*-th functional network (the blue curves in Figs.3.1e-3.1f), while $\mathbf{d}_i$'s corresponding sparse coefficient weight vector $\boldsymbol{\alpha}^i$ (*i*=1,...*k*) in *i*-th row of **α** can be mapped back to the cortical surface to obtain the cortical spatial pattern of the functional network (Figs.3.1e-3.1f). At the conceptual level, the computational framework of sparse representation can not only accurately and compactly represent tfMRI signals, but also effectively identify a comprehensive collection of functional networks whose temporal ($\mathbf{d}_i$) and spatial ($\boldsymbol{\alpha}^i$) patterns can be quantitatively assessed.

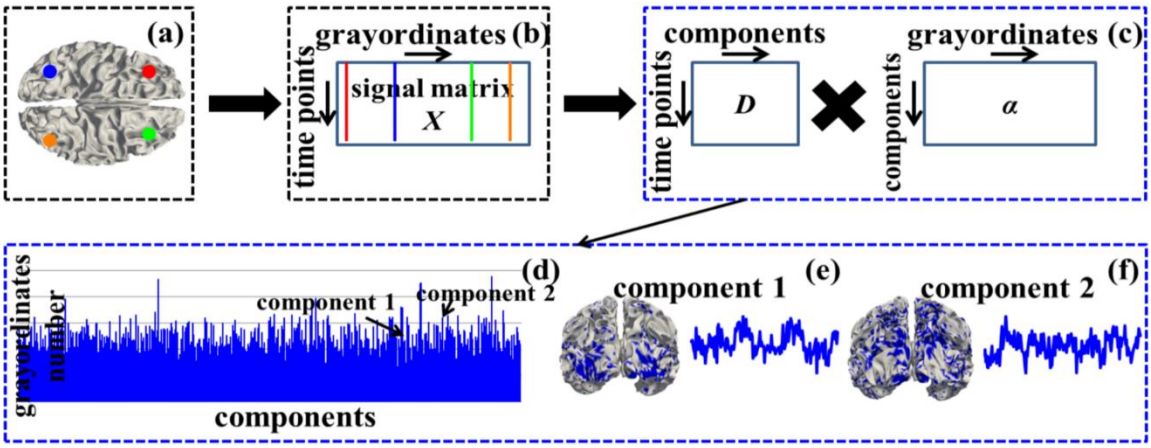

Figure 3.1. Sparse representation of whole-brain grayordinate tfMRI signals. (a): The cortical surface of an example subject in the MNI152 standard grayordinate space. Four example grayordinates are highlighted by four different colors (red, blue, green and orange). (b): The grayordinate tfMRI data matrix X of the subject in (a). Four corresponding tfMRI signals of the four example grayordinates in (a) are represented as straight lines by the same color. (c): Sparse representation of X as dictionary D × sparse coefficient weight matrix α. (d)-(f): Illustrations of D and α. The blue bars in (d) show dictionary components (indexed horizontally) and the number of grayordinates that each dictionary component contains by counting the number of non-zero elements in each row of α (vertical height). (e)-(f) show spatial distribution map on the cortical surface (highlighted by blue) and temporal time series (blue curve) of two example dictionary components, respectively.

We calculate $\mathbf{D}$ and $\boldsymbol{\alpha}$ as follows. For sparse representation of signal matrix $\mathbf{X} \in R^{t\times n}$, we aim to learn an effective over-complete dictionary $\mathbf{D} \in R^{t\times k}$ which satisfies the constraint that $k>t$ and $k<<n$ (Mairal et al., 2010). Specifically, the empirical cost function $f_n(\mathbf{D})$ of $\mathbf{X} \in R^{t\times n}$ considering the average loss of regression to all n signal vectors using D is

$$f_n(\mathbf{D}) = \frac{1}{n}\sum_{i=1}^{n} \ell\left(\mathbf{x}_i, \mathbf{D}\right) = \frac{1}{n}\sum_{i=1}^{n} \min_{\boldsymbol{\alpha}_i \in R^k} \frac{1}{2}\left\|\mathbf{x}_i - \mathbf{D}\boldsymbol{\alpha}_i\right\|_2^2 + \lambda\left\|\boldsymbol{\alpha}_i\right\|_1 \tag{3.1}$$

where the loss function $\ell\left(\mathbf{x}, \mathbf{D}\right)$ is defined as the optimal value of sparse representation: $\ell\left(\mathbf{x}, \mathbf{D}\right) = \min_{\boldsymbol{\alpha}\in R^k} \frac{1}{2}\left\|\mathbf{x} - \mathbf{D}\boldsymbol{\alpha}\right\|_2^2 + \lambda\left\|\boldsymbol{\alpha}\right\|_1$. Note that the value of $\ell\left(\mathbf{x}, \mathbf{D}\right)$ should be small if

signal $\mathbf{x}$ is reasonably well sparse represented by **D**. The l_1 regularization is used to yield a sparse resolution of $\boldsymbol{\alpha}$. λ is a regularization parameter between regression residual and sparsity level. Moreover, we have the constraint to prevent the elements in **D** from being arbitrarily large,

$$C = \left\{ \mathbf{D} \in R^{t \times k} s.t. \forall i = 1,..k, \mathbf{d}_i^T \mathbf{d}_i \leq 1 \right\} \tag{3.2}$$

So the problem of minimizing Eq. (3.1) is rewritten as a matrix factorization problem:

$$\min_{\mathbf{D} \in C, \boldsymbol{\alpha} \in R^{k \times n}} \frac{1}{2} \left\| \mathbf{X} - \mathbf{D}\boldsymbol{\alpha} \right\|_F^2 + \lambda \left\| \boldsymbol{\alpha} \right\|_{1,1} \tag{3.3}$$

We adopt the effective online dictionary learning algorithm and the associated publicly released online dictionary learning toolbox (Mairal et al., 2010) to solve Eq. (3.3) and to learn the dictionary **D**. We briefly demonstrate the online dictionary learning approaches to solve Eq. (3.3) as follows. The core idea is that the two variables D and α in Eq. (3.3) are alternated and minimized over one while keeping the other one fixed. Specifically, we define signal training set as samples of a distribution $p(\mathbf{x})$. $\mathbf{D}_m$ is defined as the updated dictionary at the iteration time *m*. $\mathbf{D}_0$ is the initial dictionary and is randomly initialized from $\mathbf{x}$. At the number of iterations *m*, for one element $\mathbf{x}_m$ drawn from $p(\mathbf{x})$ at a time in stochastic gradient descent, the least angle regression (LARS)-Lasso algorithm (Mairal et al., 2010) is used to compute the decomposition $\boldsymbol{\alpha}_m$ of $\mathbf{x}_m$ based on the dictionary $\mathbf{D}_{m-1}$ obtained at the previous iteration *m*-1. At the same time, the dictionary $\mathbf{D}_{m-1}$ is updated as $\mathbf{D}_m$ by minimizing over Eq. (3.2) the function in Eq. (3.1), where $\boldsymbol{\alpha}_m$ is computed during previous step. The block-coordinate descent with warm

starts algorithm is used for dictionary update (Mairal et al., 2010). It has been proven that the iterations of dictionary update can achieve convergence to learn an optimal D. More detailed equations and solutions of Eq. (3.3) are referred to (Mairal et al., 2010). Once **D** is learned and fixed in Eq. (3.3), the sparse representation based on the learned **D** can be solved as an l_1-regularized linear least-squares problem to learn an optimized $\boldsymbol{\alpha}$ (Mairal et al., 2010). We select the value of regularization parameter λ and dictionary size *k* via experimental results based on the criterion of group-wise consistency of the inferred functional components across individual subjects (Lv et al., 2015a; Lv et al., 2015b).

Identification of Functional Networks in Sparse Representation-Once we perform dictionary learning and sparse representation of tfMRI signals to obtain a collection of dictionary components for each subject in each task data, the next step is to identify and quantitatively characterize the meaningful functional networks (including both task-evoked networks and RSNs or called intrinsic connectivity networks (ICNs)) from the dictionary components as many as possible for each subject in each task data based on current brain science knowledge, and to seek their correspondences across individual subjects. Specifically, we identify the task-evoked networks from the dictionary components for each subject in each tfMRI data as follows. After extensive visual inspection, it is found that certain networks (dictionary components) have similar spatial and temporal patterns compared with the activation maps derived from traditional general linear model (GLM) (Friston et al., 1994). In this way, we adopt the traditional GLM to perform task activation detection on tfMRI data via FSL FEAT software. The resulting activation maps under specific task contrast designs as well as the input task contrast paradigm curves in traditional GLM can be viewed as the references to identify

and characterize task-evoked networks in sparse representation. For *i*-th dictionary component, we not only measure the temporal similarity (defined as Pearson's correlation coefficient) between its temporal vector $\mathbf{d}_i$ and each task contrast paradigm curve, but also measure the spatial similarity between its spatial pattern $\boldsymbol{\alpha}^i$ and the corresponding activation map obtained by GLM. The spatial similarity is defined as the spatial pattern overlap rate *R* between the dictionary component's spatial pattern (*S*) and the GLM-derived activation map (*T*) on cortical surface:

$$R(S,T) = \frac{|S \cap T|}{|T|} \tag{3.4}$$

Note that we firstly convert S and T from continuous values to discrete labels (all values larger than 0 are labeled as 1, and others are labeled as 0) and then calculate the spatial overlap rate using Eq. (3.4). For each subject, we select the top ten candidate dictionary components which have high spatial similarity with corresponding GLM-derived activation map and have high temporal similarity with corresponding task contrast paradigm curve, respectively. Each component with high sum of value in spatial and temporal similarity is further examined by a group of seven experts separately to determine the final component with the best match of both spatial and temporal patterns with GLM based on the agreement reached by a voting procedure of all experts. Moreover, for a specific task data, we examine the group consistency of each identified meaningful task-evoked network across all subjects by comparing the spatial and temporal patterns between group-averaged identified meaningful task-evoked networks and activation maps derived from group GLM, and only those consistent dictionary components across subjects are retained as identified task-evoked networks in the

specific task data. Our rationale is that since temporal and spatial patterns provide crucial and complementary information of functional BOLD activities and neuroanatomic distributions of a functional network, respectively, each identified meaningful task-evoked network in sparse representation should have both high temporal similarity with the task contrast paradigm curve and high spatial similarity with the activation map obtained from traditional GLM.

Moreover, we identify the intrinsic connectivity networks (ICNs) (Seeley et al., 2007; Raichle 2010; Smith et al., 2009) from the dictionary components for each subject in each task data as follows. We measure the spatial similarity defined in Eq. (3.4) between dictionary components and previously identified ICN templates to determine the correspondence. Specifically, ten previously well-defined ICNs (Smith et al., 2009) are adopted as ICN templates in this chapter. We select the top ten candidate dictionary components which have high spatial similarity with each ICN template, respectively. Each component is further examined by a group of seven experts separately to determine the final component with the best match of spatial pattern and ICN template based on the agreement reached by a voting procedure of all experts. Moreover, we examine the group consistency of each identified ICN across all subjects and all task data by comparing the spatial pattern between group-averaged identified ICN and corresponding ICN template, and only those consistent dictionary components across subjects and across task data are retained as identified ICNs. Our rationale is that each identified ICN in sparse representation should have high spatial similarity (overlap rate) with the corresponding previously identified ICN template across different subjects.

It should be noted that since there is no quantitative or effective interpretation of the comprehensive collection of all dictionary components identified by sparse representation of tfMRI signals, we adopt the traditional GLM-derived contrast maps and ICN templates as the independent references to identify those similar meaningful functional networks from the dictionary components, as well as to confirm that those meaningful functional networks indeed 'exist' in human brain no matter what methods are adopted based on current brain science knowledge. It should also be noted that in the future, all of those hundreds of dictionary components (task-evoked or ICNs, or even noise and artifacts) should be identified with future understanding of human brain function and development of other effective methodology.

Results

Identification of Meaningful Functional Networks in Sparse Representation- We identified 3, 2, 2, 5, 2, 3, and 6 task-evoked networks from the datasets of emotion, gambling, language, motor, relational, social, and working memory task, respectively. Figs. 3.2a-3.2b show an example consisting of the three identified task-evoked networks in emotion tfMRI data. Specifically, Fig. 3.2a shows the three task-evoked networks in emotion tfMRI data of one example subject. We can see that all three networks have similar spatial patterns compared with corresponding GLM-derived activation maps as well as similar temporal patterns compared with the corresponding task contrast paradigm curve. Quantitatively, the spatial overlap rate R is 0.30, 0.33, and 0.29, and the temporal similarity is 0.38, 0.30, and 0.37 for the three networks in the example subject, respectively. Fig. 3.2b shows the group-averaged spatial maps and temporal curves of identified task-evoked networks across all subjects in emotion task. Table 3.1 provides

the spatial overlap rates and temporal similarity values of all group-averaged task-evoked networks in seven tasks, indicating that all identified task-evoked networks are consistent and have relatively high spatial overlap rate and temporal similarity across subjects.

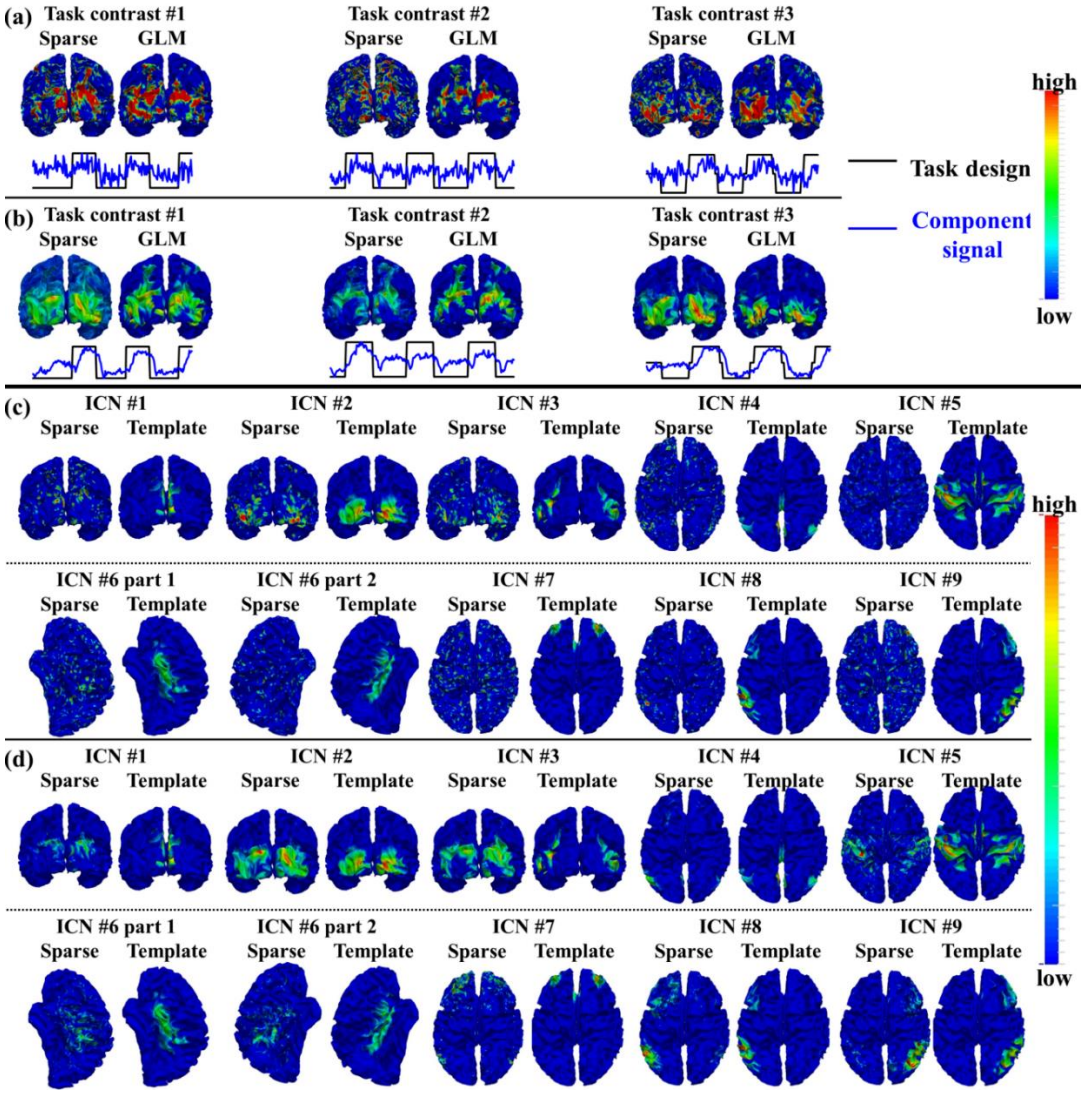

Figure 3.2. Identified task-evoked networks and ICNs in sparse representation of emotion tfMRI data. (a) Spatial and temporal patterns of the three identified task-evoked networks based on sparse representation compared with traditional GLM-derived activation maps and task contrast paradigm curves in one example subject. (b) Group-averaged spatial and temporal patterns of the three identified task-evoked networks compared with group

GLM-derived activation maps and task contrast paradigm curves across all subjects. (c) Spatial patterns of nine identified ICNs in sparse representation compared with ICN templates in the example subject. (d) Group-averaged spatial patterns of the nine identified ICNs compared with ICN templates across all subjects.

Table 3.1. Spatial overlap rate (S) and temporal similarity (T) of all identified group-averaged task-evoked networks (N) comparing with group GLM-derived activation maps.

	Emotion		Gambling		Language		Motor		Relational		Social		WM	
	S	T	S	T	S	T	S	T	S	T	S	T	S	T
N#1	0.84	0.63	0.97	0.42	0.95	0.46	0.95	0.62	0.90	0.44	0.97	0.54	0.94	0.51
N#2	0.92	0.55	0.95	0.23	0.86	0.55	0.95	0.58	0.92	0.43	0.94	0.62	0.89	0.47
N#3	0.79	0.68					0.94	0.56			0.94	0.69	0.98	0.59
N#4							0.83	0.62					0.94	0.46
N#5							0.94	0.57					0.90	0.47
N#6													0.92	0.61

Moreover, we identified nine ICNs in all subjects and in all seven tasks. Fig. 3.2c shows the spatial maps of the nine identified ICNs compared with ICN templates (Smith et al., 2009) in the emotion task of the example subject. Quantitatively, the spatial overlap rate is 0.34, 0.51, 0.37, 0.28, 0.27, 0.27, 0.23, 0.33, and 0.29 for the nine ICNs, respectively. Fig. 3.2d shows the group-averaged spatial maps of identified ICNs in emotion data across all subjects. Table 3.2 provides the spatial overlap rate of all group-averaged ICNs, indicating that all identified ICNs are consistent and have relatively high spatial overlap rate across tasks and subjects.

Table 3.2. Spatial overlap rates of all identified group-averaged ICNs.

	Emotion	Gambling	Language	Motor	Relational	Social	WM
ICN#1	0.70	0.88	0.99	0.98	0.84	0.97	0.90
ICN#2	0.96	0.94	0.98	0.97	0.97	0.97	0.96
ICN#3	0.79	0.91	0.97	0.94	0.84	0.95	0.87
ICN#4	0.69	0.79	0.86	0.85	0.75	0.84	0.71
ICN#5	0.52	0.86	0.91	0.93	0.81	0.92	0.75
ICN#6	0.44	0.85	0.92	0.93	0.81	0.92	0.72
ICN#7	0.45	0.67	0.79	0.74	0.62	0.76	0.62
ICN#8	0.69	0.90	0.97	0.92	0.84	0.91	0.81
ICN#9	0.64	0.89	0.95	0.93	0.84	0.92	0.82

Discussion and Conclusion

In this chapter, we decomposed fMRI signals into linear combinations of multiple components based on sparse representation of whole-brain fMRI signals. This novel data-driven strategy, called HAFNI, naturally accounts for that a brain region might be involved in multiple functional processes, and thus its fMRI signal is composed of various components. Experimental results have shown that this HAFNI framework can effectively and robustly reconstruct both consistent meaningful task-evoked networks and ICNs on cortical surface across all subjects and seven tasks in HCP grayordinate tfMRI datasets. There are still many other network components remaining to be characterized and interpreted. These networks could be unknown networks or just noise networks, which need effective methodology to explore in the future. It will also be invaluable to further assess possible alterations of HAFNI components and interactions in brain disorders such as Alzheimer's disease and Schizophrenia.

Acknowledgement

T. Liu was supported by NSF CAREER Award (IIS-1149260), NIH R01 DA-033393, NIH R01 AG-042599, and NSF CBET-1302089. L Guo was supported by NSFC 61273362 and NSFC 61333017. J Lv and T Zhang were supported by the China Government Scholarship and the Doctorate Foundation of NWPU.

CHAPTER 4

A FUNCTIONAL MODEL OF CORTICAL GYRI AND SULCI

4.1 Motivation

As demonstrated in Chapter 1, Diffusion tensor imaging (DTI) has been widely adopted in the brain mapping field to study the macro-scale brain structural fiber connections. Our recent studies (Nie et al. 2012; Chen et al. 2013) have demonstrated that the diffusion imaging (including DTI and HARDI) derived streamline fiber terminations concentrate on gyral regions, rather than sulcal regions in human, chimpanzee, and macaque brains. This finding reveals the structural connection patterns of cortical gyri and sulci, and suggests that gyri might be the structural connection centers of the cerebral cortex. In this chapter, we are inspired to investigate the functional connection patterns of cortical gyri and sulci based on multi-modal DTI and fMRI data. Notably, the joint modeling and analysis of multimodal DTI and fMRI data together can elucidate the structural architectures and functional mechanisms of the human brain simultaneously.

4.2 A Functional Connectivity Model of Cortical Gyri and Sulci

In order to address the concern as mentioned in Chapter 4.1, we propose a novel functional connectivity model of cortical gyri and sulci (Deng et al., 2014). As illustrated in Fig. 4.1 (Deng et al., 2014), we hypothesize that gyri are global functional connection centers and sulci are local functional units. Specifically, gyral regions (highlighted as red) exchange information between distant structurally-connected gyral regions via dense

fibers (highlighted as black curves), while sulcal regions communicate directly with the neighboring gyral regions through inter-column cortico-cortical fibers and communicate indirectly with distant regions via the neighboring gyral regions and the dense fibers (Deng et al., 2014).

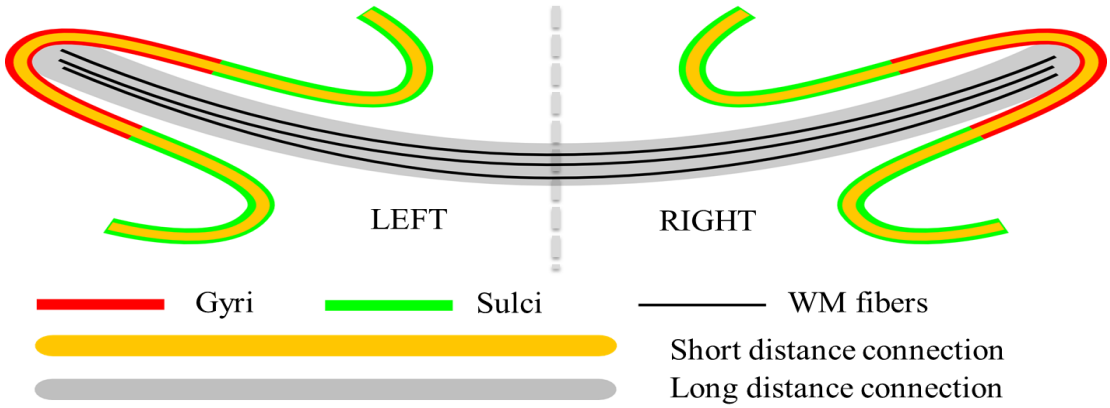

Figure 4.1. Illustration of the functional connectivity model of cortical gyri and sulci (Deng et al., 2014, Fig. 1. Reprinted here with permission of the publisher).

4.3 Methods

We examine and validate the proposed model in Fig. 4.1 by assessing the structural and functional connectivity among cortical gyral and sulcal regions as follows. We adopt the developed A-DICCCOL system in Chapter 2 as the representation of cortical gyral and sulcal regions. The rationale is that as demonstrated in Chapter 2, the A-DICCCOL system provides large-scale consistent cortical landmarks on major cortical gyral and sulcal regions which have anatomical, structural, and functional correspondences across different subjects. It can benefit the assessment of structural/functional connectivity among cortical gyral and sulcal regions of one subject, and group-wise analysis and comparison across different subjects. Specifically, first, we

identify A-DICCCOL landmarks for each subject using the methods in Chapter 2. Second, we extract the structural and functional information for each landmark respectively. The structural information is the DTI-derived fiber bundles connected to the landmark, and the functional information is the averaged resting state fMRI (rsfMRI) signal within the neighbourhood of this landmark (Deng et al., 2014). Third, for each possible pair of the A-DICCCOL landmarks which have the gyral/sulcal information, we measure the structural/ functional connectivity. The structural connectivity strength is defined as the number of DTI-derived fiber bundles connected to the two landmarks. The functional connectivity strength is defined as the Pearson correlation value between the two rsfMRI signals of two landmarks. The structural/functional connectivity is normalized by the averaged structural/functional connectivity strength among all landmark pairs for each subject in order to have a fair comparison among different subjects (Deng et al., 2014). In this way, a value of 1.0 represents the average structural/functional connectivity. The larger the value is, the stronger the structural/functional connectivity is.

4.4 Results

The structural and functional connectivity is measured between gyral-gyral, gyral-sulcal, and sulcal-sulcal landmark pairs. Table 4.1 reports the overall structural/functional connectivity value which is defined as the ratio of the survived number of landmark pairs after thresholding using a value of 1.0 as discussed in Chapter 4.3 to the total number of landmark pairs. We can see that the overall functional connectivity value is significantly strong in gyral-gyral landmark pairs, weak in sulcal-sulcal landmark pairs, and moderate

in gyral-sulcal landmark pairs. The detailed distribution histograms of the functional connectivity of the three landmark pair types are shown in Fig. 4.2. The above findings validate the proposed functional connectivity model of cortical gyri and sulci in Fig. 4.1 that gyri are global functional connection centers and sulci are local functional units. We can also see that the overall structural connectivity is significantly strong in gyral-gyral landmark pairs, weak in sulcal-sulcal landmark pairs, and moderate in gyral-sulcal landmark pairs. This finding demonstrates the structural substrates of the functional connectivity differences among gyral and sulcal regions.

Table 4.1. Overall functional and structural connectivity value of all gyral-gyral, gyral-sulcal, and sulcal-sulcal landmark pairs (Deng et al., 2014, Table 1. Reprinted here with permission of the publisher). Statistically significant items are underlined (p-value<0.05, mean=1.0). Con stands for connectivity, Stdev stands for standard deviation, and p stands for p-value.

Con / Sub	Overall Functional Connectivity Value			Overall Structural Connectivity Value		
	Gyrus-Gyrus	Gyrus-Sulcus	Sulcus-Sulcus	Gyrus-Gyrus	Gyrus-Sulcus	Sulcus-Sulcus
1	0.54	0.41	0.29	0.19	0.09	0.03
2	0.40	0.37	0.33	0.15	0.06	0.01
3	0.50	0.43	0.35	0.16	0.07	0.03
4	0.56	0.46	0.35	0.13	0.05	0.01
5	0.53	0.47	0.38	0.14	0.06	0.02
6	0.48	0.47	0.44	0.14	0.05	0.02
7	0.42	0.40	0.32	0.12	0.06	0.03
8	0.59	0.53	0.43	0.12	0.05	0.01
9	0.39	0.40	0.34	0.15	0.14	0.10
10	0.49	0.46	0.41	0.21	0.09	0.03
11	0.42	0.44	0.40	0.19	0.09	0.01
Mean	0.48	0.44	0.37	0.15	0.07	0.03
Stdev	0.07	0.04	0.05	0.03	0.03	0.03
Two-sample statistical significance test without equal variance assumption						
Test	Gyrus-Gyrus>Gyr	Gyrus-Gyrus>Sulcu	Gyrus-Sulcus>Sulc	Gyrus-Gyrus>Gyr	Gyrus-Gyrus>Sulc	Gyrus-Sulcus>Sulc

	us-Sulcus	s-Sulcus	us-Sulcus	us-Sulcus	us-Sulcus	us-Sulcus
p	**0.04**	**1.21e-04**	**9.39e-04**	**9.57e-07**	**5.75e-10**	**3.52e-04**

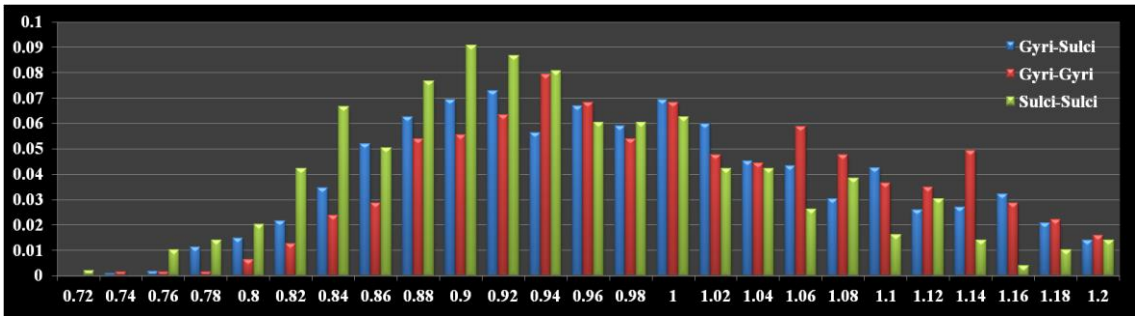

Figure 4.2. Distribution histograms of the functional connectivity of gyral-gyral, gyral-sulcal, and sulcal-sulcal landmark pairs (Deng et al., 2014, Fig. 4. Reprinted here with permission of the publisher).

CHAPTER 5

SPARSE REPRESENTATION OF HCP GRAYORDINATE DATA REVEALS NOVEL FUNCTIONAL ARCHITECTURE OF CEREBRAL CORTEX[4]

[4]Xi Jiang, Xiang Li, Jinglei Lv, Tuo Zhang, Shu Zhang, Lei Guo, and Tianming Liu. 2015. *Human Brain Mapping*. 36(12): 5301-19.

Abstract

The recently publicly released Human Connectome Project (HCP) grayordinate-based fMRI data not only has high spatial and temporal resolution, but also offers group-corresponding fMRI signals across a large population for the first time in the brain imaging field, thus significantly facilitating mapping the functional brain architecture with much higher resolution and in a group-wise fashion. In this chapter, we adopt the HCP grayordinate task-based fMRI (tfMRI) data to systematically identify and characterize task-based heterogeneous functional regions (THFRs) on cortical surface, i.e., the regions that are activated during multiple tasks conditions and contribute to multiple task-evoked systems during a specific task performance, and to assess the spatial patterns of identified THFRs on cortical gyri and sulci by applying a computational framework of sparse representations of grayordinate brain tfMRI signals as detailed in Chapter 3. Experimental results demonstrate that both consistent task-evoked networks and intrinsic connectivity networks across all subjects and tasks in HCP grayordinate data are effectively and robustly reconstructed. Moreover, it is found that there are relatively consistent THFRs locating at bilateral parietal lobe, frontal lobe, and visual association cortices across all subjects and tasks. Particularly, those identified THFRs locate significantly more on gyral regions than on sulcal regions. These results based on sparse representation of HCP grayordinate data reveal novel functional architecture of cortical gyri and sulci, and might provide a foundation to better understand functional mechanisms of the human cerebral cortex in the future.

Introduction

Studying human brain function using in-vivo functional neuroimaging techniques such as functional magnetic resonance imaging (fMRI) (Logothetis, 2008; Friston, 2009) has received significant interest in the brain mapping field. Specifically, task-based fMRI (tfMRI) has been widely adopted to identify brain regions that are functionally involved in a specific task performance (Logothetis 2008; Friston 2009). To advance the understanding of functional localizations and interactions within the human brain based on fMRI data, there have been increasing efforts in acquiring and processing fMRI data with higher spatial/temporal resolution and correspondence across subjects and populations to better characterize the regularity and variability of human brain function (Van Essen et al., 2013). One of such efforts is the recently publicly released Human Connectome Project (HCP) grayordinate-based fMRI data (Van Essen et al., 2013; Smith et al., 2013; Barch et al., 2013; Glasser et al., 2013). The HCP grayordinate data models the gray matter as combined cortical surface vertices and subcortical voxels across subjects in the standard MNI152 space (Smith et al., 2013; Glasser et al., 2013). The HCP fMRI (including tfMRI and resting state fMRI) data in the standard grayordinate space not only has both much higher spatial and temporal resolution, but also offers group-corresponding fMRI signals across a large population for the first time in the brain imaging field. In short, the HCP grayordinate fMRI data significantly facilitates the mapping of functional brain architecture with much higher resolution and in a group-wise fashion, without the need to average signals within brain regions and across subjects (Mikl et al., 2008; Yue et al., 2010).

Based on tfMRI data, various studies (e.g., Huettel et al., 2004; Fox et al., 2005; Dosenbach et al., 2006; Bullmore and Sporns 2009; Lv et al., 2014a; Lv et al., 2014b) have demonstrated that there exist multiple concurrent functional networks that are spatially distributed across brain regions and are involved and interacting with each other. This phenomenon is in agreement with studies in the neuroscience field which have been widely reported and argued that there are certain brain regions and networks that exhibit strong functional heterogeneity and diversity (Duncan 2010; Fedorenko et al., 2013; Pessoa 2012; Kanwisher 2010; Anderson et al., 2013; Gazzaniga 2004). That is, a brain region might be involved in multiple functional processes simultaneously, and a functional network might recruit heterogeneous brain regions. For instances, it was argued that "neural basis of emotion and cognition should be viewed as governed less by properties that are intrinsic to specific sites and more by interactions among multiple brain regions" (Pessoa 2012) and that "areas of the brain that have been associated with language processing appear to be recruited across other cognitive domains" (Gazzaniga 2004). In short, identifying and characterizing such meaningful task-based heterogeneous functional regions (THFRs) on cerebral cortex, i.e., the cortical regions that are activated during multiple tasks conditions and contribute to multiple task-evoked systems during a specific task performance, could be important to understanding the functional architecture of human cerebral cortex. However, those meaningful THFRs with complex temporal patterns due to the complex composition of involved multiple functional networks/processes might have been underestimated by traditional approaches which merely consider individual tfMRI signals based on model-driven subtraction procedures (Lv et al., 2015a; Lv et al., 2015b).

Motivated by the above-mentioned reasons and based on the high-quality HCP grayordinate tfMRI data, this chapter aims to identify and characterize the meaningful THFRs on cortical surface during a specific task performance, and to assess the possible distribution difference of identified THFRs on cortical gyral and sulcal regions. The recently publicly released HCP tfMRI data in the standard grayordinate space (Van Essen et al., 2013; Glasser et al., 2013; Barch et al., 2013) is particularly suitable for this study due to the following three reasons. 1) It is well demonstrated (e.g., Van Essen et al., 2013; Smith et al., 2013; Glasser et al., 2013) that it is of great importance to analyze cortical neuroimaging data with surface constraint information since the convoluted cortical sheet and its geometry information is better represented in 2D surface space than in commonly adopted 3D volume space. 2) The HCP grayordinate tfMRI data can sufficiently differentiate gyral/sulcal regions and relatively reliably map the tfMRI time series on cortical gyral and sulcal regions. While for the commonly used tfMRI data in 3D volume space, the possible functionally distinct regions across gyral blades or sulcal banks are only separated by a few voxels (millimeters). It is possible that the tfMRI time series from functionally distinct gyral/sulcal regions are mixed when performing 3D volumetric smoothing processing and thus inaccurate for succeeding analysis (Glasser et al., 2013). 3) The HCP grayordinate tfMRI data has both high spatial and temporal resolution than the commonly used tfMRI data, and the spatial correspondence of the standard grayordinate tfMRI data is relatively more precise than aligned 3D volume data across different subjects (Glasser et al., 2013), and the associated tfMRI signals of grayordinates also have relatively precise correspondence across subjects, which is suitable for cross-subject comparison and group-wise analysis. In short, using HCP

grayordinate-based tfMRI data will significantly benefit us to identify THFRs reliably and assess their spatial patterns on cortical gyri and sulci accurately in this chapter.

It is the first time (as far as we know) to assess the spatial patterns of task-based heterogeneous functional regions on cortical gyri and sulci, the results of which could provide a foundation for future exploration of functional architecture of the human cerebral cortex.

Methods

Identification of THFRs and Assessment of Spatial Patterns on Gyri/Sulci- After performing sparse representation of tfMRI signals and characterizing the meaningful functional networks based on HCP grayordinate tfMRI data as detailed in Chapter 3, we identify task-based heterogeneous functional regions (THFRs) and assess their spatial patterns on cortical gyri/sulci for each subject in each task data. Specifically, since the dictionary components can be viewed as functional networks and the *i*-th column $\boldsymbol{\alpha}_i$ (i=1,...n) of $\boldsymbol{\alpha}$ represents the functional network composition of grayordinate g_i (i=1,...n), we assess the number of involved functional networks (dictionary components) of g_i by counting the number of non-zero elements in $\boldsymbol{\alpha}_i$ ($\|\boldsymbol{\alpha}_i\|_0$). THFR is then defined as:

$$THFR = \forall g_i s.t. \|\boldsymbol{\alpha}_i\|_0 > q \tag{5.1}$$

In brief, THFR is composed of a collection of grayordinate g_i (i=1,...n) of which the number of non-zero elements (i.e., the number of involved functional networks) in $\boldsymbol{\alpha}_i$ is larger than a threshold q. Note that since we define q as the value of $\|\boldsymbol{\alpha}_i\|_0$ at the top p% across all grayordinates, the value of q is determined once value of p% is decided.

The rationale of choosing value of *p*% is that *p*% should be small enough to identify the THFRs from all grayordinates, while *p*% should also not be too small to identify merely isolated brain grayordinates instead of continues THFR regions. We test different *p*% to examine the spatial pattern consistency of identified THFRs. Note that we adopt a uniform *p*% for all tfMRI data and subjects since the values of $\|\boldsymbol{\alpha}_i\|_0$ across all voxels/grayordinates are typically normally distributed with similar mean and standard deviation across all subjects as illustrated in (Lv et al., 2015b). It should also be noted that it is likely that the identified THFRs contain specific artifact or noise components which cannot be well quantitatively characterized or modeled under current brain science knowledge. However, the results show that the identified THFRs are indeed meaningful and contain multiple identified functional networks.

After obtaining the spatial distribution of THFRs on grayordinate cortical surfaces, the further spatial pattern assessment of THFRs on gyri/sulci is straightforward. As each grayordinate already has the gyri/sulci information in each subject (Glasser et al., 2013), we could count the number of involved grayordinates in THFRs on gyral and sulcal regions respectively, then assess the ratio between the percentage of involved grayordinates in THFRs on gyri vs the percentage on sulci.

Results

Identification of THFRs in Single Task and Multiple Tasks-We identified THFRs in each single task. Fig. 5.1 shows the distribution density map of identified THFRs across subjects in each single task. In brief, since the grayordinates have correspondence across all subjects, for each task, we combine the distribution map of identified THFRs of all subjects together by counting the number of each grayordinate in

the THFRs of all subjects, and calculating the mean number of each grayordinate in the THFRs to obtain the distribution density map of identified THFRs across subjects. We see that THFRs have higher distribution density at the bilateral parietal lobe, frontal lobe, and visual association cortices within each single task. Moreover, such high distribution density pattern is relatively consistent across seven tasks (as highlighted by the red arrows in Fig. 5.1). These findings are also consistent across all individual subjects.

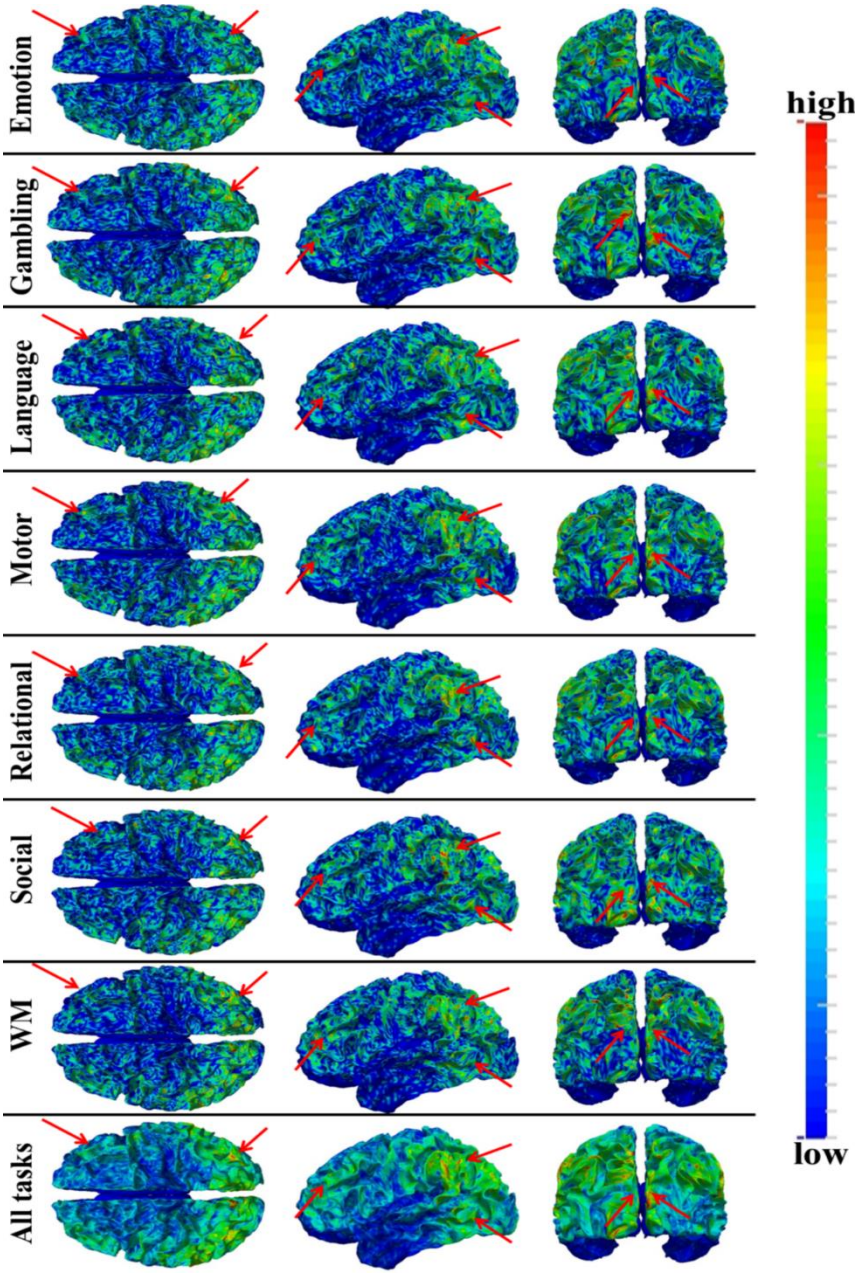

Figure 5.1. Distribution density map of identified THFRs across all subjects in each of the seven tfMRI data. Those THFRs with higher distribution density and relatively consistent across seven tasks are highlighted by red arrows.

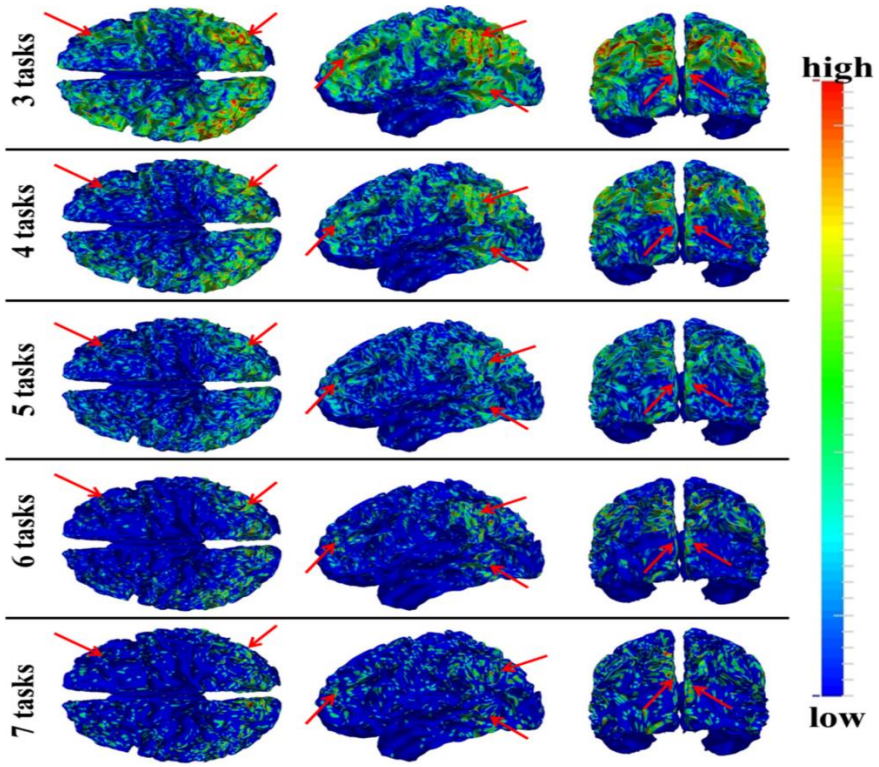

Figure 5.2. Distribution density map of identified THFRs of all subjects across multiple tasks (at least 3 of 7 tasks in HCP data (emotion, gambling, language, motor, relational, social, and working memory)). Those THFRs with higher distribution density and relatively consistent across multiple tasks are highlighted by red arrows.

Moreover, we identified THFRs across multiple tasks for each subject. Fig. 5.2 shows the distribution density map of identified THFRs of all subjects across multiple tasks (at least 3-7 tasks), respectively. In brief, since the grayordinates have correspondence across all subjects, for each situation (across 3 to 7 tasks), we combine

the distribution map of identified THFRs of all subjects together by counting the number of each grayordinate in the THFRs of all subjects, and calculating the mean number of each grayordinate in the THFRs to obtain the distribution density map of identified THFRs across all subjects. Interestingly, the THFRs also have higher distribution density at the bilateral parietal lobe, frontal lobe, and visual association cortices. Moreover, the higher distribution density pattern is relatively consistent across from at least three tasks to at least seven tasks (as highlighted by red arrows in Fig. 5.2) as those in single task (Fig. 5.1). These findings are also consistent across all subjects.

We quantitatively characterized the identified THFRs via two measurements. First, Figs. 5.3a and 5.3c show the network histograms (by counting the number of involved dictionary components (functional networks)) after normalization to the sum of 1 in THFRs and task-evoked networks of the example subject in emotion data, respectively. We can see that the histogram of THFRs (Fig. 5.3a) is complex and distributed across all components, while the histogram of task-evoked networks highly concentrates on the specific components (highlighted by black in Fig. 5.3c), as expected. Quantitatively, the network histogram concentration (defined as summing the percentage of top three components in the histogram) is 1.22% and 8.11% for THFRs and task-evoked networks in the example subject in emotion data, respectively. Table 5.1 provides the histogram concentration of THFRs and task-evoked networks in all seven tasks across all subjects. We can see that the histogram concentration value of THFRs is statistically significantly smaller than that of task-evoked networks ($p < 0.05$) across all seven tasks and subjects by using paired t-test. Moreover, the network histogram entropy (defined as the entropy of all histogram elements (Lv et al., 2015b)) is 8.62 and 8.34 for THFRs and

task-evoked networks in the example subject in emotion data, respectively. Table 5.2 shows the histogram entropy of THFRs and task-evoked networks in all seven tasks across all subjects. We can see that the histogram entropy of THFRs is statistically significantly larger than that of task-evoked networks ($p < 0.05$) across all seven tasks and subjects by using paired t-test. Second, we examined the temporal patterns of THFRs and compared with those of task-evoked networks within the same subject. As shown in Fig. 5.3b, the temporal patterns of all THFRs as well as two example components (R4 and R5) in THFRs of the example subject in emotion data are complex and have much less similarity with the task contrast paradigm curves, while the temporal patterns of the top three components in the histogram of task-evoked networks have high similarity with the task contrast paradigm curves (Fig. 5.3d). Quantitatively, the mean temporal similarity for the temporal pattern of all THFRs and two example components (R4 and R5) is only 0.01, -0.06, and 0.01 compared with the three task contrast paradigm curves, respectively, while 0.38, 0.30, and 0.37 for the top three components in the histogram of task-evoked networks in the same subject, respectively.

Table 5.1. Network histogram concentration of THFRs and task-evoked networks (%) in seven tasks across all subjects. The value is represented as mean±standard deviation. Bold values indicate p-values smaller than 0.05.

	Emotion	Gambling	Language	Motor	Relational	Social	WM
THFRs	1.44±0.17	1.35±0.16	1.26±0.11	1.31±0.15	1.42±0.20	1.38±0.16	1.19±0.09
Task-evoked	7.20±1.38	4.16±0.55	3.06±0.14	4.77±0.89	4.75±0.75	4.27±0.53	3.50±0.44
p-value	**3.53E-42**	**9.04E-46**	**1.45E-64**	**1.15E-39**	**1.17E-43**	**2.19E-47**	**2.94E-48**

Table 5.2. Network histogram entropy of THFRs and task-evoked networks in seven tasks across all subjects. The value is represented as mean±standard deviation. Bold values indicate p-values smaller than 0.05.

	Emotion	Gambling	Language	Motor	Relational	Social	WM
THFRs	8.61±0.01	8.62±0.01	8.62±0.00	8.62±0.01	8.61±0.01	8.62±0.01	8.63±0.00
Task-evoked	8.41±0.07	8.56±0.02	8.60±0.01	8.52±0.05	8.52±0.03	8.56±0.02	8.56±0.03
p-value	**6.28E-32**	**1.89E-31**	**6.74E-35**	**8.68E-24**	**5.86E-29**	**3.87E-32**	**3.18E-28**

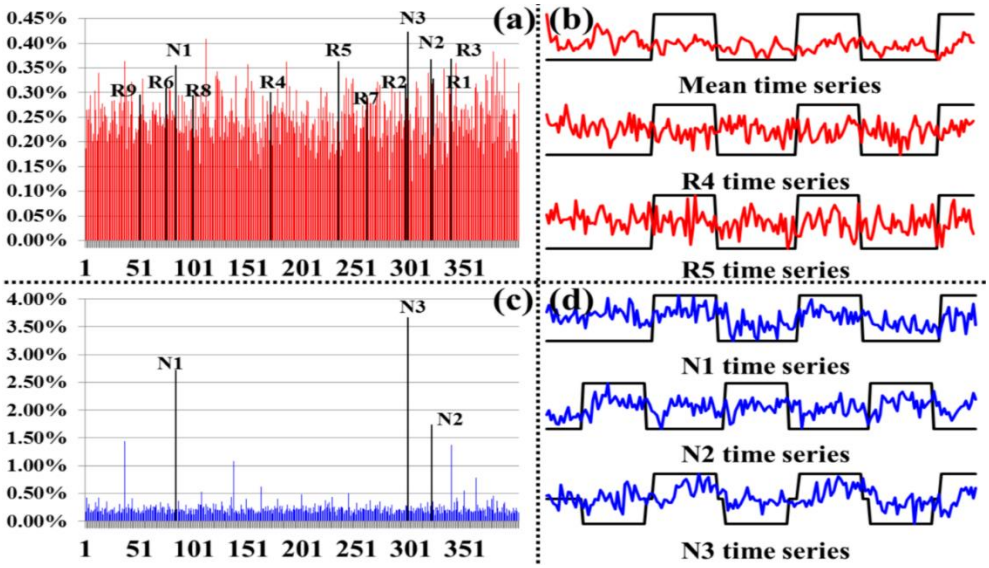

Figure 5.3. Network histogram and temporal pattern comparisons between THFRs and task-evoked networks. (a) Network histogram (red) after normalization to the sum of 1 in THFRs of an example subject in emotion data. (b) Mean temporal pattern of identified THFRs (red) and temporal patterns of two example components identified as ICN #4 and ICN #5 in Fig. 3.2 (R4 and R5). The task contrast paradigm curve is shown in black. (c) Network histogram (blue) after normalization to the sum of 1 in task-evoked networks of an example subject in emotion data. Here the task-evoked networks are the union of three

identified task-evoked networks. (d) Temporal patterns of three components identified as task-evoked networks in Fig. 3.2 (N1, N2, and N3). The task contrast paradigm curve is shown in black.

Spatial Patterns of THFRs on Cortical Gyri and Sulci-First, we assessed the spatial patterns of identified THFRs in each single task on cortical gyri and sulci. From Figs. 5.4 and 5.5, we can see that the mean percentage of involved grayordinates in THFRs on gyri is consistently larger than that on sulci in all seven tasks and all subjects. Moreover, we calculated the ratio of percentage of involved grayordinates in THFRs on gyri vs that on sulci across all subjects and tasks. Table 5.3 provides the mean ratio of percentage of involved grayordinates in THFRs on gyri vs that on sulci in seven tasks. We can see that the percentage of involved grayordinates in THFRs on gyri is statistically significantly larger than that on sulci ($p < 0.05$) across all subjects in all seven tasks by using paired t-test. The mean ratio of percentage of involved grayordinates in THFRs on gyri vs that on sulci is 2.22, 3.14, 2.63, 2.95, 3.38, 2.50, and 2.76 in seven tasks, respectively.

Table 5.3. Mean ratio of percentage of involved grayordinates in THFRs on gyri vs that on sulci across all subjects in seven tasks. The ratio is represented as mean±standard deviation. Bold values indicate p-values smaller than 0.05.

	Emotion	Gambling	Language	Motor	Rational	Social	WM
Ratio	2.22±1.09	3.14±3.87	2.63±2.07	2.95±2.47	3.38±4.29	2.50±1.32	2.76±1.59
p-value	**9.48E-22**	**9.60E-19**	**2.98E-20**	**1.56E-19**	**1.49E-17**	**8.25E-22**	**8.29E-22**

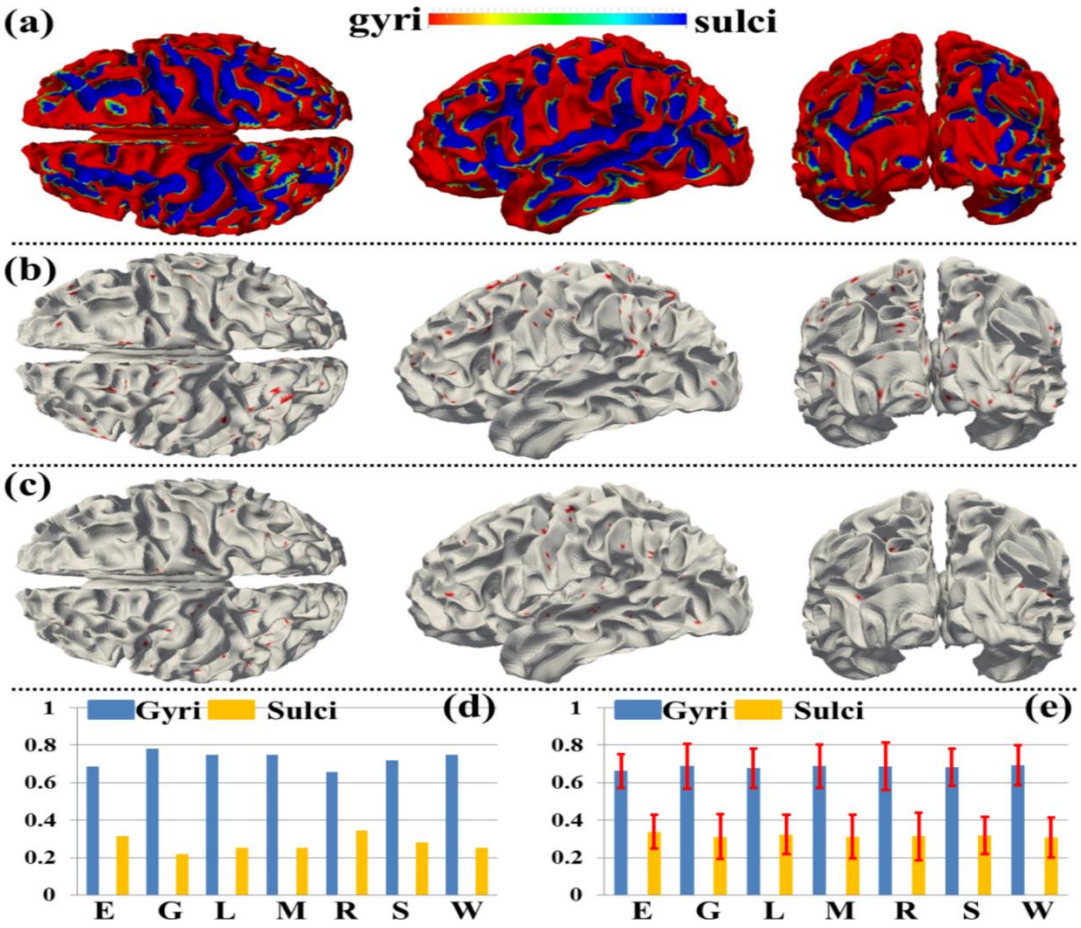

Figure 5.4. Spatial patterns of THFRs in single task on gyri/sulci and the percentages of involved grayordinates in THFRs in single task on gyri/sulci. (a): Segmented gyri and sulci of one example subject. (b)-(c): Spatial patterns of THFRs (red) on gyri (b) and sulci (c) in emotion task data of the example subject, respectively. (d) Percentages of involved grayordinates in THFRs on gyri/sulci in the example subject in all seven tasks. (e) Mean percentages of involved grayordinates in THFRs on gyri/sulci across all subjects in all seven tasks (E: emotion; G: gambling; L: language; M: motor; R: relational; S: social; W: working memory).

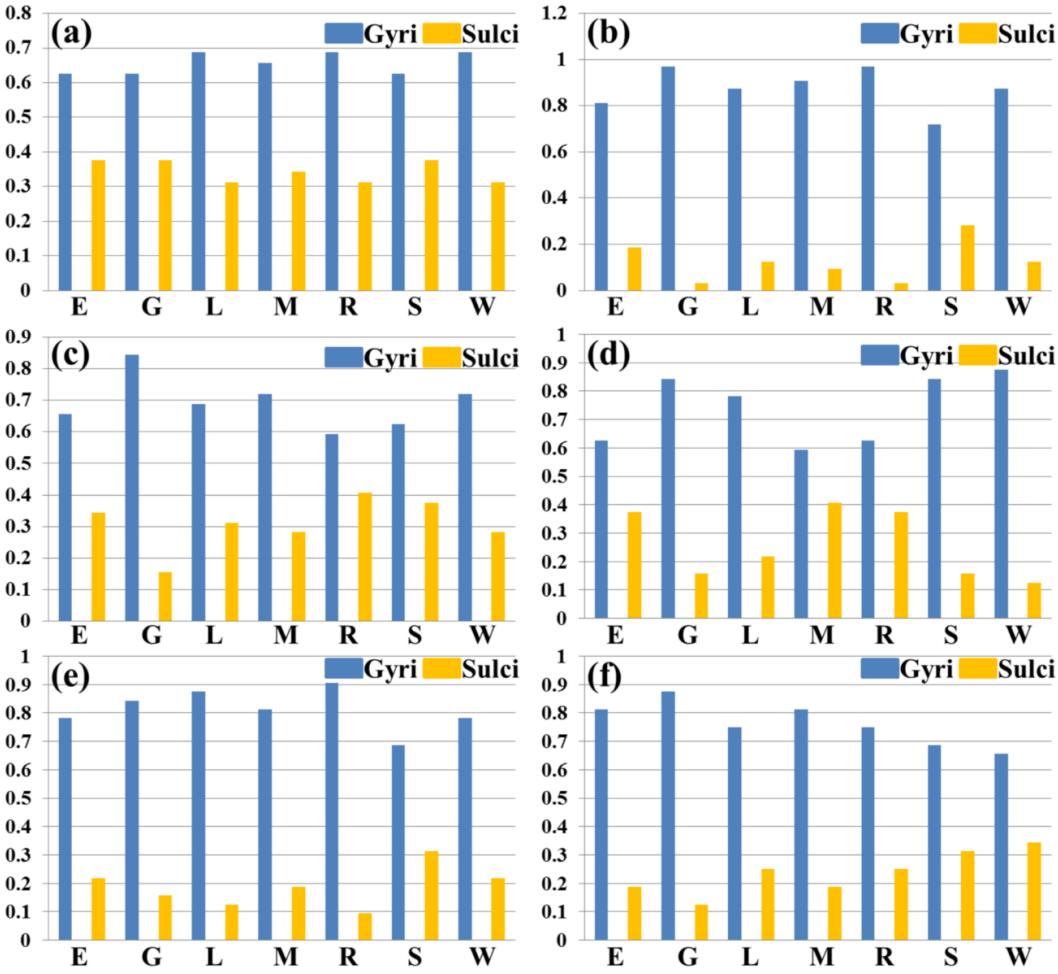

Figure 5.5. Percentages of involved grayordinates in THFRs in single task on gyri/sulci of another six subjects indexed by (a)-(f), respectively. (E: emotion; G: gambling; L: language; M: motor; R: relational; S: social; W: working memory)

Moreover, we assessed the spatial patterns of identified THFRs across multiple tasks on cortical gyri and sulci. From Figs. 5.6 and 5.7, we can see that the percentage of involved grayordinates in THFRs across multiple tasks on gyri is consistently larger than that on sulci. We further calculated the ratio of percentage of involved grayordinates in THFRs on gyri vs that on sulci for all subjects. Table 5.4 provides the mean ratio of percentage of involved grayordinates in THFRs on gyri vs that on sulci across all

subjects. We can see that the percentage of involved grayordinates in THFRs across multiple tasks on gyri is statistically significantly larger than that on sulci ($p < 0.05$) across all subjects by using paired t-test. Moreover, the more tasks are involved, the larger the mean ratio of percentage of involved grayordinates in THFRs on gyri vs that on sulci is (except for 6 tasks and 7 tasks).

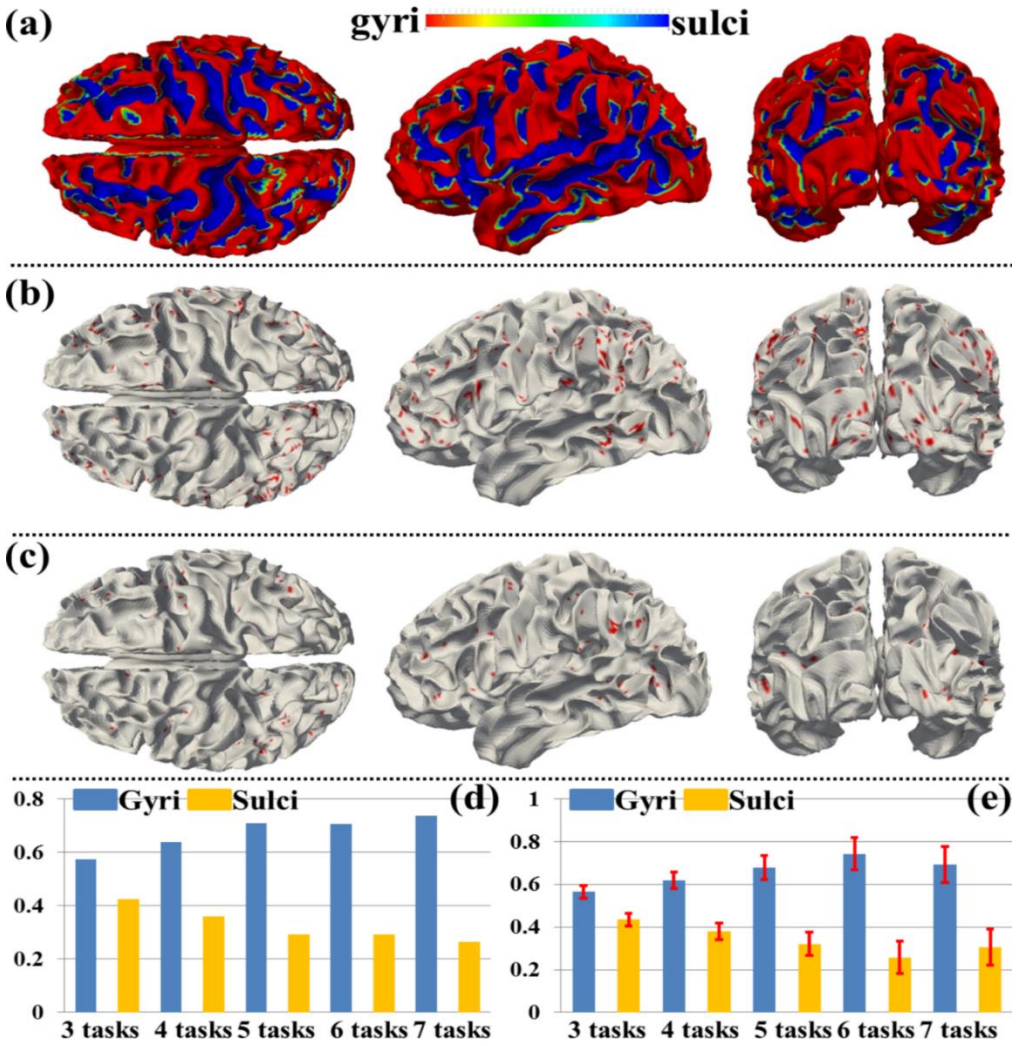

Figure 5.6. Spatial patterns of THFRs on gyri/sulci in multiple tasks and the percentages of involved grayordinates in THFRs in multiple tasks on gyri/sulci. (a): Segmented gyri and sulci of one example subject. (b)-(c): Spatial patterns of THFRs (red) on gyri (b) and sulci (c) across at least four tasks of the example subject, respectively. (d) Percentages of

involved grayordinates in THFRs on gyri/sulci in the example subject across at least three tasks. (e) Mean percentages of involved grayordinates in THFRs on gyri/sulci across at least three tasks across all subjects.

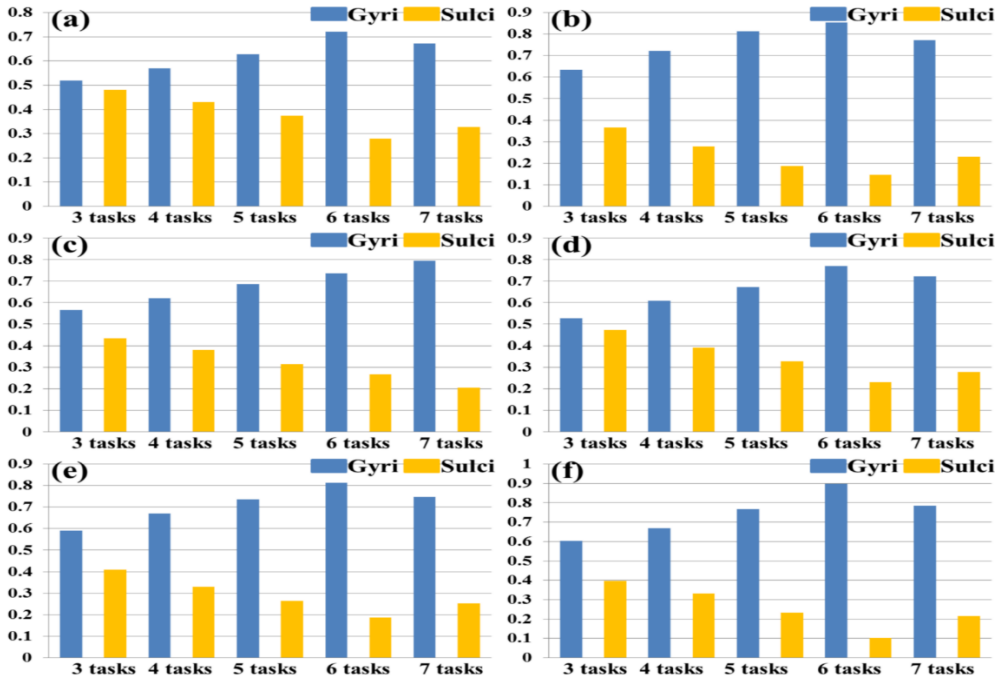

Figure 5.7. Percentages of involved grayordinates in THFRs across multiple tasks on gyri/sulci of another six subjects indexed by (a)-(f), respectively.

Table 5.4. Mean ratio of percentage of involved grayordinates in THFRs across multiple tasks on gyri vs that on sulci across all subjects. The ratio is represented as mean±standard deviation. Bold values indicate p-values smaller than 0.05.

	3 tasks	4 tasks	5 tasks	6 tasks	7 tasks
Ratio	1.31±0.16	1.66±0.29	2.22±0.64	3.33±1.67	2.53±1.05
p-value	**2.68E-26**	**2.93E-34**	**3.30E-35**	**2.00E-35**	**2.04E-27**

THFRs Distribution Difference between Cortical Gyri and Sulci is Not Due to Signal-to-noise Difference in High-resolution FMRI-When acquiring fMRI data at high resolution (2mm isotropic voxels in this chapter or below), there can be a time series signal to noise ratio (tSNR) difference between different portions of cortex (Kruger and Glover, 2001; Weiner and Grill-Spector, 2010). To examine whether the identified THFRs distribution difference between cortical gyri and sulci is merely due to the possible tSNR difference between cortical gyral and sulcal regions in high-resolution fMRI data, we measured the tSNR of each involved grayordinate in the identified THFRs. Specifically, for each grayordinate involved in the THFRs as the center, we obtained its 3-ring (about 5 mm radius, Weiner and Grill-Spector, 2010) neighborhood grayordinates on the cortical mesh surface. We then extracted the fMRI time series of all grayordinates within the 3-ring and calculated the tSNR of the centered grayordinate as follows (Weiner and Grill-Spector, 2010):

$$tSNR = \frac{mean(timeseries)}{std(timeseries)} \tag{5.2}$$

Fig. 5.8b shows the tSNR map of the THFRs on gyri and sulci in emotion task data of the same example subject in Figs. 5.4b-5.4c, respectively. We further calculated the mean tSNR of involved grayordinates in THFRs on gyri/sulci across all subjects in all seven tasks. As shown in Fig. 5.8c, we see that the tSNR of THFRs on sulci has larger mean value while also larger standard deviation compared with that on gyri. We further examined if there is statistical tSNR difference of THFRs between gyri and sulci via unpaired two-sample t-test ($p<0.01$). The results showed that the mean values of tSNR of gyri and sulci are statistically equal across all subjects in all seven tasks. In conclusion, the identified THFRs distribution difference between cortical gyri and sulci is not a result

of the possible tSNR difference in high-resolution fMRI data, and might truly reveal novel functional architecture of cortical gyri and sulci.

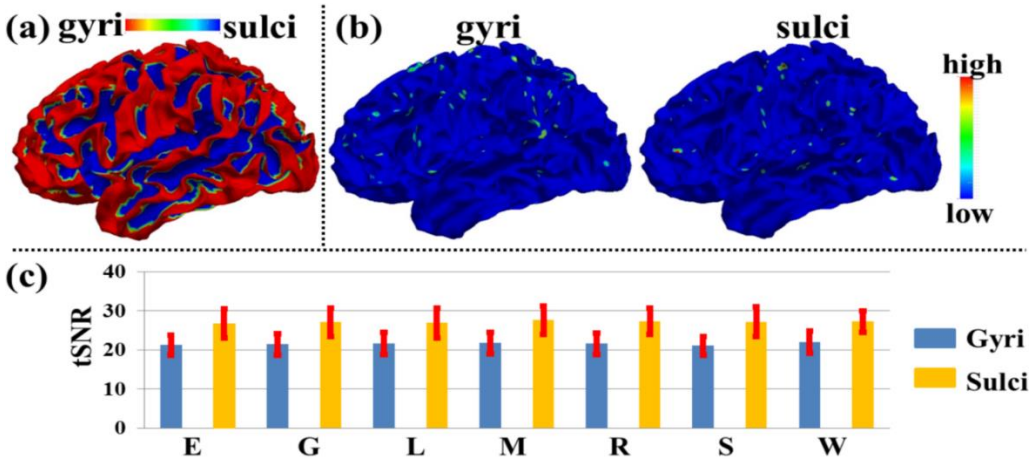

Figure 5.8. tSNR measurement: THFRs distribution difference between gyri and sulci is not due to SNR difference. (a): Segmented gyri and sulci of the same example subject in Fig. 5.4a. (b): tSNR map of the THFRs on gyri and sulci in emotion task data of the same example subject in Figs. 5.4b-5.4c, respectively. (c) Mean tSNR of involved grayordinates in THFRs on gyri/sulci across all subjects in all seven tasks.

Discussion and Conclusion

In this chapter, we systematically identified and characterized the task-based heterogeneous functional regions in specific task performances and assessed their spatial pattern distribution difference on cortical gyri and sulci. Our results have shown that the identified THFRs relatively consistently locate at the bilateral parietal lobe, frontal lobe, and visual association cortices across all subjects in both single task and across multiple tasks. Moreover, the identified THFRs locate statistically significantly more on cortical gyral regions than on cortical sulcal regions across all subjects and tasks. Particularly,

this THFRs distribution difference between gyri and sulci is not due to signal-to-noise difference in HCP high-resolution fMRI. This finding suggests that cortical gyri might participate more in multiple and heterogeneous functional processes than sulci in specific task performances, and might be consistent with Chapter 4 based on resting state fMRI data demonstrating that gyri are global functional connection centers and sulci are local functional units. These results revealed novel functional architecture of cortical gyri and sulci, and might help better understand functional mechanisms of the human cerebral cortex in the future.

In general, this chapter can be enhanced in the future in following aspects. First, all of those dictionary components derived from sparse representation should be quantitatively characterized and modeled with future understanding of human brain function and development of other effective methodology to warrant assessment of the functional network distribution and/or removal of artifacts/noise in THFRs. Second, we can extend the THFRs spatial pattern assessment on cortical gyri/sulci to subcortical gyral/sulcal regions if effective methods are developed to perform cerebellum segmentation and cerebellar surface reconstruction with the high-resolution HCP datasets in the future (Glasser et al., 2013). Third, in this chapter, we identified and reported the spatial distributions of those relatively consistent THFRs across subjects and tasks in coarse-scale, i.e., roughly locate on bilateral parietal lobe, frontal lobe, and visual association cortices. In the future, we can perform a finer scale assessment of THFRs spatial distributions and patterns on gyri/sulci by adopting our recently developed A-DICCCOL system in Chapter 2. In this way, the spatial distributions of the relatively consistent THFRs across subjects and tasks can be identified and reported at the cortical

gyral/sulcal landmark scale. We can also correlate the spatial distribution of identified THFRs with other attributes (e.g., fiber density, cortical thickness, etc.) to explore the regularity and variability between the human brain structure and function.

Acknowledgement

T. Liu was supported by NIH DA033393, NIH AG042599, NSF IIS-1149260, NSF CBET-1302089 and NSF BCS-1439051.

CHAPTER 6

TEMPORAL DYNAMICS ASSESSMENT OF SPATIAL OVERLAP PATTERN OF FUNCTIONAL BRAIN NETWORKS REVEALS NOVEL FUNCTIONAL ARCHITECTURE OF CEREBRAL CORTEX[5]

[5]Xi Jiang, Xiang Li, Jinglei Lv, Shijie Zhao, Shu Zhang, Wei Zhang, Tuo Zhang, Junwei Han, Lei Guo, and Tianming Liu. Accepted by *IEEE Transactions on Biomedical Engineering*.

Abstract

Various studies in the brain mapping field have demonstrated that there exist multiple concurrent functional networks that are spatially overlapped and interacting with each other during specific task performance to jointly realize the total brain function. Assessing such spatial overlap patterns of functional networks (SOPFNs) based on fMRI has thus received increasing interest for brain function studies. However, there are still two crucial issues to be addressed. First, the SOPFNs are assessed over the entire fMRI scan assuming the temporal stationarity, while possibly time-dependent dynamics of the SOPFNs is not sufficiently explored. Second, the SOPFNs are assessed within individual subjects, while group-wise consistency of the SOPFNs is largely unknown. To address the two issues, in this chapter, we propose a novel computational framework of group-wise sparse representation of whole-brain fMRI temporal segments to assess the temporal dynamic spatial patterns of SOPFNs that are consistent across different subjects. Experimental results based on the recently publicly released Human Connectome Project grayordinate task fMRI data demonstrate that meaningful SOPFNs exhibiting dynamic spatial patterns across different time periods are effectively and robustly identified based on the reconstructed concurrent functional networks via the proposed framework. Specifically, those SOPFNs locate significantly more on gyral regions than on sulcal regions across different time periods. These results reveal novel functional architecture of cortical gyri and sulci. Moreover, these results help better understand functional dynamics mechanisms of cerebral cortex in the future.

Introduction

There have been significant interests in the brain mapping field to study brain function using in-vivo neuroimaging techniques such as functional magnetic resonance imaging (fMRI) (Heeger and Ress, 2002; Logothetis, 2008; Friston, 2009). Specifically, task fMRI (tfMRI) records functional brain activities during a specific task performance (Heeger and Ress, 2002; Logothetis, 2008; Friston, 2009). Based on tfMRI data and associated data processing and analysis approaches, tremendous efforts have been devoted to identify brain regions and networks that are activated and functionally involved during a specific task performance (Heeger and Ress, 2002; Logothetis, 2008; Friston, 2009; Friston et al., 1994). Recently, a variety of studies (e.g., Fox et al., 2005; Bullmore and Sporns, 2009; Lv et al., 2015a; Lv et al., 2015b; Zhang et al., 2016; Zhao et al., 2015; Jiang et al., 2015) including Chapters 3 and 5 have reported an interesting finding that during a specific task performance, there exist concurrent functional networks (including both task-evoked and intrinsic connectivity functional networks), each of which locates across specific neuroanatomical areas on the human cerebral cortex. Importantly, these concurrent functional networks are spatially overlapped and interacting with each other. Those overlapped (common) brain regions among multiple concurrent functional networks, which are formally defined as spatial overlap patterns of functional networks (SOPFNs) in this chapter, have been demonstrated particularly important for the total brain function realization (e.g., Lv et al., 2015b; Duncan, 2010; Kanwisher, 2010; Pessoa, 2012; Anderson et al., 2013; Fedorenko et al., 2013), and have received increasing interest for brain function studies.

Although significant achievements have been done for SOPFNs analysis in previous studies (Lv et al., 2015b; Duncan, 2010; Kanwisher, 2010; Pessoa, 2012; Anderson et al., 2013; Fedorenko et al., 2013) as well as in Chapter 5, there are still two crucial issues to be addressed (to the best of our knowledge) as illustrated in Fig. 6.1. First, the multiple concurrent functional networks and associated SOPFNs are merely assessed based on the entire fMRI scan data assuming the temporal stationarity (Fig. 6.1a), while possibly time-dependent dynamics of the spatial patterns of functional networks and associated SOPFNs has not been sufficiently explored yet. The assumption of temporal stationarity of the functional networks and SOPFNs' spatial patterns might be problematic since neuroscience studies (Gilbert and Sigman, 2007) have suggested that the function of the brain is dynamic both spatially and temporally. That is, the dynamically changing functional interactions between different cortical regions mediate the moment-by-moment functional switching in the brain (Gilbert and Sigman, 2007). As shown in Fig. 6.1b, there is considerable variability of the spatial patterns of the same corresponding functional networks identified across different time periods, suggesting the different involvement of certain regions in the corresponding functional networks across different time periods. As a consequence, there is also considerable variability of the spatial patterns of associated SOPFNs across different time periods (Fig. 6.1b). Essentially, Chapter 5 under the temporal stationary assumption would merely identify the functional networks and associated SOPFNs from the entire time length, and ignore the considerable spatial pattern variability of those corresponding networks and associated SOPFNs across different time periods, making it incapable of assessing the temporal dynamic spatial patterns of the SOPFNs precisely. Second, the multiple

concurrent functional networks and associated SOPFNs are assessed within individual subjects and the averaged SOPFNs across different subjects are analyzed afterwards in Chapter 5. Although effective in analyzing the consistent SOPFNs across different subjects, other effective computational methodologies can be introduced to obtain accurate spatial locations of the functional networks and associated SOPFNs which are group-wise consistent across individual subjects.

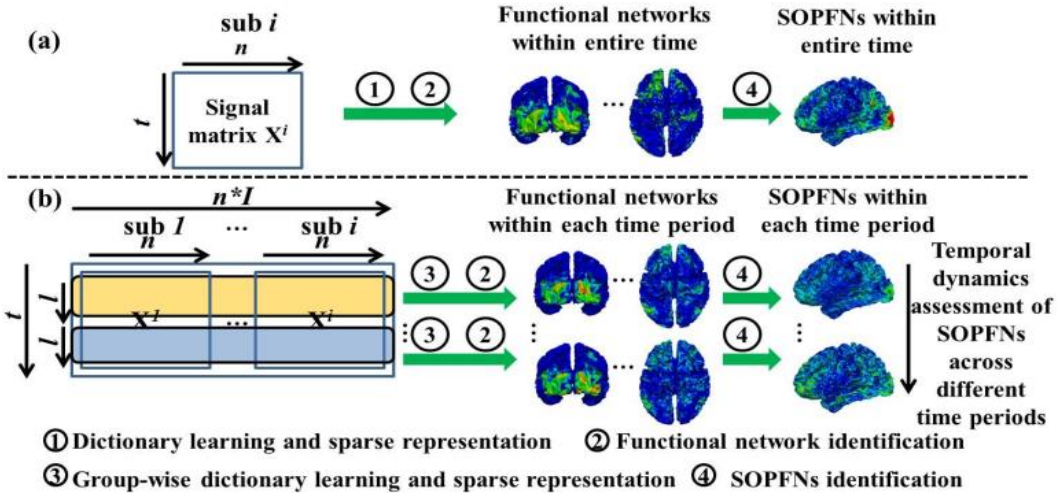

Figure 6.1. Illustration of SOPFNs assessment. (a) Previous studies (e.g., Chapter 5); (b) Our proposed framework. There are *n* tfMRI signals for each individual subject. Each signal has *t* total time points. In (b), there are *I* subjects in total. Each temporal segment has unified *l* time points. The four steps labeled as 1 to 4.

To address the above-mentioned two issues, in this chapter, we propose a novel computational framework of group-wise sparse representation of whole-brain fMRI temporal segments to assess the temporal dynamic spatial patterns of SOPFNs that are consistent across different subjects. Our contributions in this chapter are three-fold. First, instead of merely identifying temporal stationary concurrent functional networks and

associated one SOPFN based on entire fMRI scan data, we adopt the widely-used sliding time window approach (e.g., Zhang et al., 2013; Li et al., 2014; Wee et al., 2013; Wee et al., 2016) to divide the entire tfMRI signals into consecutive temporal segments, to identify the concurrent functional networks and associated SOPFNs separately based on each of the temporal segments, and to assess temporal dynamic spatial patterns of the SOPFNs across different temporal segments. Second, instead of identifying functional networks and associated SOPFNs within individual subjects, we propose a novel group-wise sparse representation of specific corresponding temporal segments across individual subjects via an effective online dictionary learning algorithm (Mairal et al., 2010) as detailed in Chapter 3 to obtain the group-wise consistent functional networks and associated SOPFNs within each specific temporal segment (time period). Third, for the first time in the brain mapping field (as far as we know), we assess the temporal dynamic spatial distribution difference of SOPFNs across different time periods between cortical gyral and sulcal regions. Chapter 5 has demonstrated that the THFRs (task-based heterogeneous functional regions) which are identified based on entire tfMRI scan data (assuming temporal stationarity) have significant spatial pattern distribution difference between cortical gyri and sulci. This has inspired us to explore the possible temporal dynamic spatial pattern distribution difference of the SOPFNs across different time periods between cortical gyral and sulcal regions in this chapter, which might help shed light on understanding functional architecture and dynamics mechanisms of cerebral cortex in the future.

Materials and Methods

Dataset and Preprocessing-We use the same preprocessed seven tfMRI grayordinate datasets in the HCP (Q1 release) as detailed in Chapter 3, which benefit the group-wise sparse representation of corresponding temporal segments across individual subjects, and assessment of temporal dynamic spatial patterns of group-wise consistent SOPFNs as well as the spatial pattern distribution of SOPFNs on gyral/sulcal regions in this chapter.

TfMRI Temporal Segments Extraction-We first extract a series of consecutive temporal segments of whole-brain tfMRI signals for each individual subject and each of the seven tfMRI datasets, respectively. Specifically, as illustrated in Fig. 6.2, for subject i, the tfMRI signals of whole-brain grayordinates are extracted as detailed in Chapter 5, normalized to zero mean and standard deviation of 1, and aggregated into a signal matrix $\boldsymbol{X}^i \in \mathbb{R}^{t\times n}$ with t time points and n grayordinates (Fig. 6.2a). Then, the sliding time window approach is adopted and defined in Eq. (6.1) to segment $\boldsymbol{X}^i$ into a series of consecutive temporal segments $\boldsymbol{X}^{i,w_j} \in \mathbb{R}^{l\times n}$ within the time window w_j which starts at time point t_j and has unified window length (number of time points) l:

$$\mathbf{X}^{i,w_j} = \left\{\mathbf{x}^{i,q} | t_j \le q < t_j + l, t_j = 1, .., (t - l + 1)\right\} \tag{6.1}$$

where $\mathbf{x}^{i,q}$ is the vector of values of q-th row of $\mathbf{X}^i$ at time point q. In total, there are $(t - l + 1)$ corresponding temporal segments (time windows) for each individual subject and each of the seven tfMRI datasets. We choose the value of window length l=20 via experimental results similar as in (Zhang et al., 2013; Li et al., 2014) based on the criterion that l should be both smaller than any of the task paradigm design (Fig. 6.2c) and large enough to reflect brain response.

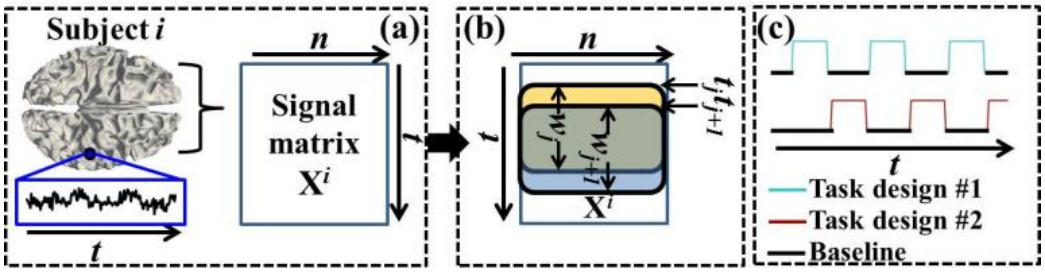

Figure 6.2. tfMRI temporal segments extraction. (a): The cortical surface and whole-brain tfMRI signal matrix $\mathbf{X}^i$ of subject i. The tfMRI signal of an example grayordinate is shown and highlighted by the blue frame. (b): Examples of extracted two consecutive temporal segments within time windows w_j and w_{j+1} (highlighted by yellow and blue frames, respectively). The first one starts at time point t_j and the second one starts at time point t_{j+1}. (c): Example of tfMRI emotion task paradigm. The blocks of the two task designs are interleaved during the entire fMRI scan time t. Window length l is smaller than the length of any of the blocks of the two task designs.

Group-wise Sparse Coding of TfMRI Temporal Segments-Once we obtain the tfMRI temporal segments, the next step is to perform group-wise dictionary learning and sparse coding of each corresponding tfMRI temporal segments across a group of subjects to obtain a comprehensive collection of group-wise consistent dictionary components within each temporal segment (time period). As illustrated in Fig. 6.3a, the conventional sparse representation framework as detailed in Chapter 3 is merely performed on each individual subject, and the group-wise consistency of the reconstructed functional network components across different subjects is not well guaranteed.

To solve this problem, in this chapter, we adopt a novel group-wise dictionary learning and sparse representation framework based on our recent work (Lv et al., 2015c)

to reconstruct group-wise consistent functional networks within each time window. As illustrated in Fig. 6.3c, considering a group of I subjects at time window w_j, the corresponding temporal segments $\left[\mathbf{X}^{1,w_j},..,\mathbf{X}^{i,w_j}\right]$ of all subjects are arranged into a big matrix $\mathbf{X}^{I,w_j} \in \mathbb{R}^{l\times(n\times I)}$. $\mathbf{X}^{I,w_j}$ is then represented as an over-complete dictionary matrix $\mathbf{D}^{I,w_j} \in \mathbb{R}^{l\times m}$ ($m > l$ and $m \ll (n \times I)$) and a sparse coefficient weight matrix $\boldsymbol{\alpha}^{I,w_j} \in \mathbb{R}^{m\times(n\times I)}$ using the online dictionary learning algorithm (Mairal et al., 2010). $\mathbf{D}^{I,w_j}$ and $\boldsymbol{\alpha}^{I,w_j}$ are calculated as follows. An empirical cost function of $\mathbf{X}^{I,w_j}$ considering the average loss of regression to all temporal segments $\mathbf{x}_k^{I,w_j}$ ($k = 1, ... (n \times I)$) is defined in Eq. (6.2).

$$f_{n\times I}(\mathbf{D}^{I,w_j}) = \frac{1}{n\times I}\sum_{k=1}^{n\times I}\min_{\boldsymbol{\alpha}_k^{I,w_j}\in\mathbb{R}^m}\frac{1}{2}\left\|\mathbf{x}_k^{I,w_j} - \mathbf{D}^{I,w_j}\boldsymbol{\alpha}_k^{I,w_j}\right\|_2^2 + \lambda\left\|\boldsymbol{\alpha}_k^{I,w_j}\right\| \tag{6.2}$$

where l_1-norm regularization and parameter λ are adopted to trade-off the regression residual and sparsity level of $\boldsymbol{\alpha}_k^{I,w_j}$, respectively. To make the coefficients in $\boldsymbol{\alpha}^{I,w_j}$ comparable, there is a constraint for $\mathbf{d}_k^{I,w_j}$ (k=1,...m) in k-th column of $\mathbf{D}^{I,w_j}$ as defined in Eq. (6.3).

$$C = \left\{\mathbf{D}^{I,w_j} \in \mathbb{R}^{l\times m} s.t. \forall k = 1, ... m, (\mathbf{d}_k^{I,w_j})^T\mathbf{d}_k^{I,w_j} \le 1\right\} \tag{6.3}$$

The whole problem in Eq. (6.2) is then rewritten as a matrix factorization problem in Eq. (6.4) and solved by effective online dictionary learning algorithm and associated publicly released toolbox (Mairal et al., 2010) to learn the dictionary $\mathbf{D}^{I,w_j}$.

$$\min_{\mathbf{D}^{I,w_j}\in C,\boldsymbol{\alpha}^{I,w_j}\in\mathbb{R}^{m\times(n\times I)}}\frac{1}{2}\left\|\mathbf{X}^{I,w_j} - \mathbf{D}^{I,w_j}\boldsymbol{\alpha}^{I,w_j}\right\|_F^2 + \lambda\|\boldsymbol{\alpha}\|_{1,1} \tag{6.4}$$

Once $\mathbf{D}^{I,w_j}$ is learned and fixed, $\boldsymbol{\alpha}^{I,w_j}$ is calculated as an l_1-regularized linear least-squares problem (Mairal et al., 2010). The values of two major parameters

dictionary size *m* and regularization parameter λ in Eq. (6.4) are experimentally determined (*m*=50 and λ=1.5) based on the criterion of consistency of reconstructed functional networks across subject groups (Lv et al., 2015a; Lv et al., 2015b).

As shown in Fig. 6.3d, in order to obtain the group-wise consistent spatial patterns of reconstructed functional networks across a group of subjects, we calculate the common sparse coefficient weight matrix $\mathbf{P}^{I,w_j} \in \mathbb{R}^{m\times n}$ based on the learned $\boldsymbol{\alpha}^{I,w_j} \in \mathbb{R}^{m\times(n\times I)}$ as follows. First, since the dictionary learning and sparse representation framework maintains the organization of all temporal segments across *I* subjects in the input $\mathbf{X}^{I,w_j}$, the learned $\boldsymbol{\alpha}^{I,w_j}$ also preserves the spatial information of temporal segments across *I* subjects. We therefore decompose $\boldsymbol{\alpha}^{I,w_j}$ into *I* sub-matrices $\left[\boldsymbol{\alpha}^{1,w_j},..,\boldsymbol{\alpha}^{i,w_j} \in \mathbb{R}^{m\times n}\right]$ corresponding to *I* subjects (Fig. 6.3c). The element (r,s) in each sub-matrix stores the corresponding coefficient value of the *s*-th grayordinate to the *r*-th dictionary in $\mathbf{D}^{I,w_j}$ for each subject. Second, since we aim to obtain the common coefficient values which are non-zero across different subjects based on the sparse matrices $\left[\boldsymbol{\alpha}^{1,w_j},..,\boldsymbol{\alpha}^{i,w_j} \in \mathbb{R}^{m\times n}\right]$, we perform t-test of the null hypothesis $(r,s)=0$ for (r,s) across *I* subjects (Lv et al., 2015c) to obtain the common sparse coefficient weight matrix $\mathbf{P}^{I,w_j} \in \mathbb{R}^{m\times n}$ (Fig. 6.3d), in which element (r,s) stores the p-value representing statistically coefficient value of the *s*-th grayordinate to the *r*-th dictionary across all *I* subjects. Third, we transform all the values in $\mathbf{P}^{I,w_j}$ from p-value to z-score just for visualization facilitation. Note that larger z-score indicates smaller p-value. Moreover, we only keep the values in $\mathbf{P}^{I,w_j}$ that are larger than 1.65 (corresponding to p-value that is smaller than 0.05) and set all other values that are smaller than 1.65 to 0. Finally, $\mathbf{p}_k^{I,w_j}$ (*k*=1,...*m*) in *k*-th row of $\mathbf{P}^{I,w_j}$ is

mapped back to the cortical surface to obtain the group-wise consistent spatial pattern of *k*-th functional network component at time window w_j (Fig. 6.3d).

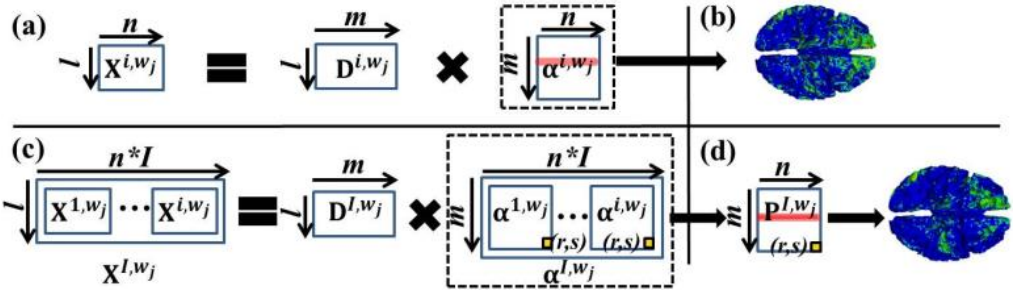

Figure 6.3. Group-wise sparse representation of temporal segments. (a) Conventional method for an individual subject. (c) The proposed method for a group of subjects. (b): The spatial pattern of an example reconstructed functional network based on conventional method. (d): The spatial pattern of an example group-wise consistent reconstructed functional network based on the proposed method.

Identification of Group-wise Consistent Functional Networks and Associated SOPFNs within Different Time Windows-Once we obtain the spatial patterns of all functional network components, the next step is to identify those meaningful group-wise consistent concurrent functional networks based on current brain science knowledge within different time windows. We adopt the similar methods in Chapter 3 to characterize and identify both task-evoked and intrinsic connectivity functional networks within different time windows. It should be noted that since we aim to assess the temporal dynamics of spatial patterns of SOPFNs based on identified corresponding functional networks across all time windows, we adopt a relatively strict criterion to only keep those functional networks that are successfully identified across all time windows (i.e., spatial pattern overlap rate R of a corresponding functional network is larger than 0.2 (Lv et al.,

2015b) across all time windows) while with potential spatial pattern variability. It is possible that certain functional networks disrupt at specific time windows while recover again at other time windows. The dynamics assessment of the spatial patterns of such functional networks would be another interesting work in the future.

The identification of SOPFNs is straightforward. It is defined as the set of all common cortical vertices (grayordinates) g_i involved in the spatial patterns of all identified concurrent functional networks at a specific time window w_j in Eq. (6.5).

$$SOPFN_{w_j} = \forall g_i s.t. g_i belongs\ to\ all\ networks\ at\ w_j \quad (6.5)$$

Since each grayordinate g_i has gyri/sulci information, those grayordinates of SOPFNs are counted for gyri and sulci, respectively, and thus the spatial pattern distribution of SOPFNs on cortical gyral/sulcal regions at a specific time window can be assessed. Finally, the temporal dynamic spatial patterns of the SOPFNs as well as the temporal dynamic spatial pattern distribution on gyri/sulci are assessed based on the identified SOPFNs across different time windows.

Results

For each of the seven tfMRI datasets, we equally divided all 64 subjects into two groups (32 each) and applied the proposed framework on each of the two subject groups to test the stability and reproducibility of our framework, and to verify the reliability and meaningfulness of identified temporal dynamic spatial patterns of SOPFNs as well as the temporal dynamic spatial pattern distribution difference of SOPFNs on gyri/sulci.

Concurrent Group-wise Consistent Functional Networks across Different Time Windows-We identified concurrent group-wise consistent functional networks which exist across all time windows based on each of the seven tfMRI datasets. Fig. 6.4

shows the spatial maps of identified functional networks in one subject group of emotion tfMRI data. Specifically, the first network (Fig. 6.4b) mainly locates at the visual cortex and has reasonable spatial pattern similarity with the GLM-derived spatial pattern, thus can be viewed as the task-evoked network. The second network (Fig. 6.4c) is widely known as the default mode network (DMN). We can see that for each of the two networks across different time windows, albeit similar in overall spatial pattern, there is considerable variability of the spatial patterns across different time windows compared with the spatial pattern merely identified from the entire time length using sparse representation and GLM/ICN template. Quantitatively, the spatial pattern overlap rate R across different time windows is 0.69±0.10 and 0.36±0.06 for the two networks, respectively. This finding is consistent between the two subject groups.

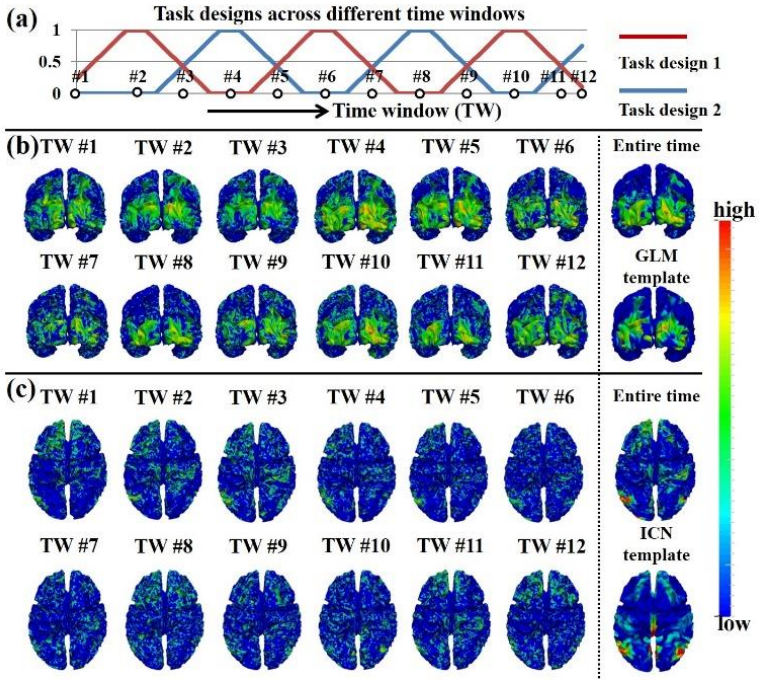

Figure 6.4. Group-wise consistent functional networks across different time windows in one subject group of emotion tfMRI data. (a) Task design curves across time windows of emotion tfMRI data. The horizontal axis is the time window and the vertical axis is the

task design value. Twelve example time windows are shown. There are two task design curves in emotion tfMRI data. For each time window, if the task design value is non-zero in both two curves, there are both two tasks performed in the time window. If the task design value is non-zero in only one task design curve, there is only the corresponding task performed in the time window. Note that the task design curves are not convoluted with hemodynamic response function for a better visualization. (b) The spatial patterns of task-evoked functional networks identified within the twelve example time windows. The corresponding networks identified from entire time length via sparse representation and GLM are also shown. (c) The spatial patterns of default mode networks (DMN) identified within the same twelve example time windows. The corresponding networks identified from entire time length via sparse representation and the DMN template (Smith et al., 2009) are also shown. (b) and (c) are color-coded by the z-scores values.

In short, the spatial pattern variability for the same functional network across different time windows suggests the time-dependent dynamics of spatial patterns of networks due to the different involvement of specific brain regions in the corresponding networks across different time windows. It is also the premise to identify the spatial patterns of SOPFNs within each time window and to assess the temporal dynamic spatial patterns of SOPFNs across all time windows.

Temporal Dynamic Spatial Patterns of SOPFNs across Different Time Windows-We assessed the SOPFN based on the identified concurrent functional networks within each time window using Eq. (6.5). Then the regularity and variability of spatial patterns of SOPFNs across different time windows were examined and compared.

We can see that there is considerable spatial pattern variability of SOPFNs across different time windows in Fig. 6.5. We further categorized all time windows into three types as illustrated in Fig. 6.5a. Specifically, time window type 1 only involves task design 1, time window type 2 only involves task design 2, and time window type 3 involves both two task designs. The mean spatial patterns of SOPFNs of time windows within each of the three time window types are shown in Fig. 6.5b. We can see that there are reasonably certain common spatial patterns of SOPFNs (with relatively higher density as highlighted by red arrows) located at the bilateral parietal/temporal/frontal lobe and visual association cortices across the three time window types and across two subject groups. Moreover, such common spatial patterns of SOPFNs are also relatively consistent across the other six tasks as illustrated in Fig. 6.6. This finding is in agreement with previous studies reporting that frontal and parietal lobes include multiple-demand patterns associated with diverse cognitive demands (Duncan, 2010; Fedorenko et al., 2013), and that visual association cortex is a heterogeneous collection of visual areas and is involved in higher level of processing (Anzai et al., 2007).

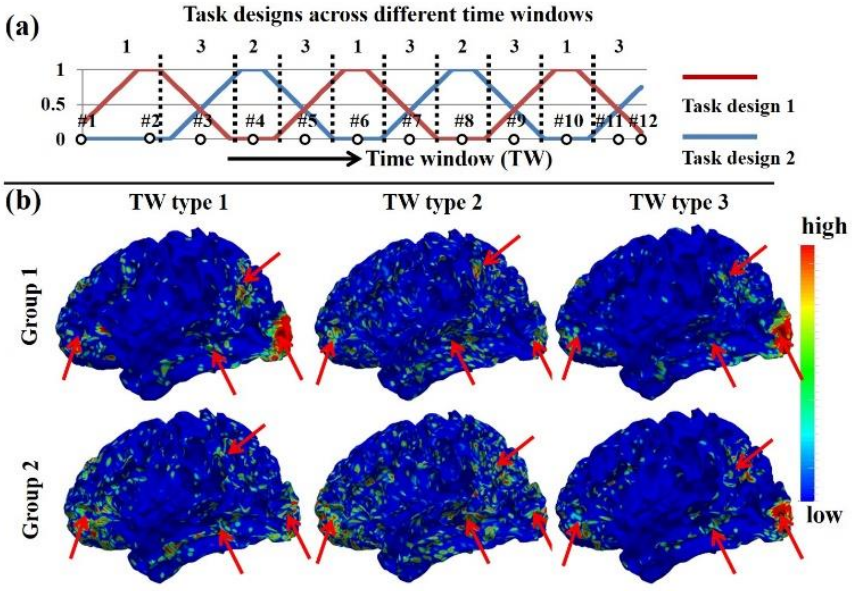

Figure 6.5. Temporal dynamic spatial patterns of SOPFNs across different time windows based on emotion tfMRI data. (a) Task design curves across time windows. The horizontal axis is the time window and the vertical axis is the task design value. The same twelve example time windows as in Fig. 6.4 are shown. There are three time window types as shown and divided by black dashed lines. Note that the task design curves are not convoluted with hemodynamic response function for a better visualization. (b) The mean spatial patterns of SOPFNs of time windows within each of the three time window types in each of the two subject groups. The common spatial patterns of SOPFNs with relatively higher density are highlighted by red arrows; (b) are color-coded by the z-scores representing SOPFNs values.

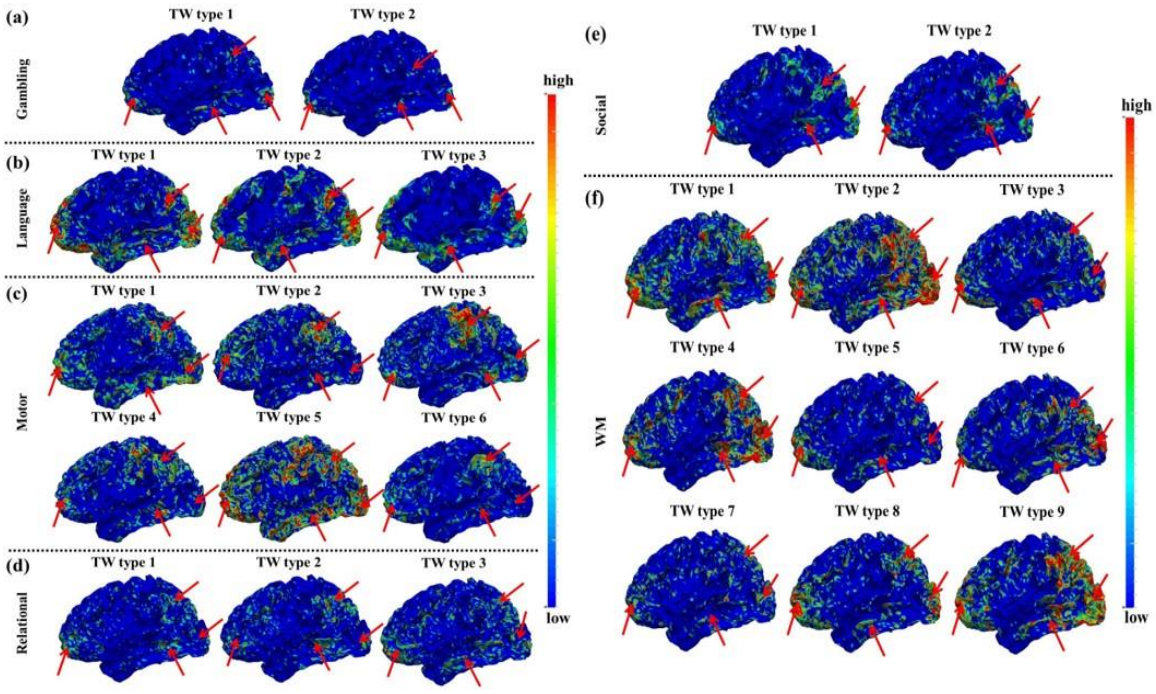

Figure 6.6. The mean spatial patterns of SOPFNs of time windows within each of the different time window types in one subject group of the other six tfMRI datasets in (a)-(f), respectively. The common spatial patterns of SOPFNs with relatively higher density

across different time window types and different tasks are highlighted by red arrows. TW represents time window. (a)-(f) are color-coded by the z-scores.

More interestingly, we can see the considerable spatial pattern variability of SOPFNs across different time window types (Fig. 6.5b and Fig. 6.6) in terms of pattern density in the common regions (bilateral parietal/temporal/frontal lobe and visual association cortices) from visual inspection, indicating the possible time-dependent dynamics of spatial patterns of SOPFNs. This phenomenon is not explored in Chapter 5 which assumes the temporal stationarity. Quantitatively, we defined and assessed the 'overlap percentage' (ratio of vertex number of overlapped region to the total vertex number of concurrent functional networks) of SOPFNs within each time window. We first performed the one-way ANOVA across all three TW types, then performed three pair-wise t-test comparison between any two of the three TW types as post-hoc multiple comparisons, and finally performed correction for multiple comparisons (Bonferroni correction) for the post-hoc tests. Table 6.1 demonstrates that the mean overlap percentage is statistically significantly large in time window type 1, small in time window type 2, and moderate in time window type 3 (involving both two task designs). This result is consistent across the two subject groups. In short, there is both regularity and variability of the identified temporal dynamic spatial patterns of SOPFNs across different time windows. Specifically, the spatial patterns of SOPFNs have reasonable common regions across different time windows (in agreement with previous studies assuming temporal stationarity) while with temporal dynamic spatial patterns in terms of significantly different overlap percentage across different time windows.

Table 6.1. Overlap percentage (mean±std) of the three time window (TW) types and the statistical comparison across different time window types in emotion task.

Overlap percentage		**TW type 1**	**TW type 2**	**TW type 3**
Group 1		0.12±0.16	0.05±0.01	0.07±0.03
Group 2		0.09±0.05	0.06±0.02	0.07±0.03
t-test		**type 1 > type 2**	**type 1 > type 3**	**type 3 > type 2**
Group 1	**tstat**	2.070	2.871	2.029
	df	62	128	118
	corrected p-value	**<u>0.043</u>**	**<u>0.007</u>**	**<u>0.043</u>**
Group 2	**tstat**	2.557	1.778	1.866
	df	62	128	118
	corrected p-value	**<u>0.020</u>**	0.065	0.065

Bold and underlined values indicate p-values smaller than 0.05. tstat: t-statistic; df: degree of freedom.

Temporal Dynamic Spatial Pattern Distribution Difference of SOPFNs between Gyral and Sulcal Regions-We assessed the spatial pattern distribution of identified SOPFN on gyral/sulcal regions within each time window, and investigated the possible temporal dynamics of spatial pattern distribution of SOPFNs on gyral/sulcal regions across different time windows. We can see that there is considerable spatial pattern distribution variability of SOPFNs on gyral and sulcal regions across different time windows as highlighted by black arrows in Fig. 6.7a. We further assessed the mean spatial pattern distributions of SOPFNs of time windows within each of the three time window types on gyral/sulcal regions as illustrated in Fig. 6.7b. We can see that there are

reasonably certain common spatial pattern distributions of SOPFNs (with relatively higher density as highlighted by red arrows) at both gyral and sulcal regions of the bilateral parietal/temporal/frontal lobe and visual association cortices across the three time window types and across two subject groups. Such common spatial patterns of SOPFNs on gyral and sulcal regions are also relatively consistent across the other six tasks as shown in Fig. 6.8.

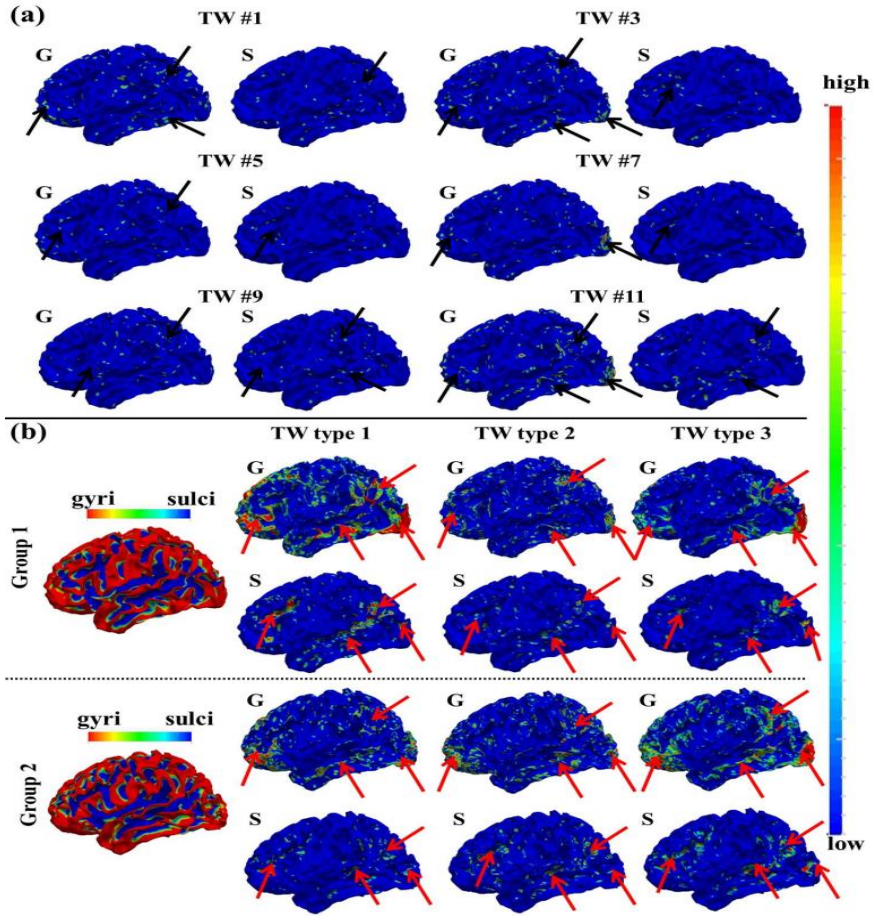

Figure 6.7. Temporal dynamic spatial pattern distributions of SOPFNs on gyral (G)/sulcal (S) regions in emotion tfMRI data. (a) Spatial pattern distributions of SOPFNs on gyral/sulcal regions in six example time windows (Fig. 6.5a). The major regions are highlighted by black arrows. (b) The mean spatial pattern distributions of SOPFNs across time windows within each of the three time window types on gyral/sulcal regions in each

of the two subject groups. The common spatial patterns of SOPFNs on gyral/sulcal regions with relatively higher density are highlighted by red arrows. Note that the surfaces illustrating the SOPFNs in (a)-(b) are color-coded by the z-scores. The two surfaces in (a)-(b) illustrating the gyri/sulci are color-coded by the principal curvature value with gyri has higher principal curvature.

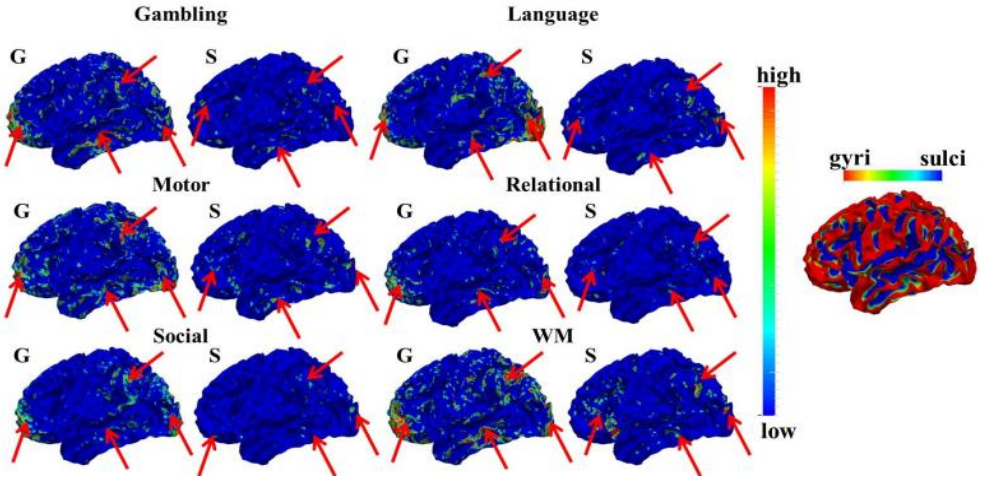

Figure 6.8. The mean spatial pattern distributions of SOPFNs across time windows within one example time window type on gyral/sulcal regions in one subject group of the other six tfMRI datasets. The common spatial patterns of SOPFNs with relatively higher density across different tasks are highlighted by red arrows. Note that the surfaces illustrating the SOPFNs are color-coded by the z-scores. The one example surface illustrating the gyri/sulci is color-coded by the principal curvature value with gyri has higher principal curvature.

More interestingly, from visual inspection, we can see the considerable spatial pattern distribution variability of SOPFNs on gyral/sulcal regions across different time window types (Fig. 6.7b and Fig. 6.8) in terms of pattern density on gyral/sulcal regions

of the common regions (bilateral parietal/temporal/frontal lobe and visual association cortices), indicating the possible time-dependent dynamics of spatial pattern distributions of SOPFNs on gyral/sulcal regions. This finding is not explored in Chapter 5 assuming the temporal stationarity. Quantitatively, we calculated the distribution percentage of SOPFNs on gyral/sulcal regions within each time window. We first performed the one-way ANOVA for the distribution percentage between gyri and sulci, and then performed corrections for multiple comparisons. The distribution percentage on gyral regions is statistically significantly larger than that on sulcal regions across all time windows ($p<0.05$). The mean ratio of distribution percentage on gyri vs that on sulci across all time windows is reported in Table 6.2. Moreover, as illustrated in Fig. 6.9, it is interesting that there are considerable peaks/valleys for the distribution percentage value on gyri/sulci during the specific time window type across the entire scan, indicating the temporal dynamics of spatial pattern distributions of SOPFNs on gyral/sulcal regions across different time windows. In short, there is both regularity and variability of the spatial pattern distributions of time-dependent SOPFNs on gyral/sulcal regions. Specifically, the spatial pattern distributions of SOPFNs on gyral/sulcal regions have reasonable common regions across different time windows (in agreement with Chapter 5 assuming temporal stationarity) while with temporal dynamics in terms of significantly larger distribution percentage on gyral regions than that on sulcal regions as well as interesting peaks/valleys alternations across different time windows.

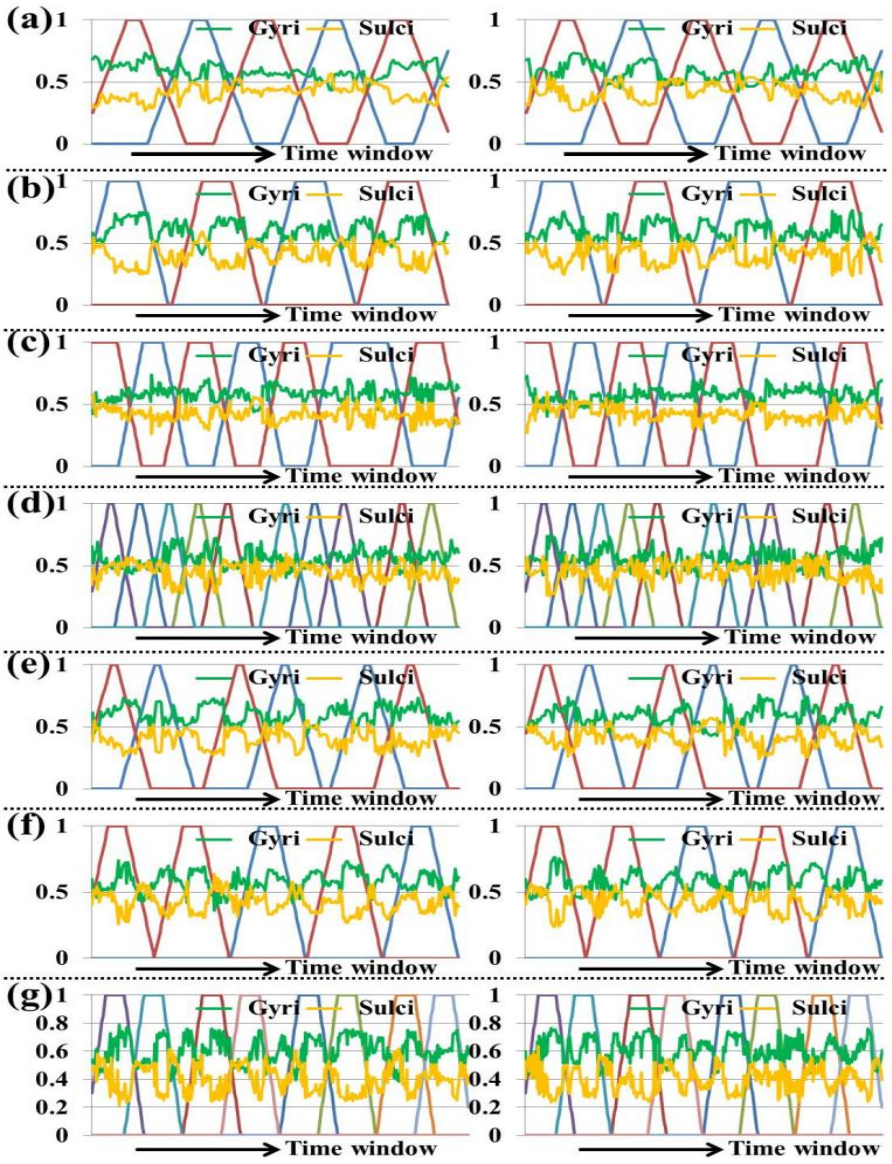

Figure 6.9. The temporal dynamic distribution percentage of SOPFNs on gyri (green curve) and sulci (orange curve) across all time windows in the two groups of the seven tasks shown in (a)-(g), respectively. In each sub-figure, the horizontal axis is the time window and the vertical axis is the distribution percentage value. Note that the task design curves are not convoluted with hemodynamic response function for a better visualization. Note that at a specific time window, the sum of percentage values of gyri and sulci equals 1.

Table 6.2. Mean ratio of distribution percentage on gyri vs that on sulci across all time windows in two subject groups of seven tasks.

	Emotion	**Gambling**	**Language**	**Motor**
Group 1	1.47	1.60	1.46	1.32
Group 2	1.45	1.55	1.38	1.33
	Rational	**Social**	**WM**	
Group 1	1.59	1.46	1.67	
Group 2	1.49	1.47	1.66	

Discussion and Conclusion

In this chapter, we identified two major functional networks (task-evoked and DMN) that are consistently exist in all time windows during the scan. During the task fMRI scan, it is straightforward that the task-evoked networks are consistently activated under specific task stimulus during the whole scanning period. The DMN has been demonstrated fundamental for brain functions and existing in both task fMRI and resting state fMRI data. It is therefore reasonable that the DMN has been identified in every time window during the whole scan in this chapter. In short, the identified consistent task-evoked network and DMN during the whole scan while with considerable spatial pattern variability are reasonable from neuroscience perspective. For the other ICNs (including resting state networks and the set of functionally connected brain networks in either resting state or task), to the best of our knowledge, Chapter 3 focuses on the exploration of those ICNs in the whole scan period, while the dynamics of those ICNs (e.g., if consistently exist or show dynamics across different time windows) during the scan period is largely unknown. That is also one of the motivations and novelties of this chapter to investigate the dynamics of the functional networks and SOPFNs.

We reported significant spatial pattern distribution difference of SOPFNs between cortical gyri and sulci across time windows. These findings are reproducible between two different subject groups and across seven different task fMRI datasets. Given the lack of ground truth in brain mapping, the reproducibility and consistency across different subjects and datasets is a reasonable justification of the reported significant SOPFN difference between cortical gyri and sulci across time windows. In short, this chapter reveals a novel functional architecture of cortical gyri and sulci in terms of significantly more distribution of SOPFNs on gyri than on sulci in a temporal dynamics way.

In this chapter, we focused on the computational framework for temporal dynamics assessment of SOPFNs. There are certain issues to be further investigated. For example, why are there peaks/valleys for the distribution percentage value of SOPFNs on gyri/sulci during the specific time windows in Fig. 6.9? Fully understanding of the unsolved concerns relating to the mechanisms of functional dynamics of cerebral cortex may need more evidence and clues from micro- or macro- scale analysis of brain structure and function in the future. We will investigate the temporal dynamic spatial pattern distribution of SOPFNs on gyral/sulcal regions in a finer scale based on our developed A-DICCCOL system in Chapter 2. We will apply the proposed framework on resting state fMRI data (e.g., the recently publicly released datasets HCP including 900 subjects, Fcon1000, etc.) to explore the temporal dynamics of spatial patterns of SOPFNs in ‘resting state’. We will apply the proposed framework on disease datasets such as Alzheimer Disease, Autism, schizophrenia, etc. to explore the possible regularity and variability of temporal dynamics of spatial patterns of SOPFNs between specific disease and normal controls, which can be potentially adopted as disease specific biomarkers.

CHAPTER 7

A CORTICAL FOLDING PATTERN-GUIDED WORKING MODEL OF FUNCTIONAL BRAIN NETWORKS[6]

[6]Xi Jiang, Xintao Hu, Tuo Zhang, Jinglei Lv, and Tianming Liu. To be submitted to *International Symposium on Biomedical Imaging (ISBI) 2017*.

Abstract

Identifying resting state networks (RSNs) based on resting state functional magnetic resonance imaging (rsfMRI) has received significant interests for brain function studies. The premise is that spatially distinct regions with similar low-frequency oscillations in rsfMRI blood-oxygen level-dependent (BOLD) signals have correlated activity patterns. Although significant achievements have been made in previous RSN studies, the underlying functional working mechanisms among the distinct regions within one RSN are still largely unknown. As an attempt to address this problem, and inspired by the previous findings in Chapters 4-6 that there are structural and functional difference between cortical folding patterns, i.e., gyri and sulci, in this chapter, we hypothesize and test a novel cortical folding pattern-guided working model of RSN: gyri serve as global functional connection centers and sulci serve as local functional units within a RSN. We examine the proposed model by using the computational framework of sparse representation of whole-brain rsfMRI signals as detailed in Chapter 3 to assess the signal representation accuracy. Experimental results based on the publicly released HCP rsfMRI data demonstrated that within a specific RSN or whole-brain, the gyral rsfMRI signals have significantly better representation accuracy based on the learned dictionary atoms than sulcal rsfMRI signals, indicating that gyri might be global functional connection centers that perform interregional neuronal communication among distinct regions within a RSN. The proposed working model of RSN provides novel insights of functional mechanisms of human brain.

Introduction

Resting state functional magnetic resonance imaging (rsfMRI) has received significant interest in studying brain functions in the brain mapping field (Friston, 2009). This approach has been demonstrated effective in identifying resting state networks (RSNs) while brain is 'at rest' as detailed in Chapter 3 based on the premise that the correlated activity patterns among spatially distinct regions have similar low-frequency oscillations in rsfMRI blood-oxygen level-dependent (BOLD) signals (Friston, 2009). Fig. 7.1a shows an example RSN which is composed of two spatially distinct regions (ROI 1 and 2 in left and right hemisphere, respectively) in volume space. Although the distinct regions within one RSN are argued to be functionally linked and interacting with each other, the underlying functional working mechanisms of interregional neuronal communication among those regions within one RSN are still largely unknown (Fig. 7.1b).

As an attempt to modeling the functional working mechanisms of RSNs and inspired by the findings of structural/functional differences between gyral and sulcal regions as detailed in Chapter 4-6 as well as the previous finding that the distinct regions within one RSN are interconnected by DTI-derived fiber bundles (Greicius et al., 2009; van den Heuvel et al., 2009), in this chapter, we examine the RSN on cortical surface (Fig. 7.1c) and hypothesize a novel cortical folding pattern-guided working model of RSN: gyri serve as global functional connection centers that perform interregional neuronal communication among distinct regions via long distance dense fibers within one RSN, and sulci serve as local functional units that directly communicate with neighboring gyri via short distance fibers (inter-column cortico-cortical fibers) and indirectly

communicate with other distant regions via the neighboring gyri with the dense fibers within one RSN (Fig. 7.1d). Specifically, we examine the proposed model by assessing the signal representation accuracy via the computational framework of sparse representation of whole-brain rsfMRI signals as detailed in Chapter 3.

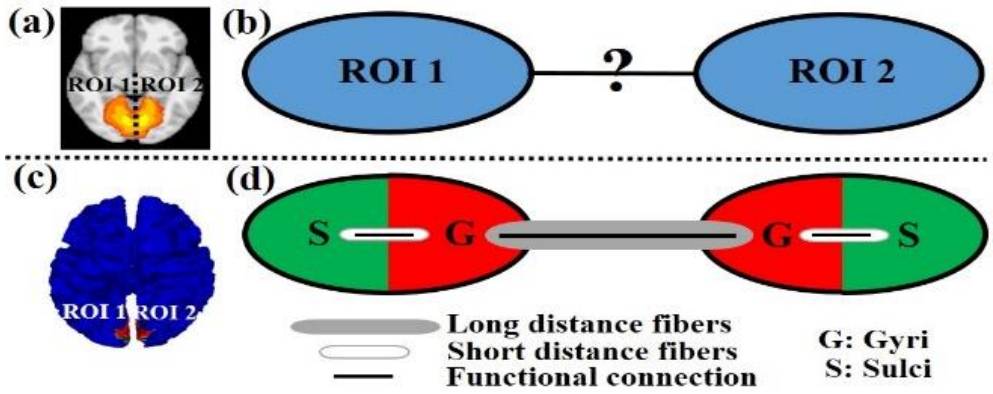

Figure 7.1. Illustration of the proposed gyri/sulci-guided model of functional network. An example RSN composed of two distinct regions (ROI 1 and 2 in left and right hemisphere, respectively) in volume space (a) and on cortical surface (c). (d) Illustrates the proposed model.

Materials and Methods

Data Acquisition and Pre-processing-We adopted multimodal rsfMRI/T1 data of ten randomly selected subjects in the recently publicly released HCP (Q1 release) (Smith et al., 2013) as a testbed in this chapter. The major rsfMRI acquisition parameters and preprocessing are detailed in Chapter 3. T1 data was used for cortical surface reconstruction for folding pattern assessment.

Sparse Representation of Whole-brain RsfMRI Signals for RSN Identification-We examine the proposed model via the computational framework of sparse representation of whole-brain rsfMRI signals in Chapter 3. The rationales are two-

fold. First, the dictionary learning and sparse representation framework in Chapter 3 has been demonstrated as an efficient and effective data-driven approach in identifying concurrent RSNs based on rsfMRI signals. This is also the premise to model the working mechanisms of RSNs. Second, the dictionary learning and sparse representation framework in Chapter 3 can learn meaningful functional activity basis patterns from hundreds of thousands of whole-brain rsfMRI signals effectively and represent the rsfMRI signals based on the learned basis efficiently and compactly. Assessing the rsfMRI signals representation accuracy based on the learned basis in gyral/sulcal regions within one RSN is thus reasonable to examine the proposed cortical folding pattern-guided working model of RSN.

After identifying the RSNs based on the methods in Chapter 3, we map the identified RSNs in rsfMRI volume space to T1 cortical surface in order to utilize the cortical folding pattern information for the proposed RSN working model. Specifically, the RSN is firstly converted into T1 volume space and then mapped onto the cortical surface using an in-house tool by localizing each voxel involved in the RSN to its nearest cortical mesh vertex.

Signal representation accuracy assessment on gyri/sulci within one RSN-The learned over-complete **D** represents a set of all basis components of functional activities from whole-brain rsfMRI signals. Each original rsfMRI signal $\mathbf{x}_i$ is approximately represented as $\bar{\mathbf{x}}_i = \mathbf{D} \times \boldsymbol{\alpha}_i$. Here we assess the rsfMRI signal representation accuracy *P* as:

$$P_{\mathbf{x}_i} = corr(\bar{\mathbf{x}}_i, \mathbf{x}_i) \tag{7.1}$$

where corr(.) is the Pearson's correlation coefficient between $\mathbf{x}_i$ and $\bar{\mathbf{x}}_i$ and ranges from 0 to 1. The larger the *P* is, the better the signal representation is for $\mathbf{x}_i$, i.e., $\mathbf{x}_i$ can be well

sparsely represented by the basis components of functional activities in **D**. In other words, $\mathbf{x}_i$ well participates in or follow the functional activities. Since theoretically, the distinct regions within one RSN have similar functional activities and are functionally linked, the assessment of the rsfMRI signal representation accuracy (Eq. (7.1)) in these distinct regions within one RSN is thus indicative of the degree of participation of specific regions within the RSN.

Specifically, for each distinct region $V = \forall v_i$ (v_i is the cortical vertex in the region) within one RSN on cortical surface, we first calculate the signal representation accuracy value P_{v_i} (Eq. (7.1)) for the rsfMRI signals of all v_i. Second, based on the principal curvature value of v_i to delineate gyral/sulcal regions as $pcurv_{v_i}\begin{cases}\geq 0, v_i \epsilon gyri \\ < 0, v_i \epsilon sulci\end{cases}$ provided in the HCP data (Smith et al., 2013), we separate *V* into gyral and sulcal regions as $V_{gyri} = \forall v_i \; s.t. pcurv_{v_i} \geq 0$ and $V_{sulci} = \forall v_i \; s.t. pcurv_{v_i} < 0$, respectively. Note that $V = V_{gyri} + V_{sulci}$. Finally, the set of all signal representation accuracy values in gyral and sulcal regions is represented as $P_{V_{gyri}} = \forall P_{v_i} \; s.t. \; v_i \in V_{gyri}$ and $P_{V_{sulci}} = \forall P_{v_i} \; s.t. \; v_i \in V_{sulci}$, respectively. By evaluating the possible mean accuracy value difference between gyral and sulcal regions in each of the distinct regions within one RSN, the proposed RSN working model is examined.

Results

Signal representation accuracy difference on gyri/sulci in DMN-We adopted the proposed framework to examine the default mode network (DMN), which is the most recognized RSN (Smith et al., 2009). As illustrated in Fig. 7.2, there are four spatially distinct ROIs in DMN including left inferior parietal lobule (ROI 1), right inferior parietal lobule (ROI 2), bilateral medial prefrontal gyrus/anterior cingulate cortex (ROI

3), and bilateral posterior cingulate cortex (ROI 4) (Greicius et al., 2009; van den Heuvel et al., 2009; Smith et al., 2009). For each of the four ROIs, we calculated the mean rsfMRI signal representation accuracy value in gyral and sulcal regions, respectively. We can see that both gyral and sulcal regions have reasonably high accuracy value (Fig. 7.2) since the sparse representation approach can relatively effectively represent whole-brain rsfMRI signals. However, there is still accuracy difference between gyral and sulcal regions. A two-sample one-tailed t-test between the set of accuracy values of gyri and sulci ($p=0.05$) shows that the signal representation accuracy value on gyri is significantly larger than that on sulci for each of the four ROIs (Fig. 7.2). More results in Fig. 7.3 indicate that this finding is consistent across different subjects. This result indicates that gyri might directly participate more than sulci in functional activities/interactions among distinct regions within DMN. That is, gyri serve as global functional connection centers to perform direct interregional functional interaction via fibers (Greicius et al., 2009; van den Heuvel et al., 2009) within DMN. Sulci also serve crucial roles in DMN by possibly indirectly communicating with distinct regions via neighbor gyri.

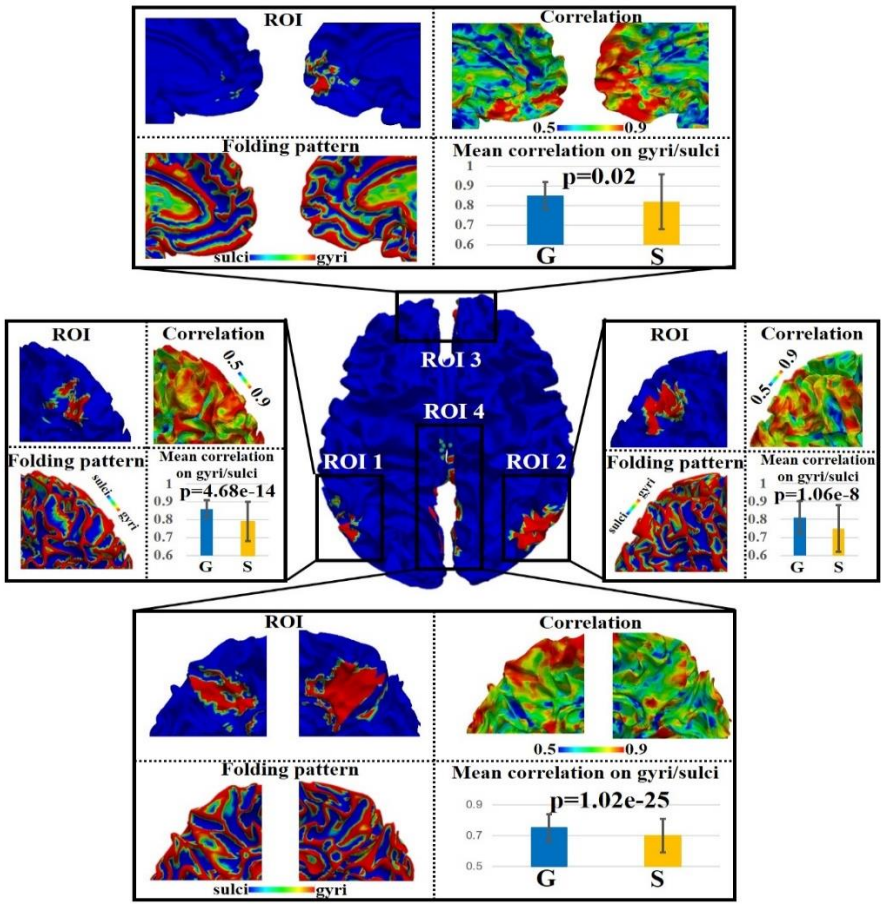

Figure 7.2. RsfMRI signal representation accuracy difference between gyral and sulcal regions in default mode network (DMN) of one example subject. The detailed assessment of each of the four distinct regions (ROI 1-4) within DMN is in zoomed-in view. G: gyri; S: sulci. The p value represents two-sample one-tailed t-test (gyri>sulci, p=0.05). The representation accuracy value ranges from 0.5 to 0.9 for a better visualization.

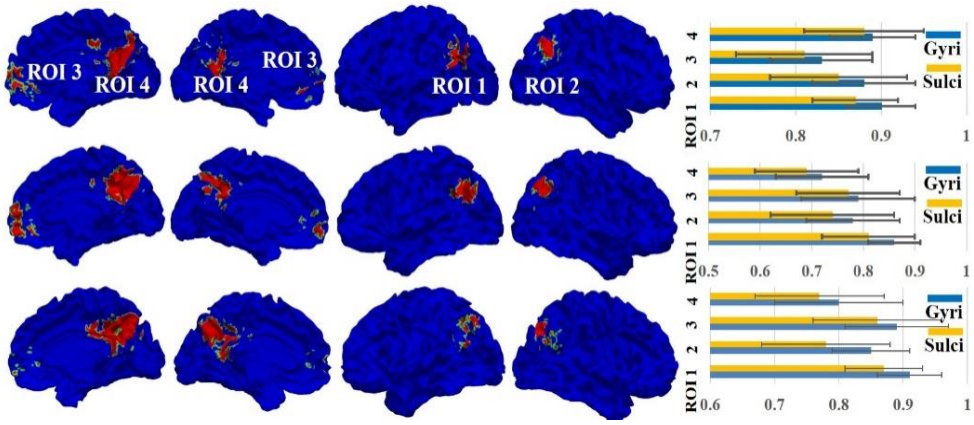

Figure 7.3. Signal representation accuracy difference between gyral and sulcal regions in DMN of another three subjects. A two-sample one-tailed t-test (p=0.05) shows that the value on gyri is significantly larger than that on sulci across all ROIs and subjects.

Signal representation accuracy difference on gyri/sulci in other RSNs-We assessed the signal representation accuracy on gyri/sulci in other RSNs to examine the reproducibility and universality of the proposed working model of RSN. Specifically, we adopted eight meaningful RSNs (Smith et al., 2009) besides DMN as examples, including three visual networks (RSN 1-3), motor (RSN 4), auditory (RSN 5), executive control (RSN 6), and bilateral frontal/parietal networks (RSN 7-8). Fig. 7.4 shows that the signal representation accuracy value on gyri is also significantly larger than that on sulci for all distinct ROIs in all eight RSNs, indicating that the proposed gyri/sulcal-based working model works for the major RSNs in the brain.

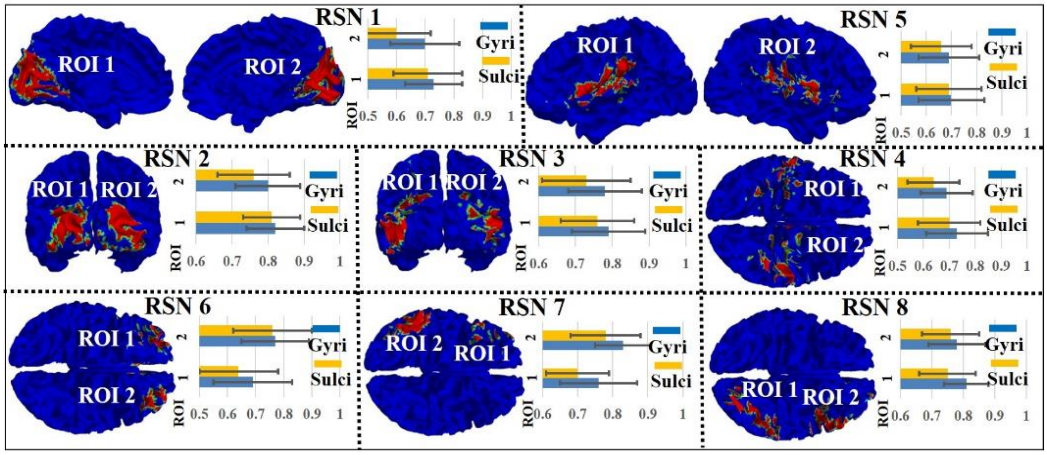

Figure 7.4. Signal representation accuracy difference between gyral and sulcal regions in the other eight RSNs of one example subject. A two-sample one-tailed t-test (p=0.05) shows that the accuracy value on gyri is significantly larger than that on sulci across all ROIs and RSNs.

Signal representation accuracy difference on gyri/sulci in whole brain-We further assessed the signal representation accuracy on gyri/sulci in the whole brain since the brain can be viewed as one comprehensive functional network integrating all functional networks (including RSNs and other networks) in the whole-brain. Fig. 7.5 shows the signal representation accuracy in the whole cortex of all ten subjects. Quantitative results in Fig. 7.6 demonstrate that the signal representation accuracy value on gyri is significantly larger than that on sulci across the whole-brain, indicating the proposed working model of RSN also applies for the whole brain, i.e., gyri are the global functional centers and sulci are the local functional units. This finding is also in agreement with previous findings showing that the resting state functional connectivity is strong between gyral-gyral regions, weak between sulcal-sulcal regions, and moderate between gyral-sulcal regions in the whole brain in Chapter 4 (Deng et al., 2014).

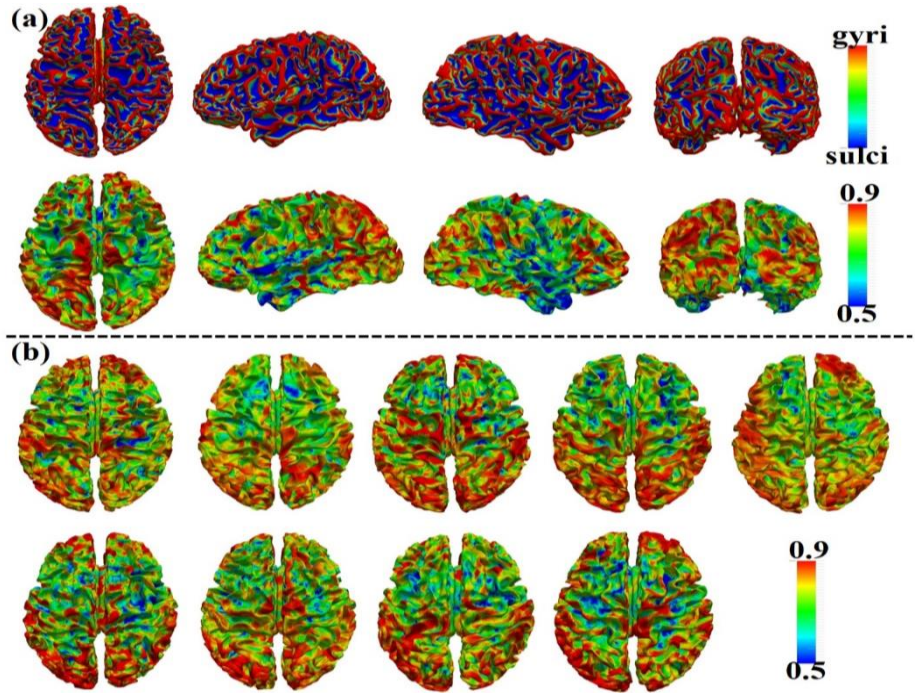

Figure 7.5. Signal representation accuracy in the whole cortex. (a) The folding pattern and signal representation accuracy in one example cortex. (b) The signal representation

accuracy in the whole cortex of the other nine subjects. The representation accuracy value ranges from 0.5 to 0.9 for a better visualization.

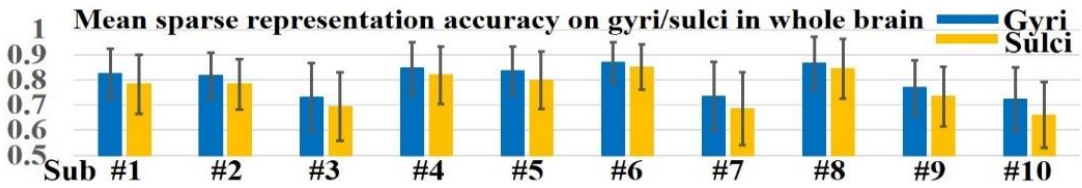

Figure 7.6. Mean signal representation accuracy in gyri/sulci of whole cortex. A two-sample one-tailed t-test (p=0.05) shows that the accuracy value on gyri is significantly larger than that on sulci across all ten subjects.

Discussion and conclusion

In this chapter, we proposed a novel cortical folding pattern-guided working model of RSN, and examined the model by assessing the rsfMRI signal representation accuracy via sparse representation in each distinct regions within the same RSN. Experimental results based on HCP rsfMRI data demonstrated that the signal representation accuracy value in gyri is significantly larger than that on sulci across nine major RSNs as well as whole-brain, indicating the effectiveness and universality of the proposed work model of RSN. Our results provide novel insights of functional mechanisms of the human brain. One future work will test and further validate the working model on more subjects, e.g., the recently released 900 subjects with rsfMRI and task fMRI datasets by HCP.

CHAPTER 8

DISCUSSION AND CONCLUSION

This dissertation systematically studied the functional interactions between cortical gyri and sulci. Experimental results have demonstrated that there are meaningful functional interactions between cortical gyri and sulci based on the four proposed approaches, respectively. It should be noted that these findings from the four approaches can be mutually supported. First, all of the four findings suggest that gyri might play a centric role in cortical functional processing than sulci. Specifically, Chapter 4 has demonstrated that gyri might serve as the global functional hubs since gyral-gyral regions have the strongest functional connectivity. Chapters 5 and 6 have demonstrated that gyri might participate more in those spatially overlapped and interacting functional networks since the THFRs/SOPFNs locate more on gyri than sulci either under temporal stationarity (Chapter 5) or temporal dynamics (Chapter 6). Chapter 7 has demonstrated that gyri might serve as global functional connection centers within a specific functional network since it well participates in or follows the functional activities in terms of better fMRI signal sparse representation accuracy. Second, all of the four findings suggest that sulci also serve crucial roles in cortical functional processing. Specifically, Chapter 4 has demonstrated that sulci might serve as local functional units since sulcal-sulcal regions have weakest functional connectivity. Chapter 5 and 6 have demonstrated that sulci also participates in those spatially overlapped and interacting functional networks since there is considerable THFRs/SOPFNs which locate on sulcal regions either under temporal

stationarity (Chapter 5) or temporal dynamics (Chapter 6). Chapter 7 has demonstrated that sulci serve as local functional units within a specific functional network since it has relatively less fMRI signal sparse representation accuracy. In conclusion, the functional interactions between cortical gyri and sulci reveals novel functional architecture of cortical gyri and sulci, and provides novel understanding of functional mechanisms of human cerebral cortex.

This research topic can be further investigated in the future from two perspectives. First, the proposed four computational approaches aim to discover the functional interactions between cortical gyri and sulci from different perspectives. They provide evidence and clues to establish a fundamental theoretic framework which can be quantitatively or mathematically formulated to represent the functional interaction model of cortical gyri and sulci in the future. Second, current studies have focused on the group-wise consistent findings of functional interactions between cortical gyri and sulci across different subjects. In the future, we can explore the individual variabilities of such functional interactions. The individual-specific functional interactions can help better understand the functional mechanisms of human brain in individual level.

REFERENCES

Anderson ML, Kinnison J and Pessoa L. (2013) Describing functional diversity of brain regions and brain networks. NeuroImage.73:50-58.

Andersson J, Smith S, and Jenkinson M. (2008) FNIRT - FMRIB's non-linear image registration tool. In 14th Annual Meeting of the Organisation for Human Brain Mapping (OHBM). 496.

Anzai A, Peng X, and Van Essen DC. (2007) Neurons in monkey visual area V2 encode combinations of orientations. Nat Neurosci. 10 (10):1313-21.

Asman AJ and Landman BA. (2011) Characterizing spatially varying performance to improve multi-atlas multi-label segmentation. Information Processing in Medical Imaging (IPMI). 6801:85-96.

Avants BB, Epstein CL, Grossman M, and Gee JC. (2008) Symmetric diffeomorphic image registration with cross-correlation: evaluating automated labeling of elderly and neurodegenerative brain. Medical Image Analysis. 12:26-41.

Barch DM, Burgess GC, Harms MP, Petersen SE, Schlaggar BL, Corbetta M, Glasser MF, Curtiss S, Dixit S, Feldt C, Nolan D, Bryant E, Hartley T, Footer O, Bjork JM, Poldrack R, Smith S, Johansen-Berg H, Snyder AZ, and Van Essen DC. (2013) Function in the Human Connectome: Task-fMRI and Individual Differences in Behavior. NeuroImage. 80:169-189.

Barron D. (1950) An experimental analysis of some factors involved in the development of the fissure pattern of the cerebral cortex. J Exp Zool. 113:553-581.

Beckmann CF, DeLuca M, Devlin JT, and Smith SM. (2005) Investigations into resting-state connectivity using independent component analysis. Philosophical Transactions of the Royal Society B: Biological Sciences. 360(1457):1001-1013.

Behrens JBH, Robson TEJ, Drobnjak MD, Rushworth I, Brady MFS, Smith JM, Higham SM, and Matthews DJ. (2004) Changes in connectivity profiles define functionally distinct regions in human medial frontal cortex. Proceedings of the National Academy of Sciences of the United States of America (PNAS). 101:13335-13340.

Biswal BB, Kylen, JV, and Hyde JS. (1997) Simultaneous assessment of flow and BOLD signals in resting-state functional connectivity maps. NMR in Biomedicine. 10(45):165-170.

Biswal BB. (2011) Resting state functional connectivity. Biological Psychiatry. 69(9): 200S-200S.

Biswal BB. (2012) Resting state fMRI: a personal history. Neuroimage. 62(2):938-944.

Bullmore E and Sporns O. (2009) Complex brain networks: graph theoretical analysis of structural and functional systems. Nature Reviews Neuroscience. 10(3):186-198.

Calhoun VD, Pekar JJ, and Pearlson GD. (2004) Alcohol intoxication effects on simulated driving: exploring alcohol-dose effects on brain activation using functional MRI. Neuropsychopharmacology. 29:2097-3017.

Chen H, Zhang T, Guo L, Li K, Yu X, Li L, Hu X, Han J, and Liu T. (2013) Coevolution of gyral folding and structural connection patterns in primate brains. Cereb Cortex. 23 (5):1208-1217.

Chen H, Li K, Zhu D, Zhang T, Jin C, Guo L, Li L and Liu T. (2013) Inferring group-wise consistent multimodal brain networks via multi-view spectral clustering. IEEE Transactions on Medical Imaging. 32(9):1576-86.

Craddock RC, James GA, Holtzheimer 3rd PE, Hu XP, and Mayberg HS. (2012) A whole brain fMRI atlas generated via spatially constrained spectral clustering. Hum Brain Mapp. 33(8):1914-1928.

Deng F, Jiang X, Zhu D, Zhang T, Li K, Guo L, and Liu T. (2014) A functional model of cortical gyri and sulci. Brain Structure and Function. 219(4):1473-91.

Dosenbach NU, Visscher KM, Palmer ED, Miezin FM, Wenger KK, Kang HC, Burgund ED, Grimes AL, Schlaggar BL, and Petersen SE. (2006) A core system for the implementation of task sets. Neuron. 50(5):799-812.

Duncan J. (2010) The multiple-demand (MD) system of the primate brain: mental programs for intelligent behaviour. Trends in cognitive sciences. 14(4):172-179.

Fang J, Hu X, Han J, Jiang X, Zhu D, Guo L, and Liu T. (2015) Data-driven analysis of functional brain interactions during free listening to music and speech. Brain Imaging and Behavior. 9(2):162-77.

Fedorenko E, Duncan J and Kanwisher N. (2013) Broad domain generality in focal regions of frontal and parietal cortex. Proceedings of the National Academy of Sciences. 110(41):16616-16621.

Fillard P, Descoteaux M, Goh A, Gouttard S, Jeurissen B, Malcolm J, Ramirez-Manzanares A, Reisert M, Sakaie K, Tensaouti F, Yo T, Mangin JF, and Poupon C. (2011) Quantitative evaluation of 10 tractography algorithms on a realistic diffusion MR phantom. Neuroimage. 56(1):220-234.

Fischl B, Sereno MI, Tootell RB, and Dale AM. (1999) High-resolution intersubject averaging and a coordinate system for the cortical surface. Hum Brain Mapp. 8:272-284.

Fischl B, Salat DH, Busa E, and Albert M. (2002) Whole brain segmentation: automated labeling of neuroanatomical structures in the human brain. Neuron. 33(3):341-355.

Fox MD, Snyder AZ, Vincent JL, Corbetta M, Van Essen DC, and Raichle ME. (2005) The human brain is intrinsically organized into dynamic, anticorrelated functional networks. Proc Natl Acad Sci U S A. 102(27):9673-9678.

Fox MD and Raichle ME. (2007) Spontaneous fluctuations in brain activity observed with functional magnetic resonance imaging. Nature Reviews Neuroscience. 8(9):700-711.

Friston KJ, Holmes AP, Worsley KJ, Poline JP, Frith CD, and Frackowiak RS. (1994) Statistical parametric maps in functional imaging: a general linear approach. Human Brain Mapping. 2(4):189-210.

Friston KJ. (2009) Modalities, modes, and models in functional neuroimaging. Science. 326:399-403.

Gazzaniga MS(Ed.). (2004) The cognitive neurosciences III. The MIT Press.

Gilbert CD and Sigman M. (2007) Brain states: top-down influences in sensory processing. Neuron. 54(5):677-96.

Glasser MF, Sotiropoulos SN, Wilson JA, Coalson TS, Fischl B, Andersson JL, Xu J, Jbabdi S, Webster M, Polimeni JR, Van Essen DC, Jenkinson M; WU-Minn HCP Consortium. (2013) The minimal preprocessing pipelines for the Human Connectome Project. Neuroimage. 80:105-24.

Greicius MD, Supekar K, Menon V, and Dougherty RF. (2009) Resting-state functional connectivity reflects structural connectivity in the default mode network. Cereb Cortex. 19(1):72-8.

Heeger DJ, and Ress D. (2002) What does fMRI tell us about neuronal activity? Nature Reviews Neuroscience. 3(2):142-151.

Honey CJ, Sporns O, Cammoun L, Gigandet X, Thiran JP, Meuli R, and Hagmann P. (2009) Predicting human resting-state functional connectivity from structural connectivity. Proceedings of the National Academy of Sciences of the United States of America (PNAS). 106(6):2035-2040.

Hu X, Guo L, Zhang D, Li K, Zhang T, Lv J, Han J, and Liu T. (2011) Assessing the Dynamics on Functional Brain Networks using Spectral Graph Theory. International Symposium on Biomedical Imaging (ISBI). 2144-2149.

Huettel SA, Song AW and McCarthy G. (2004) Functional Magnetic Resonance Imaging. 1st edition. Sunderland, MA: Sinauer Associates, Inc., ISBN: 9780878932887.

Jbabdi S, Woolrich MW, and Behrens TEJ. (2009) Multiple-subjects connectivity-based parcellation using hierarchical Dirichlet process mixture models. NeuroImage. 44:373-384.

Jenkinson M and Smith SM. (2001) A global optimisation method for robust affine registration of brain images. Medical Image Analysis. 5(2):143-156.

Jia H, Wu G, Wang Q, and Shen D. (2010) ABSORB: atlas building by self-organized registration and bundling. NeuroImage. 51(3):1057-1070.

Jiang X, Zhang T, Hu X, Lu L, Han J, Guo L, and Liu T. (2012) Music/Speech classification using high-level features derived from fMRI brain imaging. ACM Multimedia. 825-828.

Jiang X, Zhang T, Zhu D, Li K, Lv J, Guo L, and Liu T. (2013) Anatomy-guided discovery of large-scale consistent connectivity-based cortical landmarks. MICCAI. 16(Pt 3):617-25.

Jiang X, Zhu D, Li K, Zhang T, Shen D, Guo L, and Liu T. (2013) Predictive models of resting state networks for assessment of altered functional connectivity in MCI. MICCAI. 16(Pt 2):674-81.

Jiang X, Zhu D, Li K, Zhang T, Wang L, Shen D, Guo L, and Liu T. (2014) Predictive models of resting state networks for assessment of altered functional connectivity in Mild Cognitive Impairment. Brain Imaging and Behavior. 8(4):542-57.

Jiang X, Lv J, Zhu D, Zhang T, Li X, Hu X, Guo L, and Liu T. (2014) Discovery network-level functional interactions from working memory fMRI data. ISBI. 13-16.

Jiang X, Lv J, Zhu D, Zhang T, Hu X, Guo L, and Liu T. (2014) Inferring group-wise functional brain activities via point processes. ISBI. 69-672.

Jiang X, Zhang X, and Zhu D. (2014) Intrinsic functional component analysis via sparse representation on Alzheimer's Disease Neuroimaging Initiative database. Brain Connect. 4(8):575-86.

Jiang X, Zhang T, Zhu D, Li K, Chen H, Lv J, Hu X, Han J, Shen D, Guo L, and Liu T. (2015) Anatomy-guided dense individualized and common connectivity-based cortical landmarks (A-DICCCOL). IEEE Trans Biomed Eng. 62(4):1108-1119.

Jiang X, Li X, Lv J, Zhang T, Zhang S, Guo L, and Liu T. (2015) Sparse representation of HCP grayordinate data reveals novel functional architecture of cerebral cortex. Human Brain Mapping. 36(12):5301-19.

Jiang X, Zhang T, Zhao Q, Lu J, Guo L, and Liu T. (2015) Fiber connection pattern-guided structured sparse representation of whole-brain fMRI signals for functional network inference. MICCAI. 9349:133-141.

Jiang X, Li X, Lv J, Zhao S, Zhang S, Zhang W, Zhang T, Han J, Guo L, and Liu T. Temporal dynamics assessment of spatial overlap pattern of functional brain networks reveals novel functional architecture of cerebral cortex. IEEE Transactions on Biomedical Engineering, accepted.

Kanwisher N. (2010) Functional specificity in the human brain: a window into the functional architecture of the mind. Proceedings of the National Academy of Sciences. 107(25):11163-11170.

Krekelberg B, Boynton GM, and Van Wezel RJ. (2006) Adaptation: from single cells to BOLD signals. Trends in neurosciences. 29(5):250-256.

Kruger G. and Glover G.H. (2001) Physiological noise in oxygenation-sensitive magnetic resonance imaging. Magn. Reson. Med. 46:631-637.

Laird AR, Eickhoff SB, Kurth F, Fox PM, Uecker AM, Turner JA, Robinson JL, Lancaster JL, and Fox PT. (2009) ALE meta-analysis workflows via the BrainMap database: Progress towards a probabilistic functional brain atlas. Neuroinformatics. 3(23):11.

Li G, Guo L, Nie J, and Liu T. (2009) Automatic cortical sulcal parcellation based on surface principal direction flow field tracking. NeuroImage. 46(4):923-937.

Li K, Guo L, Faraco C, Zhu D, Deng F, Zhang T, Jiang X, Zhang D, Chen H, Hu X, Miller LS, and Liu T. (2010) Individualized ROI optimization via maximization of group-wise consistency of structural and functional profiles. Advances in Neural Information Processing Systems (NIPS). 23:1369-1377.

Li K, Guo L, Zhu D, Hu X, Han J, and Liu T. (2012) Individual functional ROI optimization via maximization of group-wise consistency of structural and functional profiles. Neuroinformatics. 10(3):225-242.

Li K, Guo L, Faraco C, Zhu D, Chen H, Yuan Y, Lv J, Deng F, Jiang X, Zhang T, Hu X, Zhang D, Miller LS, and Liu T. (2012) Visual analytics of brain networks. NeuroImage. 61(1):82-97.

Li K, Zhu D, Guo L, Li Z, Lynch ME, Coles C, Hu X, and Liu T. (2012) Connectomics signatures of prenatal cocaine exposure affected adolescent brains. Human Brain Mapping. 34(10):2494-2510.

Li X, Zhu D, Jiang X, Jin C, Zhang X, Guo L, Zhang J, Hu X, Li L, and Liu T. (2014) Dynamic functional connectomics signatures for characterization and differentiation of PTSD patients. Human Brain Mapping. 35(4):1761-78.

Liu T, Li H, Wong K, Tarokh A, Guo L, and Wong S. (2007) Brain tissue segmentation based on DTI data. NeuroImage. 38(1):114-123.

Liu T, Nie J, Tarokh A, Guo L, and Wong S. (2008) Reconstruction of central cortical surface from MRI brain images: method and application. NeuroImage. 40(3):991-1002.

Liu T. (2011) A few thoughts on brain ROIs. Brain Imaging and Behavior. 5(3):189-202.

Logothetis NK. (2008) What we can do and what we cannot do with fMRI. Nature. 453:869-878.

Lv J, Jiang X, Li X, Zhu D, Chen H, Zhang T, Zhang S, Hu X, Han J, Huang H, Zhang J, Guo L, and Liu T. (2015a) Sparse representation of whole-brain fMRI signals for identification of functional networks. Med Image Anal. 20(1):112-134.

Lv J, Jiang X, Li X, Zhu D, Zhang S, Zhao S, Chen H, Zhang T, Hu X, Han J, Ye J, Guo L, and Liu T. (2015b) Holistic atlases of functional networks and interactions reveal reciprocal organizational architecture of cortical function. IEEE Trans Biomed Eng. 62(4):1120-1131.

Lv J, Jiang X, Li X, Zhu D, Zhao S, Zhang T, Hu X, Han J, Guo L, Li Z, Coles C, Hu X, and Liu T. (2015c) Assessing effects of prenatal alcohol exposure using group-wise sparse representation of fMRI data. Psychiatry Research: Neuroimaging. 233(2):254-68.

Mairal J, Bach F, Ponce J, Sapiro G. (2010) Online learning for matrix factorization and sparse coding. The Journal of Machine Learning Research. 11:19-60.

Mikl M, Mareček R, Hluštík P, Pavlicová M, Drastich A, Chlebus P, Brázdil M, Krupa P. (2008) Effects of spatial smoothing on fMRI group inferences. Magnetic resonance imaging. 26(4):490-503.

Nie J, Guo L, Li K, Wang Y, Chen G, Li L, Chen H, Deng F, Jiang X, Zhang T, Huang L, Faraco C, Zhang D, Guo C, Yap PT, Hu X, Li G, Lv J, Yuan Y, Zhu D, Han J, Sabatinelli D, Zhao Q, Miller LS, Xu B, Shen P, Platt S, Shen D, and Liu T. (2012) Axonal fiber terminations concentrate on gyri. Cerebral cortex. 22 (12):2831-2839.

Passingham RE, Stephan KE, and Kotter R. (2002) The anatomical basis of functional localization in the cortex. Nature Reviews Neuroscience. 3(8):606-616.

Pessoa L. (2012) Beyond brain regions: Network perspective of cognition-emotion interactions. Behavioral and Brain Sciences. 35(03):158-159.

Poldrack RA. (2012) The future of fMRI in cognitive neuroscience. NeuroImage. 62(2):1216-1220.

Rakic P. (1988) Specification of cerebral cortical areas. Science. 241:170-176.

Raichle ME. (2010) Two views of brain function. Trends in cognitive sciences. 14 (4):180-190.

Rettmann ME, Han X, Xu C, and Prince JL. (2002) Automated sulcal segmentation using watersheds on the cortical surface. NeuroImage. 15(2):329-344.

Saygin ZM, Osher DE, Koldewyn K, Reynolds G, Gabrieli JD, and Saxe RR. (2011) Anatomical connectivity patterns predict face selectivity in the fusiform gyrus. Nat Neurosci. 15(2):321-327.

Seeley WW, Menon V, Schatzberg AF, Keller J, Glover GH, Kenna H, Reiss AL, and Greicius MD. (2007) Dissociable intrinsic connectivity networks for salience processing and executive control. J Neurosci. 27(9):2349-56.

Shen D and Davatzikos C. (2002) HAMMER: hierarchical attribute matching mechanism for elastic registration. IEEE Transaction on Medical Imaging. 21(11):1421-1439.

Siegel S and Castellan Jr. NJ. (1988) Nonparametric statistics for the behavioral sciences (2nd ed.). 266. McGraw-Hill, New York.

Smith SM, Fox PT, Miller KL, Glahn DC, Fox PM, Mackay CE, Filippini N, Watkins KE, Torod R, Laird AR, and Beckmann CF. (2009) Correspondence of the brain's functional architecture during activation and rest. Proceedings of the National Academy of Sciences. 106(31):13040-13045.

Smith SM, Andersson J, Auerbach EJ, Beckmann CF, Bijsterbosch J, Douaud G, Duff E, Feinberg DA, Griffanti L, Harms MP, Kelly M, Laumann T, Miller KL, Moeller S, Petersen S, Power J, Salimi-Khorshidi G, Snyder AZ, Vu AT, Woolrich MW, Xu J, Yacoub E, Uğurbil K, Van Essen DC, and Glasser MF. (2013) Resting-state fMRI in the Human Connectome Project. NeuroImage. 80(15):144-168.

Takahashi E, Folkerth RD, Galaburda AM, and Grant PE. (2012) Emerging cerebral connectivity in the human fetal brain: an MR tractography study. Cerebral cortex. 22 (2):455-464.

Thompson PM and Toga AW. (1996) A surface-based technique for 1336 warping 3-dimensional images of the brain. IEEE Transaction on Medical Imaging. 15(4)1-16.

Tournier JD, Calamante F, and Connelly A. (2012) MRtrix: Diffusion tractography in crossing fiber regions. Int J Imaging Syst Technol. 22(1):53-66.

Tuch DS, Reese TG, Wiegell MR, Makris N, Belliveau JW, and Wedeen VJ. (2002) High angular resolution diffusion imaging reveals intravoxel white matter fiber heterogeneity. Magn. Res. Med. 48(4):577-582.

Uğurbil K, Xu J, Auerbach EJ, Moeller S, Vu AT, Duarte-Carvajalino JM, Lenglet C, Wu X, Schmitter S, Van de Moortele PF, Strupp J, Sapiro G, De Martino F, Wang D, Harel N, Garwood M, Chen L, Feinberg DA, Smith SM, Miller KL, Sotiropoulos SN, Jbabdi S, Andersson JL, Behrens TE, Glasser MF, Van Essen DC, Yacoub E; WU-Minn HCP Consortium. (2013)
Pushing spatial and temporal resolution for functional and diffusion MRI in the Human Connectome Project. Neuroimage. 80:80-104.

Van den Heuvel MP, Mandl R, and Pol HH. (2008) Normalized cut group clustering of resting-state FMRI data. PloS one. 3(4):e2001.

Van den Heuvel MP, Mandl RC, Kahn RS, and Hulshoff Pol HE. (2009) Functionally linked resting-state networks reflect the underlying structural connectivity architecture of the human brain. Hum Brain Mapp. 30(10):3127-4.

Van Essen DC and Dierker DL. (2007) Surface-based and probabilistic atlases of primate cerebral cortex. Neuron. 56(2):209-225.

Van Essen DC, Smith SM, Barch DM, Behrens TE, Yacoub E, Ugurbil K; WU-Minn HCP Consortium. (2013) The WU-Minn Human Connectome Project: an overview. Neuroimage. 80:62-79.

Wang P, Zhu D, Chen H, Jiang X, Sun L, Cao Q, Li A, Liu T, and Wang Y. (2013) Identifying functional connectomics abnormality in attention deficit hyperactivity disorder. ISBI. 544-547.

Wee CY, Yang S, Yap P, and Shen D. (2013) Temporally dynamic resting-state functional connectivity networks for early MCI identification. Machine Learning in Medical Imaging. 139-146.

Wee CY, Yang S, Yap P, and Shen D. (2016) Sparse temporally dynamic resting-state functional connectivity networks for early MCI identification. Brain Imaging Behav. 10(2):342-356.

Weiner KS and Grill-Spector K. (2010) Sparsely-distributed organization of face and limb activations in human ventral temporal cortex. Neuroimage. 52(4):1559-73.

Welker W. (1990) Why does cerebral cortex fissure and fold? A review of determinants of gyri and sulci. Cereb Cortex. 8:3-136.

Worsley KJ. (1997) An overview and some new developments in the statistical analysis of PET and fMRI data. Human Brain Mapping. 5(4):254-258.

Wright J, Yang AY, Ganesh A, Sastry SS, and Ma Y. (2009) Robust face recognition via sparse representation. Pattern Analysis and Machine Intelligence, IEEE Transactions on. 31(2):210-227.

Xu J, Potenza MN, and Calhoun VD. (2013) Spatial ICA reveals functional activity hidden from traditional fMRI GLM-based analyses. Frontiers in neuroscience. 7.

Yap P, Gilmore JH, Lin W, and Shen D. (2011) POPTRACT: population-based tractography. IEEE Transaction on Medical Imaging. 30:1829-1840.

Yuan Y, Jiang X, Zhu D, Chen H, Li K, Lv P, Yu X, Li X, Zhang S, Zhang T, Hu X, Han J, Guo L, and Liu T. (2013) Meta-analysis of functional roles of DICCCOLs. Neuroinformatics. 11(1):47-63.

Yue Y, Loh JM, and Lindquist MA. (2010) Adaptive spatial smoothing of fMRI images. Statistics and its Interface. 3:3-13.

Zeng T, Chen H, Fakhry A, Hu X, Liu T, and Ji S. (2015) Allen mouse brain atlases reveal different neural connection and gene expression patterns in cerebellum gyri and sulci. Brain Structure and Function. 220(5):2691-703.

Zhang P and Cootes TF. (2011) Automatic part selection for groupwise registration. Information Processing in Medical Imaging (IPMI). 6801:85-96.

Zhang S, Li X, Lv J, Jiang X, Guo L, and Liu T. (2016) Characterizing and differentiating task-based and resting state fMRI signals via two-stage sparse representations. Brain Imaging and Behavior. 10(1):21-32.

Zhang T, Guo L, Li K, Jing C, Hu X, Cui G, Li L, and Liu T. (2012) Predicting functional cortical ROIs via DTI-derived fiber shape models. Cerebral Cortex. 22(4):854-864.

Zhang T, Chen H, Guo L, Li K, Li L, Zhang S, Shen D, Hu X, and Liu T. (2014) Characterization of U-shape streamline fibers: methods and applications. Med Image Anal. 18(5):795-807.

Zhang X, Guo L, Li X, Zhang T, Zhu D, Li K, Chen H, Lv J, Jin C, Zhao Q, Li L, and Liu T. (2013) Characterization of task-free and task-performance brain states via functional connectome patterns. Med Image Anal. 17(8):1106-22.

Zhao S, Jiang X, Han J, Hu X, Zhu D, Lv J, Zhang T, Guo L, and Liu T. (2014) Decoding auditory saliency from fMRI brain imaging. ACM Multimedia. 873-876.

Zhao S, Han J, Lv J, Jiang X, Hu X, Zhao Y, Ge B, Guo L, and Liu T. (2015) Supervised dictionary learning for inferring concurrent brain networks. IEEE Transactions on Medical Imaging. 34(10):2036-45.

Zhu D, Li K, Faraco C, Deng F, Zhang D, Jiang X, Chen H, Guo L, Miller LS, and Liu T. (2011) Discovering dense and consistent landmarks in the brain. Information Processing in Medical Imaging (IPMI). 22:97-110.

Zhu D, Li K, Faraco C, Deng F, Zhang D, Jiang X, Chen H, Guo L, Miller LS, and Liu T. (2011) Optimization of functional brain ROIs via maximization of consistency of structural connectivity profiles. NeuroImage. 59:1382-93.

Zhu D, Li K, Guo L, Jiang X, Zhang T, Zhang D, Chen H, Deng F, Faraco C, Jin C, Wee C, Yuan Y, Lv P, Yin Y, Hu X, Duan L, Hu X, Han J, Wang L, Shen D, Miller LS, Li L, and Liu T. (2013) DICCCOL: Dense Individualized and Common Connectivity-based Cortical Landmarks. Cerebral Cortex. 23(4)4:786-800.